EIGENSTRUCTURE ASSIGNMENT FOR A TAILLESS AIRCRAFT

BY

Clara B. Nieto-Wire

A dissertation submitted to the Graduate Faculty in Electrical Engineering in partial fulfillment of the requirements for the degree of Doctor of Philosophy, The City University of New York

2012

This manuscript has been read and accepted for the Graduate Faculty in Engineering in satisfaction of the dissertation requirements for the degree of Doctor of Philosophy.

Prof. Kenneth M. Sobel

Date

Chair of Examining Committee

Prof. Mumtaz Kassir

Date

Executive Officer

Professor G.M. Kranc

Professor Y.L Tian

Professor J. Xiao

Professor A.I. Belkharraz, Mathematics Dept, LGCC

Dr. J.E. Piou, MIT Lincoln Laboratory

Supervisory Committee

The City University of New York

Abstract

EIGENSTRUCTURE ASSIGNMENT FOR A TAILLESS AIRCRAFT

By

Clara B. Nieto-Wire

Adviser: Professor Kenneth M. Sobel

In the first part of our work we apply eigenstructure assignment to the design of a flight control system for a wind tunnel model of a tailless aircraft. The aircraft, known as the innovative control effectors (ICE) aircraft, has unconventional control surfaces plus pitch and yaw thrust vectoring. We show how to modify the desired eigenvalues to simultaneously achieve acceptable responses to pilot commands, stabilize the phugoid mode, satisfy MIL-F-8785C mode specifications and satisfy MIL-F-9490D specifications on phase and gain margins.

We use the unified delta operator model to obtain a flight control system for the ICE aircraft that is valid for both continuous time and sampled data operation. We prove a new result that extends disk gain and phase margins to the delta operator system. We consider symmetric lock in place failures of either the elevons or the all moving tips. We propose a novel eigenstructure assignment reconfiguration capable of maintaining stability, desired performance, and disk gain/phase margins of the ICE aircraft under symmetric lock in place failures in the lateral control effectors.

In the second part of our work we extend multiple and simultaneous fault detection and isolation (FDI) system design by a single diagnostic observer to the delta operator model. First, we reformulate the detection filter problem and detectability conditions for delta operator systems. Then, we present (1) the mathematical results that extend fixed directional residuals to delta operator systems, (2) the conditions for allowable failures, (3) a new projection matrix W that is independent of eigenvectors to diagonalize the failure/residual map, (4) a method for computing the observer gains for delta operator systems, and (5) a new result for the delta operator model fault free residual bound. Based upon these mathematical results, we propose a new eigenvector selection criterion for robust FDI to unstructured uncertainty and known initial condition mismatches. Then, we present a new method/algorithm for multiple and simultaneous FDI of actuator failures for delta operator systems which is capable of monitoring a variety of failures in the control actuators.

We consider the linearized longitudinal dynamics of a VTOL aircraft in the vertical plane subject to the combined and separate effects of an initial condition mismatch in the vertical velocity state and bias actuator failures of the pitch control and the longitudinal pitch control. We show that FDI system design by fixed directional residuals that use eigenstructure-based optimizations result in different sets of eigenvectors. Thus, residual responses can vary significantly. In contrast, our optimization and simulations results show that our algorithm for FDI yields well-conditioned residual generators with excellent and tightly consistent residual responses with detection time of 4 ms for 1ms sampled data operation.

ACKNOWLEDGMENTS

The author wishes to thank her thesis advisor, Prof. Sobel for sharing his remarkable skill and expertise in the area and for proposing a highly challenging yet absolutely beautiful topic. As an engineer, I consider all these, precious and invaluable, and therefore there are no words to express my gratitude for my advisor's generous gift. Thank you Prof. Sobel.

I also would like to express my gratitude to my thesis committee members for their valuable input, and to all faculty from the Electrical Engineering Department at CCNY, from the CUNY Graduate Center, and from BMCC for the support and the quality education that has been provided.

I am deeply grateful to the Louis Stokes Alliance for Minority Participation (LSAMP) Program, the Alliances for Graduate Education and the Professoriate (NSF/CUNY AGEP # 0450360) Program, the CUNY Graduate Center, and The School of Engineering of The City College of New York - CUNY, for the financial support without which this research would not have been possible. Special thanks to Dr. Claude Brathwaite, and Prof. Gail Smith for their support, motivation and guidance during all these years.

To my mother Ligia and my childhood maestro Plutarco for who they are and for working untiringly to equip me with what they thought would help me achieve my dreams. A mi madre Ligia y a mi maestro de infancia Plutarco por ser quienes son y por trabajar incansablemente para equiparme con lo que ellos consideraron me ayudaria a realizar mis sueños.

Special thanks to Dr. Flavio Cabrera, an extraordinary colleague and an unrivaled friend.

Finally, I would like to thank Michael, Veronica and Natalia for being the inspiration of my everyday work and to Anita, Angel, Angelica, Hernando, Francisco and their families for their unconditional love, and support.

Table of Contents

List of Tables x

List of Figures xii

1 Introduction 1

- 1.1 Background . . . 1
  - 1.1.1 Eigenstructure Assignment for the Innovative Control Effectors Aircraft . . . 1
  - 1.1.2 Fault Detection and Isolation . . . 5
- 1.2 Historical Review . . . 8
  - 1.2.1 Eigenstructure Assignment for Linear Systems . . . 8
  - 1.2.2 Pseudo Control . . . 11
  - 1.2.3 Delta Operator Eigenstructure Assignment . . . 14
  - 1.2.4 Observer-Based Residual Generator for Multiple Fault Detection and Isolation - Shen et al. . . . 18
- 1.3 Contributions of the Thesis . . . 21
  - 1.3.1 Nonlinear Simulation . . . 21
  - 1.3.2 Flight Control System Design . . . 21
  - 1.3.3 Reconfigurable Control System . . . 22
  - 1.3.4 Fault Detection and Isolation . . . 23
- 1.4 Outline . . . 25

2 Eigenstructure Assignment for the Innovative Control Effectors Aircraft 27

2.1 Overview 27

2.2 Flight Control System Design 28

2.3 Robustness Results 39

2.4 Nonlinear Simulation Results 44

3 Reconfigurable Control System 49

3.1 Overview 49

3.2 Problem Statement 50

3.3 Mathematical Results 51

3.4 Delta Eigenstructure Assignment Reconfiguration 53

3.5 Symmetric Lock in Place Failure Reconfiguration Results 62

4 Fault Detection and Isolation 74

4.1 Overview 74

4.2 Problem Statement 75

4.3 Mathematical Results 80

4.4 Robustness Results 84

4.5 Eigenvector Selection Criterion 86

4.6 Numerical Method for Robust and Multiple FDI of Actuator Failures by Fixed Directional Residuals for Delta Operator Systems 87

4.7 Implementation and Example - Our Algorithm 89

4.8 Algorithm Consistency 101

5 Concluding Remarks 113

5.1 Conclusions 113

5.2 Problems and Recommendations 116

Appendix A Proof of Theorem 3.1 **119**

Appendix B Proof of Theorem 3.2 **120**

Appendix C Proof of Theorem 3.3 **122**

Appendix D Proof of Theorem 4.1 **125**

Appendix E Proof of Corollary 4.1 **126**

Appendix F Proof of Corollary 4.2 **127**

Appendix G Proof of Lemma 4.1 **129**

Appendix H Proof of Theorem 4.2 **130**

List of Publications **134**

Bibliography **135**

List of Tables

1. Eigenvalues and eigenvectors for the lateral dynamics 29
2. SVD of Lateral Control Distribution Matrix 30
3. Lateral Eigenstructure Assignment Design 31
4. SVD of Longitudinal Control Distribution Matrix 35
5. Longitudinal feedback gain matrix K_D 37
6. Longitudinal Disk Gain/Phase Margins 38
7. Lateral Disk Gain/Phase Margins 40
8. Lateral Eigenstructure Assignment Design 40
9. Comparison of Gains for Different Projection Methods 54
10. Disk Phase Margin vs. samples/sec for no failure case 56
11. Optimal and Feasible Solutions for 100% elevon failure 58
12. No Failure Case: Feedback Gains, Gain/Phase Margins, and Eigenvalues . 60
13. Longitudinal feedback gains 61
14. 100% elevon failure: Feedback Gains, Gain/Phase Margins, and Eigenvalues 62
15. 100% amt failure: Feedback Gains, Gain/Phase Margins, and Eigenvalues . 64
16. Diagnostic observer's γ-domain eigenvalues, allowable subspaces and eigevector parameter α_i 93
17. Optimal Alphas for runs 5, 13, 25, 39, 47 95
18. P, L_ρ for runs 5, 13, 25, 39, 47 97
19. Diagnostic observer z-domain eigenvalues, allowable subspaces and eigevector parameter α_i. 104

20. Optimal Alphas for runs 5, 13, 25, 39, 47 - Shen et al. algorithm. 108

21. P, L for runs 5, 13, 25, 39, 47 - Shen et al. algorithm. 109

List of Figures

2.1 Block diagram of lateral flight control system 33

2.2 Linear time responses to a 1 deg initial sideslip 34

2.3 Block diagram of longitudinal flight control system 38

2.4 Monte carlo simulation for lateral dynamics 42

2.5 Monte carlo simulation for longitudinal dynamics 44

2.6 Nonlinear time responses to a 1 deg/s p_s pulse 45

2.7 Nonlinear control responses to a 1 deg/s p_s pulse 46

2.8 Nonlinear time responses to a 1 g cstar step 47

2.9 Nonlinear control responses to a 1 g cstar step 48

3.1 Washout filter eigenvalue vs. dutch roll natural frequency 57

3.2 All moving tips failure before roll rate command (states) 66

3.3 Elevon failure before roll rate command (states) 67

3.4 All moving tips failure before lateral gust (states) 68

3.5 Elevon failure before lateral gust (states) 69

3.6 All moving tips failure during roll rate command (states) 70

3.7 All moving tips failure during roll rate command (controls) 71

3.8 All moving tips failure during roll rate command (speed, altitude, alpha) 72

3.9 Elevon failure during roll rate command (states) 73

4.1 Observer-based residual generator. 78

4.2 Optimization Results. 94

4.3 Optimal Alphas 96

4.4 Residual response to failure-initial mismatch separate effect. 99

4.5 Residual response to failure-initial mismatch combined effect. 100

4.6 Optimization Results - Shen et al. algorithm. 106

4.7 Optimal Alphas - Shen et al. algorithm. 108

4.8 Residual response to failure-initial mismatch separate effect. 111

4.9 Residual response to failure-initial mismatch combined effect. 112

Chapter 1

Introduction

1.1 Background

1.1.1 Eigenstructure Assignment for the Innovative Control Effectors Aircraft

We consider the design of a flight control system using eigenstructure assignment for a wind tunnel model of the Innovative Control Effectors (ICE) aircraft. This tailless aircraft program was first described by Dorsett and Mehl [1] and by Dorsett et al. [2]. The ICE aircraft has many unconventional control surfaces plus pitch and yaw thrust vectoring.

We develop a nonlinear 6DOF simulation for dynamic analysis and control design validation of the ICE tailless aircraft. We modified the Aircraft Control Toolbox [3] to include look up tables with interpolation for approximately 20,000 values of the ICE aircraft aerodynamic coefficients [4]. Then, we modified the force and moment equations to include yaw and pitch thrust vectoring. We also modified the trim program cost function to penalize nonzero trim bank angle and non-1g trim normal acceleration. Finally, we added limiters on actuator deflections, deflection rates, and control system integrators.

Several authors have proposed flight control system designs for the ICE aircraft. Ngo et al. [5] use dynamic inversion with structured singular value synthesis. However, the authors remove the bank angle equation from the model which causes an unstable complex mode to be replaced with an unstable real mode. This occurs because the ICE aircraft does not exhibit a conventional real spiral mode. Sparks [6] uses linear parameter varying control. Schumacher and Johnson [7] use dynamic inversion with adaptation for self reconfiguring. Shtessel et al. [8] propose reconfigurable sliding mode control with direct adaptation. Hess et al. [9] use sliding mode control with asymptotic observers. However, the results in Ref. [9] are based only upon linear simulation. The only previous design using eigenstructure assignment was proposed by Jones et al. [10]. The main emphasis of Ref. [10] is a method for gain scheduling. Thus, no details of the eigenstructure assignment design are shown. Furthermore, [10] ignores the phugoid mode, only uses pitch flap for the longitudinal controller, uses a pitch rate command system, and only uses elevon for the lateral control system.

Eigenstructure assignment is an excellent method for incorporating classical specifications on damping, settling time, and mode decoupling into a modern multivariable control framework. Andry et al. [11] applied eigenstructure assignment to the design of a constant gain output feedback aircraft flight control system. Andry et al. [11] proposed a choice for the desired eigenvectors for the lateral dynamics of an aircraft based upon mode decoupling. The desired eigenvectors in Ref. [11] are based upon decoupling yaw rate and sideslip angle from roll rate and bank angle. Later, Davidson and Andrisani [12] proposed another choice for desired eigenvectors. The desired eigenvectors in Ref. [12] are based upon the observations that bank angle is the integral of roll rate and bank angle should induce a yaw rate. The desired eigenvectors in [12] have only two specified entries which is fewer than the number of specified entries in Ref. [11]. This is an important point because the lateral dynamics has only two independent control directions which are yawing moment and rolling moment.

We apply eigenstructure assignment to the design of a flight control system for the ICE tailless aircraft that includes thrust vectoring. Our longitudinal controller is a cstar command system and our lateral controller is a stability axis roll rate command system. Our design achieves MIL-F-8785C mode specifications on the short period, phugoid, dutch roll, roll subsidence and spiral modes, and achieves MIL-F-9490D specifications on phase and gain margins. The performance of the flight control system is evaluated by using a 6DOF nonlinear simulation of the ICE aircraft.

Jiang[13] proposed a method for reconfiguration using eigenstructure assignment. Jiang[13] chooses the eigenvectors of the reconfigured system using an orthogonal projection onto the space spanned by the eigenvectors of the original unfailed system. Jiang[13] applies his method to a fourth order linearized longitudinal model of an aircraft. However, he uses elevator and throttle as control effectors even though these two effectors have very different time scales. A more typical longitudinal flight control system would use a single input model with only elevator. The pilot usually commands throttle for speed control. Furthermore, his failure is chosen to be a change in several of the entries of the matrices (A,B,C) that describe the linearized dynamics. We believe that it is unclear what type of failure is described by this choice.

Konstantopoulos [14] proposes an optimization using a complicated performance index. This index includes terms for (1) minimizing the norm between the original and the failed eigenvectors, (2) enforcing the eigenvalue/eigenvector relationship, (3) a Lyapunov equation, and (4) the trace of the solution to the Lyapunov equation. However, such a method will require much more computation time than the direct method of Jiang [13]. Konstantopoulos[14] applies his method to Jiang's [13] longitudinal example. Then, he considers the fourth order linearized dynamics of an aircraft with full state feedback. His failure is chosen to be a change in two of the three aileron control derivatives. Again, we believe that it is unclear what type of failure is described by this choice.

Ashari et al. [15] propose an alternative optimization that is solved using a genetic algorithm. Ashari et al. [15] apply their method to Jiang's [13] longitudinal example. The authors [15] also consider the linearized dynamics of an aircraft, but the failure is the removal of the aileron actuator dynamics from the linearized model. We suggest that this does not represent any realistic failure.

The control systems of Refs. [10], [13], [14], [15] were designed in continuous time whereas they will probably be implemented on a digital computer. Piou and Sobel [16] extended eigenstructure assignment to linear time-invariant plants that are represented by Middleton and Goodwin's[17] unified delta model that is valid for continuous time and sampled data operation. An important property of the delta model is that the discrete time eigenvalues approach the continuous time eigenvalues as the sampling period approaches zero.

We extend our continuous time eigenstructure assignment design to the delta operator model. We present three new mathematical results. First, we derive an expression for the $\gamma - plane$ eigenvalues of the delta operator system as a function of damping ratio and natural frequency. Second, we show that a failure in continuous time body axes is equivalent to the same failure in delta operator stability axes.

Third, we extend disk gain and phase margins to the delta operator system. We consider symmetric lock in place failures of either the elevons or the all moving tips. We propose a novel eigenstructure assignment reconfiguration in which we first switch to a new recomputed gain to achieve satisfactory time responses. Then, we perform an optimization to achieve specifications on the disk gain and phase margins. We then switch to a second set of gains when the optimization achieves a feasible solution. We present simulation results using a full 6DOF nonlinear simulation. We show that an all moving tip failure causes the aircraft to become unstable whereas our reconfigured eigenstructure assignment reconfigured flight control system yields responses that are similar to the unfailed responses. We also show that an elevon failure requires the feasible solution from an optimization to satisfy the disk gain and phase margin specifications in all channels.

1.1.2 Fault Detection and Isolation

Multiple fault detection and isolation (FDI) system design by a single diagnostic observer was possible due to the development of detection filters originally proposed by Beard [18] and Jones [19]. Detection filters are a special class of observers that are designed to generate fixed directional residuals. These residuals can be easily associated with some known failure mode.

White and Speyer [20] reformulated the development of Beard [18] and Jones [19] in an eigenstructure assignment framework based on the additional freedom offered in multivariable systems (beyond eigenvalue assignment) of assigning eigenvectors to achieve the required system performance [21]. White and Speyer [20] showed that the eigenstructure assignment approach to fixed directional residual design allows for a systematic calculation of the detection filter gains and the closed-loop eigenvectors once the closed-loop eigenvalues have been assigned. In addition, White and Speyer

[20] demostrated that detection filters can be completely defined by specification of a set of closed-loop eigenvalues along with appropriate constraints on the eigenvectors.

Chen and Nagarajaia [22] used eigenstructure assignment in conjunction with the Linear-Matrix-Inequality technique to find the optimal detection filter gains so that the noise effect on the residual is reduced. Li and Jaimoukha [23] derived an algorithm for minimizing the effect of disturbances on the residual. The development in [23] generalizes the results of Douglas and Speyer [24] and Liu and Si [25]. The algorithms proposed in [22] and [23] were applied to a continuous-time linearized longitudinal model of the F16XL aircraft.

Shen et al. [26] presented an eigenvector selection criterion to provide robustness to unstructured uncertainties and initial condition mismatches to fixed directional residuals that are suitable for detection and isolation of multiple faults when they occur simultaneously. Shen et al. [26] first described how to assign the left eigenvectors to confine the effect of each failure on the residual to a different fixed direction in the output space and how to choose a projection matrix in order to diagonalize the residual/fault map. Then, Shen et al. [26] presented their eigenvector selection criterion which is the minimization of the condition number. Shen et al. [26] applied their algorithm for multiple and simultaneous FDI to the linearized longitudinal dynamics of a VTOL aircraft in the vertical plane. Simulations in [26] subject the VTOL aircraft to an initial mismatch in three of the four aircraft states and to bias actuator failures.

We extend multiple and simultaneous fault detection and isolation (FDI) system design by a single diagnostic observer to the delta operator model that is valid for both continuous time and sampled data operation. First, we reformulate the detection filter problem and detectability conditions for delta operator systems. Then, we use an eigenstructure framework to extend fixed directional residuals to delta operator systems and establish the conditions for allowable failures for the delta operator model. We present a new projection matrix W to diagonalize the failure/residual map for delta operator systems. We present a new mathematical result that reveals the independence of the projection matrix from the observer's eigenvectors. This mathematical result shows that unlike the development in [26], the projection matrix of the diagnostic observer is completely independent from the optimization's choice of eigenvectors. Furthermore, the projection matrix is completely defined by the observer's eigenvalues, output coefficient matrix, and failure signature matrix. We extend a result proven by Moore [21] for computing the observer gains to the delta operator model. Then, we present a new result for the delta operator model fault free residual bound and use it to propose a new eigenvector selection criterion for robust FDI to unstructured uncertainty and known initial condition mismatches.

Based on these mathematical results, we propose a new method/algorithm for multiple and simultaneous FDI of actuator failures for delta operator systems. This novel method involves the selection of eigenvalues for the diagnostic observer, the calculation of the projection matrix W which is eigenvector independent, a coordinate transformation which is defined by the failure signature matrix, the construction of subspaces for allowable eigenvectors to satisfy FDI conditions, and an eigenvector selection criterion for FDI robustness that is determined by the unconstrained optimization of a three-termed weighted performance index.

We consider the linearized longitudinal dynamics of a VTOL aircraft in the vertical plane described in [27] to implement our FDI algorithm for delta operator systems. We subject the aircraft to an initial condition mismatch in the vertical velocity state and bias actuator failures of the pitch control and the longitudinal pitch control. We examine the algorithm results from multiple optimization runs and their time responses corresponding to the combined and separate effect of initial mismatch and actuator failures for all runs.

We show that eigenstructure-based optimizations can lead to different sets of eigenvectors that minimize the performance index. These different sets of eigenvectors yield time responses that vary significantly which is problematic when there is a need to impose a threshold over the optimal time responses as is the case of FDI signals. This fact has not been addressed in literature on eigenstructure-based optimizations for fixed directional residual design. In contrast, our optimization and simulation results show that our FDI algorithm yields different sets of eigenvectors that minimize the performance index, satisfy FDI design requirements, have low condition number, and result in excellent and tightly similar residual responses with a detection time of about 4ms for 1ms sampled data for all runs.

1.2 Historical Review

1.2.1 Eigenstructure Assignment for Linear Systems

Consider an aircraft modeled by the linear time invariant matrix differential equation described by

$$\dot{x}(t) = Ax(t) + Bu(t) \tag{1.1}$$

$$y(t) = Cx(t) \tag{1.2}$$

where x is the state vector $(n \times 1)$, u the control vector $(m \times 1)$ and y the output vector $(r \times 1)$. It is assumed that the m inputs and the r outputs are independent.

Also, as is usually the case with aircraft, it is asssumed that $m < r < n$. If there are no pilot commands, the feedback control vector u equals a matrix times the ouput vector y:

$$u(t) = -Fy(t) \tag{1.3}$$

The feedback problem can be stated as follows: given a set of desired eigenvalues (λ_i^d), i=1,2,...,r and a corresponding set of desired eigenvectors, (v_i^d), i=1,2,...,r, find the real m x r matrix F such that the eigenvalues of A-BFC contain (λ_i^d) as a subset, and the corresponding eigenvectors of A-BFC are close to the respective members of the set (v_i^d).

Srinathkumar [28] has shown that if (A,B) is a controllable pair then the feedback gain F will exactly assign r eigenvalues. It will also assign the corresponding eigenvectors, provided that (v_i^d) is chosen to be in the subspace spanned by the columns of $(\lambda_i I - A)^{-1}B$ for i=1,2,...,r. This subspace is of dimension m, which is the number of independent control variables. A numerically superior representation for this subspace is described by Kautsky et al. [29], who showed that the subspace in which the eigenvector (v_i^d) must reside is also given by the nullspace of $U_1^T(\lambda_i I - A)$. Let L_i be a matrix whose columns are a basis for this nullspace. The matrix U_1 is obtained from the singular value decomposition of B, which is given by

$$B = [U_0 \;\; U_1] \begin{bmatrix} \Sigma V^T \\ 0 \end{bmatrix} \tag{1.4}$$

If we choose an eigenvector v_i which lies precisely in the subspace spanned by the columns of L_i, it will be achieved exactly. In general, however, a desired eigenvector v_i^d will not reside in the prescribed subspace and hence cannot be achieved. Andry et al. [11] describe a way to find the "best possible choice" for an achievable eigenvector.

This best possible eigenvector is the projection of v_i^d onto the subspace spanned by the columns of L_i (in the least square sense). In many practical situations, complete specification of v_i is neither required nor known, but rather the designer is interested only in certain elements of the eigenvector. Thus, assume that v_i^d has the following structure:

$$v_i^d = [v_{i1}, \mathrm{x}, \mathrm{x}, \mathrm{x}, \mathrm{x}, v_{ij}, \mathrm{x}, \mathrm{x}, v_{in}]^T \tag{1.5}$$

where v_{ij} are designer specified components and x is an unspecified component. Define, as shown by Andry et al. [11], a reordering operation $\{\ \}^{R_i}$ such that

$$\{v_i^d\}^{R_i} = \begin{bmatrix} \ell_i \\ d_i \end{bmatrix} \tag{1.6}$$

where ℓ_i is a vector of specified components of v_i^d and d_i is a vector of unspecified components of v_i^d. The rows of the matrix L_i are also reordered to conform with the reordered components of v_i^d. Thus,

$$\{L_i\}^{R_i} = \begin{bmatrix} \tilde{L}_i \\ D_i \end{bmatrix} \tag{1.7}$$

Then, the acheivable eigenvector v_i^a is given by

$$v_i^a = L_i z_i \tag{1.8}$$

where $z_i = \tilde{L}_i^{\dagger} \ell_i$ and where $(\cdot)^{\dagger}$ denotes the appropriate pseudoinverse of $(\cdot)$.

The feedback gain matrix F is given by

$$F = -V_b \Sigma_b^{-1} U_{b0}^T (V\Lambda - AV) V_r \Sigma_r^{-1} U_{r0}^T \tag{1.9}$$

where the singular value decomposition of the matrices B and CV are given by

$$B = [U_{b0} \;\; U_{b1}] \begin{bmatrix} \Sigma_b V_b^T \\ 0 \end{bmatrix} \tag{1.10}$$

$$CV = [U_{r0} \;\; U_{r1}] \begin{bmatrix} \Sigma_r V_r^T \\ 0 \end{bmatrix} \tag{1.11}$$

and where Λ is an r x r diagonal matrix with entries λ_i, i=1,2,...,r.

1.2.2 Pseudo Control

Sobel and Lallman[30] proposed a pseudocontrol strategy based upon the singular value decomposition. We use this pseudocontrol strategy to reduce the number of ICE aircraft redundant control effectors so that the lateral pseudo inputs are yaw and roll moment and the longitudinal pseudo input is pitching moment. Once the design is complete the controller is mapped back into the original control space.

Consider an aircraft modeled by the linear time invariant matrix differential equation described by Eqs. (1.1) and (1.2). The singular value decomposition of the control distribution matrix B is given by

$$\begin{aligned} B &= U\Sigma V^T \\ &= [U_3 \;\; U_0] \begin{bmatrix} \Sigma_3 & \\ & 0 \end{bmatrix} \begin{bmatrix} V_3^T \\ V_0^T \end{bmatrix} \end{aligned} \tag{1.12}$$

where U is the matrix of left singular vectors, V is the matrix of right singular vectors, and Σ is a diagonal matrix containing the singular values in the order of descending magnitude.

Suppose we partition the matrix Σ_3 as follows:

$$\Sigma_3 = \begin{bmatrix} \sigma_1 & & & & & & & & \\ & \cdot & & & & & & & \\ & & \cdot & & & & & & \\ & & & \cdot & & & & & \\ & & & & \sigma_a & & & & \\ & & & & & \sigma_{a+1} & & & \\ & & & & & & \cdot & & \\ & & & & & & & \cdot & \\ & & & & & & & & \cdot \\ & & & & & & & & & \sigma_b \end{bmatrix} = \begin{bmatrix} \Sigma_1 & \\ & \Sigma_2 \end{bmatrix} \tag{1.13}$$

where

$$\sigma_b \leq \sigma_{b-1} \leq \cdots \leq \sigma_{a+1} \leq \epsilon \tag{1.14}$$

and where ϵ is not necessarily close to zero. Sobel and Lallman [30] show that partition of U_3 and V_3 conformally with Σ_3 results in Eq. (1.12) to be rewritten as follows:

$$B = \begin{bmatrix} U_1 & U_2 & U_0 \end{bmatrix} \begin{bmatrix} \Sigma_1 & & \\ & \Sigma_2 & \\ & & 0 \end{bmatrix} \begin{bmatrix} V_1^T \\ V_2^T \\ V_0^T \end{bmatrix} \tag{1.15}$$

Now, let the system with pseudocontrol δ be described by

$$\dot{x} = Ax + \tilde{B}\delta \tag{1.16}$$

$$y = Cx \tag{1.17}$$

where

$$\tilde{B} = U_1 \tag{1.18}$$

The pseudocontrol δ is computed for the system described by Eqs. (1.16)-(1.18). Then, the true control u for the system described by Eqs. (1.1) and (1.2) is given by

$$u = V_1\Sigma_1^{-1}\delta \tag{1.19}$$

To derive the inverse control mapping given by Eq.(1.19), Sobel and Lallman[30] observe that upon comparing Eqs. (1.1) and (1.16), it is required that,

$$Bu = \tilde{B}\delta \tag{1.20}$$

Solving for the true control u, Sobel and Lallman[30] obtain

$$u = B^{+}\tilde{B}\delta \tag{1.21}$$

where the pseudoinverse B^{+} may be written as [31]

$$B^{+} = V_3{\Sigma_3}^{-1}U_3^T \tag{1.22}$$

Upon combining Eqs. (1.18), (1.21) and (1.22) Sobel and Lallman[30] obtain

$$u = (V_3{\Sigma_3}^{-1}U_3^T)U_1\delta \tag{1.23}$$

Using Eq. (1.15)

$$u = \begin{bmatrix} V_1 & V_2 \end{bmatrix} \begin{bmatrix} \Sigma_1^{-1} & \\ & \Sigma_2^{-1} \end{bmatrix} \begin{bmatrix} U_1^T \\ U_2^T \end{bmatrix} U_1 \delta \tag{1.24}$$

Expand Eq. (1.24) to obtain

$$u = V_1 {\Sigma_1}^{-1} U_1^T U_1 \delta + V_2 {\Sigma_2}^{-1} U_2^T U_2 \delta \tag{1.25}$$

But, from the properties of singular value decomposition [31], Sobel and Lallman[30] have that U and V are unitary matrices. Hence

$$U_1^T U_1 = I \tag{1.26}$$

and

$$U_2^T U_1 = 0 \tag{1.27}$$

Thus, the mapping of the controller into the original control space is

$$u = V_1 {\Sigma_1}^{-1} \delta \tag{1.28}$$

1.2.3 Delta Operator Eigenstructure Assignment

Piou and Sobel [16] extended eigenstructure assignment to linear time-invariant plants that are represented by Middleton and Goodwin's [17] unified delta model that is valid both for continuous time and sampled data operation of the plant. An important property of the delta model is that the discrete time eigenvalues approach the continuous time eigenvalues as the sampling period approaches zero. Piou and Sobel [16] showed that the eigenvectors of the delta model are identical to the eigenvectors of the continuous time plant and derived an expression for the eigenstructure assignment feedback gain matrix for the delta model. Piou and Sobel [16] showed that, in the limit as the sampling period delta goes to zero, the delta feedback gain approaches the continuous time feedback gain.

Consider an aircraft modeled by the linear time invariant matrix differential equation described by Eqs.(1.1) and (1.2), where $x \in \mathbb{R}^n$ is the state vector; $u \in \mathbb{R}^m$ the input vector; $y \in \mathbb{R}^r$ the output vector; and A, B, and C are constant matrices.

The corresponding sampled data system, which is obtained by using Middleton and Goodwin's [17] delta operator, is

$$\delta x = A_\delta x + B_\delta u \tag{1.29}$$

$$y = Cx \tag{1.30}$$

where

$$A_\delta = \Omega A \tag{1.31}$$

$$B_\delta = \Omega B \tag{1.32}$$

$$\Omega = \frac{1}{\Delta}\int_0^\Delta e^{A\tau} d\tau \tag{1.33}$$

and where

$$\delta = (q-1)/\Delta \tag{1.34}$$

and where the shift operator q is defined by

$$qx_k = x_{k+1} \tag{1.35}$$

and where Δ is the sampling period.

The unified state space model proposed by Middleton and Goodwin [17] is valid for both the discrete and continuous time cases simultaneously. This unified model is described by

$$\rho x(t) = A_\rho x(t) + B_\rho u(t) \tag{1.36}$$

$$y(t) = Cx(t) \tag{1.37}$$

where

$$A_\rho = \begin{cases} A & \text{in continuous time} \\ A_\delta & \text{in discrete time} \end{cases} \tag{1.38}$$

$$B_\rho = \begin{cases} B & \text{in continuous time} \\ B_\delta & \text{in discrete time} \end{cases} \tag{1.39}$$

and where

$$\rho = \begin{cases} \frac{d}{dt} & \text{in continuous time} \\ \delta & \text{in discrete time} \end{cases} \tag{1.40}$$

If there are no pilot commands, the feedback control vector u equals a matrix times the ouput vector y:

$$u = F_\delta y \tag{1.41}$$

with $F_\delta \in \mathbb{R}^{mxr}$ such that the closed-loop system $A_\delta + B_\delta F_\delta C$ is asymptotically stable with $A_\delta + B_\delta F_\delta C$ nondefective and $r \geq m$. Let $\Lambda_{\delta r}$ be the $r \times r$ diagonal matrix whose entries are the assignable closed-loop eigenvalues and let M_r be the $n \times r$ matrix whose columns are the corresponding achievable eigenvectors. Then, the solution to

$$(A_\delta + B_\delta F_\delta C)M_r \quad = \quad M_r \Lambda_{\delta r} \tag{1.42}$$

is given by

$$F_\delta \quad = \quad V_\delta \Sigma_\delta^{-1} U_{\delta 0}^T (M_r \Lambda_{\delta r} - A_\delta M_r) V_r \Sigma_r^{-1} U_{r0}^T \tag{1.43}$$

where

$$B_\delta = [U_{\delta 0} \;\; U_{\delta 1}] \begin{bmatrix} \Sigma_\delta V_\delta^T \\ 0 \end{bmatrix} \tag{1.44}$$

and

$$CM_r = [U_{r0} \;\; U_{r1}] \begin{bmatrix} \Sigma_r V_r^T \\ 0 \end{bmatrix} \tag{1.45}$$

are the singular value decompositions of B_δ and CM_r, respectively. Furthemore, Piou and Sobel[16] show that when $\Delta \rightarrow 0$, F_δ in Eq.(1.43) → F in Eq(1.9).

1.2.4 Observer-Based Residual Generator for Multiple Fault Detection and Isolation - Shen et al.

Consider the nominal plant formulated as

$$x(k+1) = Gx(k) + Hu(k) + Kf(k) \tag{1.46}$$

$$y(k) = Cx(k) \tag{1.47}$$

where $x(k) \in \mathbb{R}^n$ is the state vector, $u(k) \in \mathbb{R}^m$ is the known control input vector, $y(k) \in \mathbb{R}^r$ is the vector of the measured signal, and $f(k) \in \mathbb{R}^p$ is the fault vector. G, H, C, and K are known matrices with proper dimensions; the term $Kf(k)$ models the fault effects acting on actuators or components.

The observer dynamics considered by Shen et al. [26] can be expressed as follows:

$$\hat{x}(k+1) = (G - LC)\hat{x}(k) + Hu(k) + Ly(k) \tag{1.48}$$

$$\hat{y} = C\hat{x}(k) \tag{1.49}$$

$$r(k) = W[y(k) - \hat{y}(k)] \tag{1.50}$$

where $r(k)$ is the residual vector for fault monitoring, $L(k) \in \mathbb{R}^{n\times r}$ is the observer feedback gain matrix, and W is a constant projection matrix to project residuals onto specific directions.

Let $S_{\lambda_i} = [\lambda_i I - G^T \quad C^T]$ and let there be a compatibly partitioned matrix

$$\Sigma_{\lambda_i} = \begin{bmatrix} N_{\lambda_i} \\ M_{\lambda_i} \end{bmatrix} \tag{1.51}$$

whose columns constitute the basis of $\mathcal{N}(S_{\lambda_i})$, where $\mathcal{N}(\cdot)$ denotes the null space of $(\cdot)$.

The numerical algorithm of allowable subspaces for FDI by fixed directional residuals for shift-operator systems proposed by Shen et al. [26] is as follows:

1. Determine a distinct self-conjugate eigenvalue set of $(G - LC)$.
2. Apply a coordinate transformation to the original plant (G, H, K, C) to parameterize the allowable eigenvectors and the observer feedback gain matrix L by α_i.
3. Construct eigenvector subspaces to satisfy conditions for FDI and obtain the assignable subspaces, the basis N_{λ_i} for p_i and M_{λ_i} for ξ_i in the original coordinate system for $i = 1, \ldots, p$ and $i = p + 1, \ldots, n$.
4. Arbitrarily determine a nonzero eigenvector parameterization vector α_i and calculate $p_i = N_{\lambda_i}\alpha_i$ and $\xi_i = M_{\lambda_i}\alpha_i$.
5. Calculate observer feedback matrix L and projection matrix W.

Shen et al. [26] noted that proper selection of parameterization by α_i in step 4, provides degrees of freedom to further enhance the robustness of the diagnostic observer to unstructured uncertainty. Therefore, Shen et al. [26] studied the fault free system subjected to unstructured uncertainties to develop a well-conditioned design for robust FDI by fixed directional residuals.

Shen et al. [26] concluded that the 2-norm of the residual vector due to uncertainties and initial condition mismatches can be reduced by minimizing the condition number of P. The authors in [26] also explained that the minimum condition number of the diagnostic observer's modal matrix $\kappa(P)$, can be approached by making the eigenstructure as orthonormal as possible. For that reason, Shen et al. [26] modified their numerical algorithm to include the rank-one updating method for the optimization of the condition number $\kappa(P)$ which yields a set of orthonormal eigenvectors.

The optimization approach by Shen et al. [26] is used to determine α_i in step 4 as follows:

1. Use the rank-one method to determine a P such that minimum condition number $\kappa(P)$ is approached.
2. Once the optimization is finished, use the optimal P to determine eigenvector parameterization vector α_i from $p_i = N_{\lambda_i}\alpha_i$ (note: an inverse is required).
3. Once α_i is determined, calculate ξ_i, L and W.

Note that the eigenvector selection criterion in [26] for FDI robustness to unstructured uncertainty and initial condition mismatches is the minimization of the condition number $\kappa(P)$ alone. Earlier results by Sobel and Banda [32] show however that minimizing the condition number of the modal matrix alone will not, in general, yield good error attenuation. The projection matrix W in [26] is defined in terms of the output coefficient matrix C, failure signature matrix K, and the observer's eigenvalues and eigenvectors. Thus, the projection matrix W in [26] is not independent from the optimization. Furthermore, the calculation of W for robust FDI in [26] leads to impractical cases as it requires the output coefficient matrix C to be square and invertible. The optimization approach in [26], builds a diagnostic observer's modal matrix P with an iteration process that involves inverses. Once P is determined, additional inverses are required to obtain parameter α_i.

1.3 Contributions of the Thesis

1.3.1 Nonlinear Simulation

- Developed a nonlinear 6DOF simulation for dynamic analysis and control design validation of the ICE tailless aircraft.
  - Modified the Aircraft Control Toolbox [3] to include look up tables with interpolation for approximately 20,000 values of the ICE aircraft aerodynamic coefficients [4].
  - Modified the force and moment equations to include yaw and pitch thrust vectoring.
  - Modified the trim program cost function to penalize nonzero trim bank angle and non-1g trim normal acceleration.
  - Added limiters on actuator deflections, deflection rates, and control system integrators.

1.3.2 Flight Control System Design

- Applied eigenstructure assignment to the design of a flight control system for the ICE tailless aircraft.
  - Linearized the aircraft in straight and level flight at an altitude of 15,000 feet and Mach number 0.4.
  - Designed flight control systems for the longitudinal and lateral dynamics.
    - Our longitudinal controller is a cstar [33] command system using symmetric pitch flaps and pitch thrust vectoring. The cstar quantity is a blend of normal acceleration at the pilot station and pitch rate.

    - Our lateral controller is a stability axis roll rate command system using right and left elevons, right and left all moving tips, and yaw thrust vectoring.

  - Used a control allocation scheme with weights so that the lateral pseudo inputs are yaw and roll moment and the longitudinal pseudo input is pitch moment.

  - Showed how to modify the desired eigenvalues to simultaneously achieve:

    - acceptable responses to pilot commands
    - stabilize the phugoid mode
    - satisfy MIL-F-8785C [34] mode specifications
    - satisfy MIL-F-9490D [35] specifications on phase and gain margins.

  - Showed time responses for our combined longitudinal/lateral flight control system using a 6DOF nonlinear simulation of the ICE aircraft.

1.3.3 Reconfigurable Control System

- Presented three new mathematical results.

  - Derived an expression for the $\gamma - plane$ eigenvalues of the delta operator system as a function of damping ratio and natural frequency.

  - Showed that a failure in continuous time body axes is equivalent to the same failure in delta operator stability axes.

  - Extended disk gain and phase margins to the delta operator system.

- Extended our continuous time eigenstructure assignment design of a flight control system for the ICE tailless aircraft to the delta operator model that is valid for both continuous time and sampled data operation.

- Studied the effect of the sampling period on the dutch roll damping, natural frequency, and phase margins to explain our choice of 25 samples/sec.

- Considered symmetric lock in place failures of either the elevons or the all moving tips.

- Proposed a novel eigenstructure assignment reconfiguration in which we first switch to a new recomputed gain to achieve satisfactory time responses. Then, we perform an optimization to achieve specifications on the disk gain and phase margins. We then switch to a second set of gains when the optimization achieves a feasible solution. This requires much less time than waiting for convergence to the optimal solution.

- Presented simulation results using a full 6DOF nonlinear simulation.
  - Showed that an all moving tips failure causes the aircraft to become unstable whereas our eigenstructure assignment reconfigured flight control system yields responses that are similar to the unfailed responses.
  - Showed that an elevon failure requires the feasible solution from an optimization to satisfy disk gain and phase margin specifications in all channels.

1.3.4 Fault Detection and Isolation

- Extended multiple and simultaneous fault detection and isolation (FDI) system design by a single diagnostic observer to the delta operator model.
  - Reformulated the detection filter problem and detectability conditions for delta operator systems.
  - Used an eigenstructure framework to extend fixed directional residuals to delta operator systems and establish the conditions for allowable failures

  for the delta operator model.

  - Presented a new mathematical result that reveals the independence of the projection matrix from the observer's eigenvectors and showed how to calculate the projection matrix W to diagonalize the failure/residual map for delta operator systems. This mathematical result shows that the projection matrix of the diagnostic observer is completely defined by the observer's eigenvalues, the output coefficient matrix and the failure signature matrix.
  - Extended a result proven by Moore [21] for computing the observer gains to the delta operator model.
  - Presented a new result for the delta operator model fault free residual bound and used it to propose a new eigenvector selection criterion for robust FDI to unstructured uncertainty and known initial condition mismatches.

- Proposed a new method/algorithm for multiple and simultaneous FDI of actuator failures for delta operator systems. This novel method involves (1) the selection of eigenvalues for the diagnostic observer, (2) the calculation of the projection matrix W which is eigenvector independent, (3) a coordinate transformation which is defined by the failure signature matrix, (4) the construction of subspaces for allowable eigenvectors to satisfy FDI conditions, and (5) an eigenvector selection criterion for FDI robustness that is determined by the unconstrained optimization of a three-termed weighted performance index.

- Applied our delta operator model-based algorithm for multiple FDI to the linearized longitudinal dynamics of a VTOL aircraft in the vertical plane under a known initial condition mismatch in the vertical velocity state and bias actuator failures of the pitch control and the longitudinal pitch control.

- Examined the algorithm results from multiple optimization runs and showed simulation results corresponding to the combined and separate effect of initial mismatch and actuator failures for all runs.

- Showed that eigenstructure-based optimizations can lead to different sets of eigenvectors that minimize the performance index and satisfy design requirements for multiple FDI by fixed directional residuals. These different sets of eigenvectors yield time responses that vary significantly which is problematic when there is a need to impose a threshold over the optimal time responses as is the case of FDI signals.

- Showed that our delta operator model-based FDI algorithm results in highly consistent residual responses. Our algorithm yields different sets of eigenvectors that minimize the performance index, satisfy FDI design requirements, have low condition number, and result in tightly similar residual responses with a detection time of about 4ms for 1ms sampled data for all runs.

1.4 Outline

Chapter 2 presents a flight control system design for a wind tunnel model of the innovative control effectors (ICE) tailless aircraft. First, the aircraft is linearized in straight and level flight at an altitude of 15,000 feet and Mach number 0.4. Then, eigenstructure assignment is used to simultaneously stabilize the phugoid mode, satisfy MIL-F-8785C mode specifications, and satisfy MIL-F-9490D phase and gain margin specifications. Finally, simulation results of the flight control system are presented using a full 6DOF nonlinear simulation.

Chapter 3 extends the ICE aircraft's continuous-time flight control system design to the unified delta operator model that is valid for both continuous time and sampled data operation, and a novel eigenstructure assignment reconfiguration for the flight control system is proposed. A new result that extends disk gain and phase margins to the delta operator system is proposed, symmetric lock in place failures of either the elevons or the all moving tips is considered, and a full 6DOF nonlinear simulation is used to demostrated the reconfiguration of the ICE aircraft's lateral actuators symmetric lock in place failures.

Chapter 4 presents the mathematical results that extend multiple and simultaneous fault detection and isolation (FDI) system design by a single diagnostic observer to the delta operator model. Then, a new method for multiple and simultaneous FDI of actuator failures for delta operator systems is proposed. Finally the linearized longitudinal dynamics of a VTOL aircraft in the vertical plane is considered to implement our novel FDI algorithm for delta operator systems.

Chapter 2

Eigenstructure Assignment for the Innovative Control Effectors Aircraft

2.1 Overview

We apply eigenstructure assignment to the design of a flight control system for a wind tunnel model of a tailless aircraft. The aircraft, known as the innovative control effectors (ICE) aircraft, has unconventional control surfaces plus pitch and yaw thrust vectoring. We linearize the aircraft in straight and level flight at an altitude of 15,000 feet and Mach number 0.4. Then, we separately design flight control systems for the longitudinal and lateral dynamics. We use a control allocation scheme with weights so that the lateral pseudo inputs are yaw and roll moment and the longitudinal pseudo input is pitching moment. In contrast to previous eigenstructure assignment designs for the ICE aircraft, we consider the phugoid mode, thrust vectoring, and stability margins. We show how to simultaneously stabilize the phugoid mode, satisfy MIL-F-8785C mode specifications, and satisfy MIL-F-9490D phase and gain margin specifications. We also use a cstar command system that is preferable to earlier pitch rate command systems. Finally, we present simulation results of the combined longitudinal/lateral flight control system using a full 6DOF nonlinear simulation with approximately 20,000 values for the aerodynamic coefficients. Our simulation includes limiters on actuator deflections, deflection rates, and control system integrators.

2.2 Flight Control System Design

ICE Linearized Model

We linearize the dynamics of the ICE aircraft at a speed of Mach 0.4 and an altitude of 15,000 feet. The state variables are velocity V_T (ft/s), angle of attack α (rad), pitch angle θ (rad), pitch rate q (rad/s), engine power level, sideslip angle β (rad), bank angle ϕ (rad), roll rate p (rad/s), and yaw rate r (rad/s). The control effectors are throttle δ_{th} (0-1), symmetric pitch flap δ_{pflap} (deg), left elevon δ_{el} (deg), right elevon δ_{er} (deg), left all moving tip δ_{amtl} (deg), right all moving tip δ_{amtr} (deg), pitch thrust vectoring δ_{ptv} (deg), and yaw thrust vectoring δ_{ytv}(deg). The deflection limits are $\mid \delta_{pflap} \mid \leq 30^\circ$, $\mid \delta_{elevon} \mid \leq 30^\circ$, $-30^\circ \leq \delta_{amt} \leq 60^\circ$, $\mid \delta_{ptv} \mid \leq 15^\circ$, $\mid \delta_{ytv} \mid \leq 15^\circ$. The deflection rate limits are $\mid \dot{\delta}_{pflap} \mid \leq 50$deg/s, $\mid \dot{\delta}_{elevon} \mid \leq 150$deg/s, $\mid \dot{\delta}_{amt} \mid \leq 150$deg/s, $\mid \dot{\delta}_{ptv} \mid \leq 60$deg/s, and $\mid \dot{\delta}_{ytv} \mid \leq 60$deg/s.

The dynamics are decoupled into longitudinal and lateral design models. The longitudinal states are V_T (ft/s), α (rad), θ (rad), q (rad/s), and integral of cstar $\int c^*$. Here, cstar [33], [36] is defined as $c^* = n_{zp} + 12.4q$ where n_{zp} is the normal acceleration at the pilot's station. The control effectors are symmetric pitch flap δ_{pflap} (deg) and pitch thrust vectoring δ_{ptv} (deg). The sensor measurements are α (deg), q (deg), and $n_{zp}(g)$. The lateral states are β (rad), ϕ (rad), p (rad/s), r (rad/s), and a yaw rate washout filter state x_{wo} with a one second time constant. The control effectors are left elevon δ_{el} (deg), right elevon δ_{er} (deg), left all moving tip δ_{amtl} (deg), right all moving tip δ_{amtr} (deg), and yaw thrust vectoring δ_{ytv}(deg). The sensor measurements are β (deg), roll rate p (deg/s), and yaw rate r (deg/s). In addition, we use longitudinal and lateral simulation models which are the design models augmented with first order actuator dynamics with time constant 0.049505 seconds.

Lateral Flight Control System

The open loop lateral eigenvalues and eigenvectors are shown in Table 2.1. We observe that the aircraft has two complex lateral modes with one of the modes being unstable. This is in sharp contrast to a conventional aircraft that exhibits a complex dutch roll mode, a real roll subsidence mode, and a real spiral mode. Furthermore, the eigenvectors indicate that both modes are strongly coupled and that neither mode can be identified as a dutch roll.

We transform the lateral dynamics from body axis to stability axis so that we can decouple stability axis roll rate p_s from sideslip angle. This is consistent with our choice of p_s as the pilot command. This transformation requires the value of trim alpha which is 0.1569 rad. The states are now sideslip angle β, bank angle ϕ, stability axis roll rate p_s, stability axis yaw rate r_s, and a washout filter state x_{wo}. We choose the lateral feedbacks to be β, p_s, and washed out stability axis yaw rate$(r_s)_{wo}$ which allows us to assign three eigenvalues. The military specifications [34], [37] for level 1, category A, class IV flight require (1) a maximum roll mode time constant of one second, (2) dutch roll minimum ζ_{dr} of 0.4, minimum $\zeta_{dr}\omega_n$ of 0.4 r/s, minimum $\omega_n = 1.0r/s$, and (3) stable spiral mode or unstable spiral mode with minimum time to double amplitude $T_2 > 12s$. The desired dutch roll and roll subsidence eigenvalues and eigenvectors are those suggested by Davidson and Andrisani [12] and are shown

Table 2.1: Eigenvalues and eigenvectors for the lateral dynamics[a]

	Open Loop			Desired Closed Loop		
Eigenvalues	$\lambda_{1,2}$=-0.5197±j0.4319			Dutch roll	$(\zeta_{dr}, \omega_{ndr}) = (0.4, 3)$	
	$\lambda_{3,4}$= 0.0200±j0.2251			Roll subsidence	$1/\tau_{roll} = -4$	
				Dutch roll	Roll subsidence	
Eigenvectors	0.0420±j0.0031	0.0065±j0.0244	β	1±j0	β/p	β
	0.8278	0.9735	ϕ	$\lvert\phi/\beta\rvert$±j0	x	ϕ
	-0.4332±j0.3514	0.0083±j0.2139	p	x±jx	1	p_s
	0.0178±j0.0389	0.0695±j0.0328	r	x±jx	x	r_s
				x±jx	x	x_{wo}

[a] Open loop is in body axis, no washout. Closed loop is in stability axis. $|\phi/\beta| = |\beta/p| = 0$.

in Table 2.1. We note that the desired eigenvalues satisfy the military specifications. Furthermore, we note that the dutch roll mode is a (β, r_s) mode that is decoupled from ϕ whereas the roll subsidence mode is a p_s mode that is decoupled from β.

We show the singular values of the control distribution matrix B_{stab} in Table 2.2. Observe that there are only two nonzero singular values which indicate that there are only two independent control directions. We use the first two columns of U_{stab} as the pseudocontrol distribution matrix. Column 1 corresponds to rolling moment δ_{roll} and column 2 corresponds to yawing moment δ_{yaw}.

We can generalize this method by adding weights to the five lateral control effectors. This will allow larger control deflections for the effectors with larger deflection limits and vice versa. Mathematically, let W contain the weights and consider the singular

Table 2.2: SVD of Lateral Control Distribution Matrix[a]

Left Singular Vectors U_{stab}					Singular Values
0.0003	-0.0134	0.9999	0.0000	β	0.1248
-0.0000	-0.0000	-0.0000	1.0000	ϕ	0.0279
0.9800	0.1992	0.0024	0.0000	p_s	0.0000
-0.1992	0.9799	0.0132	0.0000	r_s	0.0000

[a] After transformation to stability axis, no weights.

value decomposition

$$B_{stab}W = U_{stab}\Sigma_{stab}V_{stab}^T \tag{2.1}$$

Then,

$$\dot{x} = Ax + \tilde{B}\delta \tag{2.2}$$

where

$$\tilde{B} = U_{stab}(:, 1:2) \tag{2.3}$$

$$\delta = -\tilde{K}y = [\delta_{roll}, \delta_{yaw}]^T \tag{2.4}$$

Then, the inverse mapping to obtain the control u(t) is

$$u(t) = V_{stab}\Sigma_{stab}^{-1}\tilde{K}Wy(t) \tag{2.5}$$

The feedback gain matrix, achievable eigenvalues, and achievable eigenvectors are shown in Table 2.3. We observe that we have achieved the desired eigenvalues and eigenvectors. We also observe that the thrust vector gains are larger than the elevon and amt gains.

A linear simulation, that includes actuator dynamics, shows that the thrust vector

Table 2.3: Lateral Eigenstructure Assignment Design[a]

	Feedback Gain Matrix				Achievable Eigenvectors		Achievable Eigenvalues	
	β	p_s	$(r_s)_{wo}$		Dutch Roll	Roll Subsidence		
Unweighted B	-1.7256	0.2945	0.2292	elevonL	1±j0	0	$(\zeta_{dr}, \omega_{dr})$	= (0.4,3.0)
$\zeta_{dr} = 0.4$	1.7256	-0.2945	-0.2292	elevonR	0±j0	-0.2531	λ_{roll}	= -4
	0.7870	0.1188	-0.2387	amtL	0±j0.0001	1	λ_{spiral}	= 0.0077
	-0.7870	-0.1188	0.2387	amtR	1.1007±j2.8348	-0.0106	λ_{filter}	= -1.33
	7.7741	-0.4185	-1.5142	yawTV	-1.0545±j0.3236	0.0035		
Weighted B	-8.0478	0.6333	1.4730	elevonL	1±j0	0	$(\zeta_{dr}, \omega_{dr})$	= (0.4,3.0)
W=(1,1,1,1,0.25)	8.0478	-0.6333	-1.4730	elevonR	0±j0	-0.2531	λ_{roll}	= -4
$\zeta_{dr} = 0.4$	8.6966	-0.3052	-1.7949	amtL	0±j0.0001	1	λ_{spiral}	= 0.0077
	-8.6966	0.3052	1.7949	amtR	1.1166±j2.8222	-0.0120	λ_{filter}	= -1.34
	3.3934	-0.1820	-0.6667	yawTV	-1.0504±j0.3297	0.0040		

[a] Design model includes washout filter but no actuator dynamics.

deflection is larger than the elevon and amt deflections. This is undesirable because the thrust vector deflection limit is only 15 degrees whereas the elevon and amt deflection limits are 30 degrees. To remedy this problem we reduce the thrust vector weight in Eq.(2.1) while maintaining the other weights at unity. Table 2.3 shows the results for a thrust vector weight of 0.25 where we observe that the thrust vector gains are now smaller than the elevon and amt gains. A linear simulation shows that the maximum thrust vector deflection to a stability axis roll rate pulse is approximately 40% and 66% of the elevon and amt maximum deflections, respectively. We also observe from Table 2.3 that the spiral mode is unstable with eigenvalue $\lambda_{spiral} = 0.0077$. The time to double amplitude for the unstable spiral mode is given by [37]

$$T_2 = \frac{0.693}{unstableroot} = \frac{0.693}{0.0077} = 90sec \tag{2.6}$$

which satisfies the specification of $T_2 > 12$ seconds.

A block diagram of the lateral flight control system is shown in Figure 2.1. We have added a gain of 4/3 to the pilot stick for the purpose of achieving zero steady state error to a p_s command.

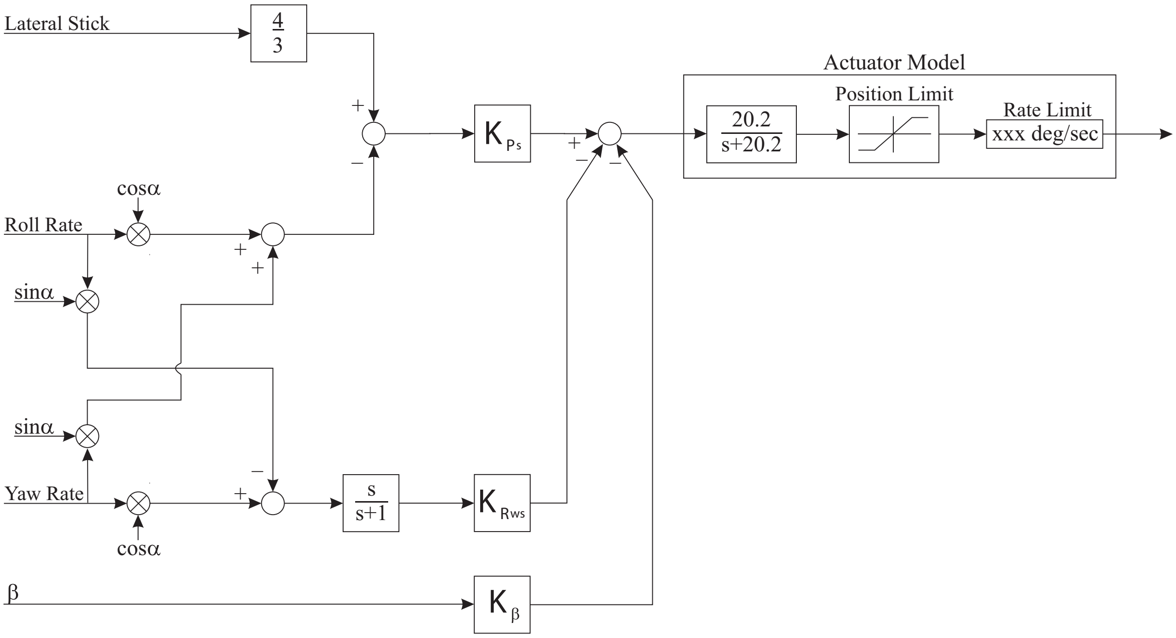

Figure 2.1: Block diagram of lateral flight control system

The linearized lateral time responses to a one degree initial sideslip are shown in Figure 2.2. We observe that the bank angle is appoximately 0.1 degree. This yields $| \phi/\beta | \approx 0.1$ which indicates excellent decoupling from sideslip to bank angle.

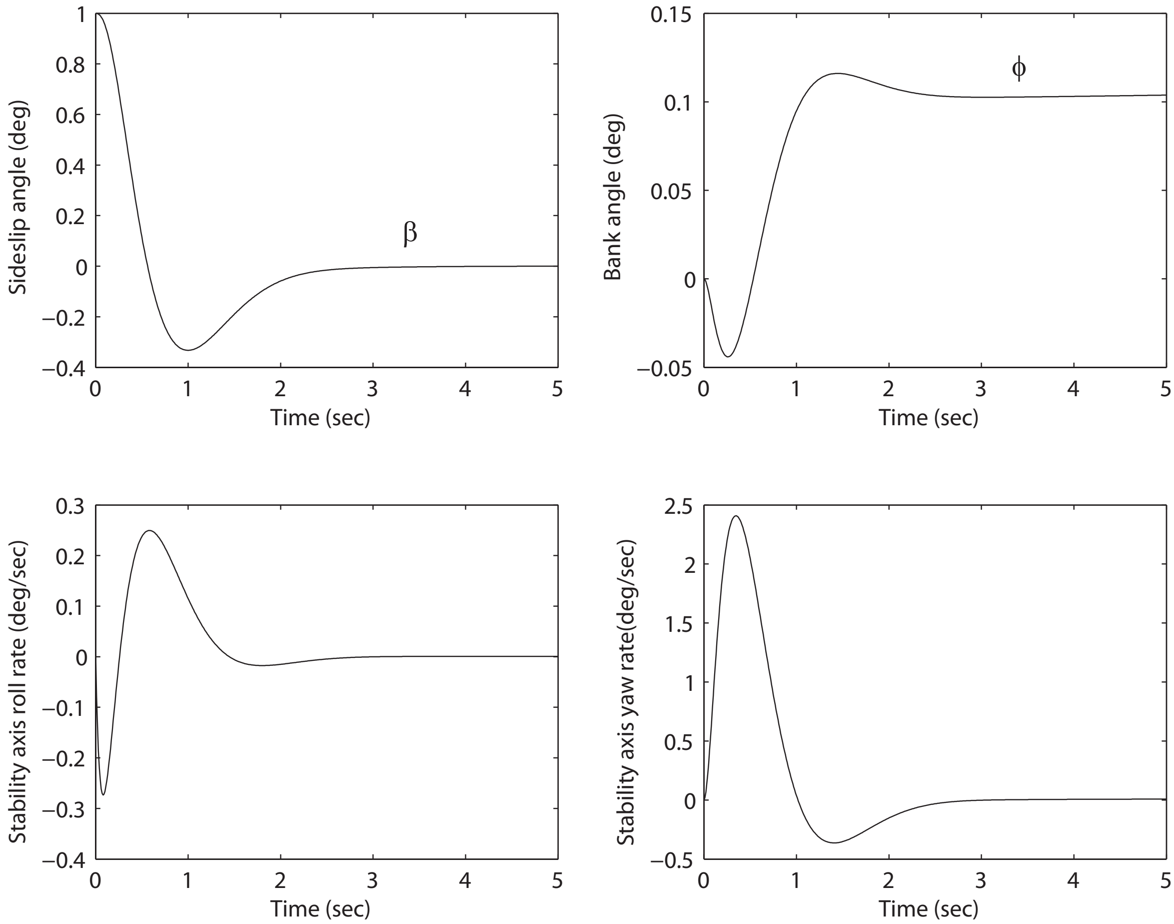

Figure 2.2: Linear time responses to a 1 deg initial sideslip

Longitudinal Flight Control System

The linearized longitudinal states are V_T, α, θ, q, and integral of cstar $\int c^*$. The open loop short period and phugoid modes exhibit natural frequencies and damping ratios given by $(\omega_{nsp}, \zeta_{sp})$=(1.10, 0.57) and $(\omega_{nph}, \zeta_{ph})$=(0.107, 0.11), respectively. The damping ratio specifications for the short period and phugoid modes for level 1, category A flight are [34] $0.35 \leq \zeta_{sp} \leq 1.30$ and $\zeta_{ph} \geq 0.04$, respectively. For small angles, the steady state load factor per steady state angle of attack is given by [38]

$$\frac{n}{\alpha} = \frac{V_{trim} L_{\alpha}}{g} \approx \frac{-U_0 Z_w}{g} \tag{2.7}$$

For our linearized longitudinal dynamics, the trim velocity V_{trim}=422.96 ft/s, Z_w=-0.5972 which yields $n/\alpha = 7.85$. Using MIL-F-8785C [34] with n/α=7.85 we find that the specification for the short period natural frequency is $1.6 \leq \omega_{nsp} \leq 5.5$. We note that the open loop aircraft does not meet the specification on ω_{nsp}.

We show the singular values of the control distribution matrix B_{long} in Table 2.4. Observe that although there are two nonzero singular values, the second singular value is ten times smaller than the first singular value. This indicates that there is only one strongly independent control direction which corresponds to pitch moment denoted by δ_{pitch}.

Table 2.4: SVD of Longitudinal Control Distribution Matrix[a]

Left Singular Vectors						Singular Values
-0.0028	-0.0169	0	-0.9623	0.2714	u	0.0548
-0.0121	-0.0429	0	-0.2704	-0.9617	α	0.0057
0	0	1	0	0	θ	
-0.9201	-0.3906	0	0.0164	0.0244	q	
0.3915	-0.9194	0	0.0233	0.0295	$\int$c*	

[a] V_T replaced by normalized velocity u, no weights.

We use the first column of U_{long} as the pseudocontrol distribution matrix. Therefore, this is a single input problem which allows eigenvalue but not eigenvector assignment. We add the weights (1, 0.65) so that δ_{pflap} will have maxmium deflection of approximately twice the δ_{ptv} deflection. This choice is because the pitch flap has a deflection limit that is twice the thrust vector deflection limit. Mathematically, let W contain the weights and consider the singular value decomposition

$$B_{long}W = U_{long}\Sigma_{long}V_{long}^{T} \tag{2.8}$$

Then,

$$\dot{x} = Ax + \tilde{B}\delta \tag{2.9}$$

where

$$\tilde{B} = U_{long}(:,1) \tag{2.10}$$

$$\delta_{pitch} = -\tilde{K}y \tag{2.11}$$

Then, the inverse mapping to obtain the gain K_0 for the control $u(t) = -K_0 y(t)$ is

$$K_0 = V_{long}\Sigma_{long}^{-1}\tilde{K}W \tag{2.12}$$

We choose the feedbacks to be c^*, q, and $\int c^*$. This causes the aircraft longitudinal dynamics to have an output vector y=Cx+Du with a nonzero matrix D. To apply eigenstructure assignment to these dynamics, we first compute K_0 from Eq.(2.12) with D=0. Then, it can be easily shown that the feedback gain matrix K_D for nonzero D is given by

$$K_D = (I - K_0 D)^{-1} K_0 \tag{2.13}$$

We can assign three eigenvalues because we have three outputs. We begin our design with the short period values that are used by Yechout [37] which are ζ_{sp}=0.7 and ω_{nsp}=3.98. The cstar response is slow so we change the short period natural frequency and damping to ζ_{sp}=0.6 and ω_{nsp}=5.00. This yields an improved cstar response. For the integrator mode we begin with λ_{int}=-1 which is approximately the value used by Stevens and Lewis [36].

Velocity and bank angle are not usually fed back for inner loop control such as a stability augmentation system (SAS) or command augmentation system (CAS). We find that it is difficult to simultaneously achieve short period and phugoid specifications for the ICE aircraft when feeding back c^*, q, and $\int c^*$. We found that to stabilize the phugoid mode it is necessary but not sufficient to feed back angle of attack. However, we do not want to add a fourth output to the eigenstructure assignment because we do not have a fourth eigenvalue to assign. The modes that we are assigning are the short period and the integrator. So we chose to replace c^* with $c^* + \alpha$. We can separate out the c^* and α gains from the gains computed by eigenstructure assignment. We further found that the phugoid was unstable even with the α feedback when the integrator eigenvalue was assigned to λ_{int}=-1. We moved the integrator eigenvalue closer to the origin and the phugoid mode was stabilized with ζ_{ph}=0.053 when λ_{int}=-0.38. This achieves the phugoid damping specifications, but the gain and phase margins were too small in the δ_{pflap}, δ_{ptv}, α, and $\int c^*$ loops. Finally, we achieved the short period, phugoid, and gain/phase margin specifications by assigning the integrator mode at λ_{int}=-0.25. The phugoid mode exhibits a natural frequency and damping ratio given by $(\omega_{nph}, \zeta_{ph})$=(0.01, 0.7). The feedback gain matrix and the disk gain/phase margins are shown in Tables 2.5 and 2.6, respectively.

Table 2.5: Longitudinal feedback gain matrix K_D

c^*	α	q	$\int c^*$	
-5.59	-5.59	-0.4979	8.32	δ_{pf}
-2.89	-2.89	-0.2574	4.30	δ_{ptv}

Table 2.6: Longitudinal Disk Gain/Phase Margins[a]

	Gain Margin (db)	Phase Margin (deg)	Frequency (r/s)
δ_{pf}	±14.68	±69.09	7.87
δ_{ptv}	±26.02	±84.28	9.95
c*	±28.92	±85.90	17.08
α	± 5.33	±33.15	0.0085
q	±29.22	±86.04	17.44
$\int$c*	± 4.81	±30.23	0.0097

[a] Gain and phase margins use model with actuator dynamics.

However, the cstar response was not inside the cstar response envelope [33]. This was because the integrator mode caused the response to be too slow. To remedy this problem. We add a lead compensator in series with the pitch stick. We found that a good cstar response was obtained with the compensator 5(s+0.5)/(s+2). A block diagram of the longitudinal flight control system is shown in Figure 2.3.

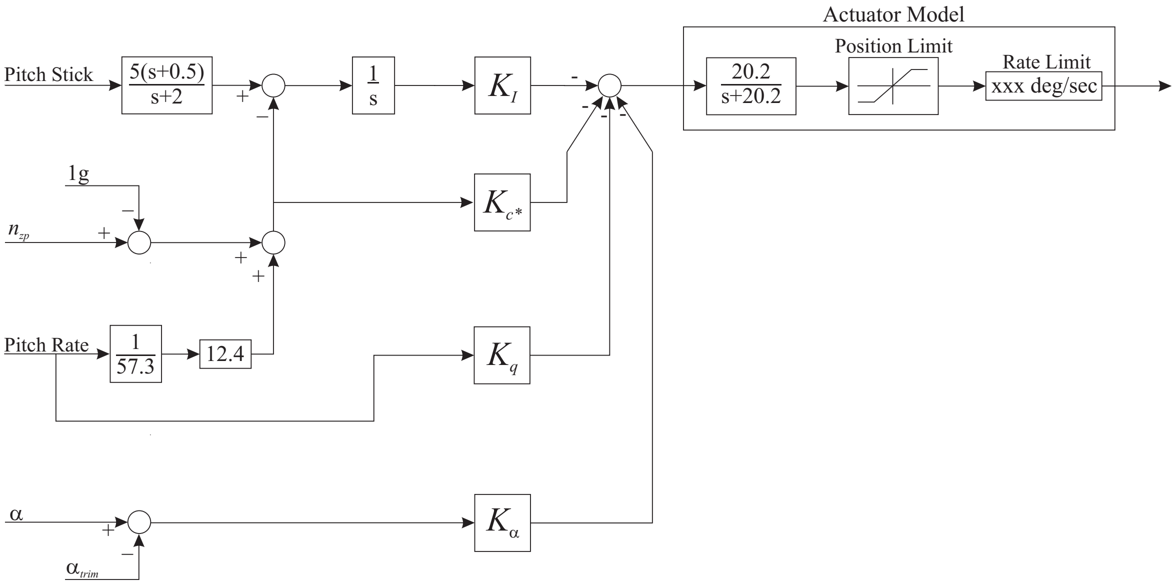

Figure 2.3: Block diagram of longitudinal flight control system

2.3 Robustness Results

a. Stability Robustness

We analyze the stability robustness of the design using open loop phase and gain margins. We use the linearized simulation model that includes actuator dynamics.We use function loopmargin from the MATLAB Robust Control Toolbox [39] to compute the disk margins. The disk margins represent the largest region for each channel such that the closed loop system is stable for all gain and phase variations inside the region. The disk margin analysis allows for simultaneous gain and phase variations one loop at a time.

a.1. Lateral dynamics

The unstable open loop complex mode poses a problem for gain and phase margin calculation. For a conventional aircraft with a real unstable spiral mode we would use a similarity transformation to decouple the spiral mode. Then, we would obtain gain and phase margins for the reduced order model that does not include the spiral mode. Unfortunately, the best that can be done here is to remove the bank angle equation from the open loop aircraft. This results in closed loop eigenvalues that are approximately the same for the model with the bank angle equation except for the absense of the spiral mode. We believe that this is acceptable especially because we use disk margins for simultaneous gain and phase variation whereas MIL-F-9490D [35] specifies either gain or phase variation. Thus, our analysis is conservative with respect to the specifications. The disk margins are shown in Table 2.7 where we observe that the specifications are acheived for all loops except the sideslip loop.

Table 2.7: Lateral Disk Gain/Phase Margins[a]

		Gain Margin(db)	Phase Margin(deg)	Frequency(r/s)
Specifications		±4.5	±30	ω <0.377
		±6.0	±45	0.377< ω < 1st bending mode
δ_{dr}=0.4	δ_{elevon}	±18.95	±77.13	2.51
	δ_{amt}	±10.18	±55.58	3.52
	δ_{yawTV}	±13.30	±65.59	4.12
	β	± 4.78	±30.02	3.10
	p_s	±20.61	±79.35	10.60
	$(r_s)_{wo}$	±13.58	±66.34	2.51
δ_{dr}=0.707	δ_{elevon}	±35.29	±88.03	20.63
	δ_{amt}	±18.96	±77.14	7.07
	δ_{yawTV}	±20.63	±79.37	9.73
	β	± 7.72	±45.31	3.53
	p_s	±20.58	±79.30	10.96
	$(r_s)_{wo}$	±13.57	±66.32	1.80

[a] Weighted B with W=(1,1,1,1,0.25)

We found that increasing the dutch roll damping improved the sideslip loop margins. We choose the dutch roll damping to be $\zeta_{dr} = 0.7$ which yields a sideslip loop phase margin of ±45.31 degrees as compared with the specification of ±45 degrees. The new feedback gains are shown in Table 2.8 where we observe that the gain magnitudes are larger for $\zeta_{dr} = 0.7$ as compared to the gain magnitudes for $\zeta_{dr} = 0.4$ in Table 2.3.

a.2. Longitudinal dynamics

Longitudinal disk gain and phase margins are shown in Table 2.6. We observe that MIL-F-9490D specifications are satisfied in all channels.

Table 2.8: Lateral Eigenstructure Assignment Design[a]

	Feedback Gain Matrix				Achievable Eigenvectors		Achievable Eigenvalues	
	β	p_s	$(r_s)_{wo}$		Dutch Roll	Roll Subsidence		
Weighted B	-10.5499	0.6535	2.7356	elevonL	1±j0	0	$(\zeta_{dr}, \omega_{dr})$	= (0.707,3.0)
W=(1,1,1,1,0.25)	10.5499	-0.6535	-2.7356	elevonR	0±j0	-0.2531	λ_{roll}	= -4
$\zeta_{dr} = 0.707$	11.8373	-0.3307	-3.3928	amtL	0±j0	1	λ_{spiral}	= 0.0077
	-11.8373	0.3307	3.3928	amtR	2.1068±j2.2247	-0.0120	λ_{filter}	= -1.84
	4.5464	-0.1913	-1.2514	yawTV	-1.2299±j0.3432	0.004		

[a] Design model includes washout filter but no actuator dynamics.

b. Performance Robustness

We analyze performance robustness to the real uncertainty in the stability and control derivatives by performing a monte carlo simulation. The uncertainty in each parameter is uniformly distributed and independent of the other parameters. We separately use the linearized lateral/longitudinal simulation models that include first order actuator dynamics. We perform 100 runs of the linearized lateral/longitudinal dynamics over the real uncertainty in the stability and control derivatives. This is accomplished by using functions ureal and usample from the MATLAB Robust Control Toolbox [39].

b.1. Lateral dynamics:

The uncertainty in the stability derivatives is given by [5] $Y_\beta = 15\%$, $L_\beta = 10\%$, $L_p = 30\%$, $L_r = 20\%$, $N_\beta = 30\%$, $N_p = 50\%$, and $N_r = 15\%$. The uncertainty is 15% in all control derivatives.

The responses to a one deg/s stability axis roll rate pulse command are shown in Figure 2.4. We observe that the responses are well behaved for all uncertainty and

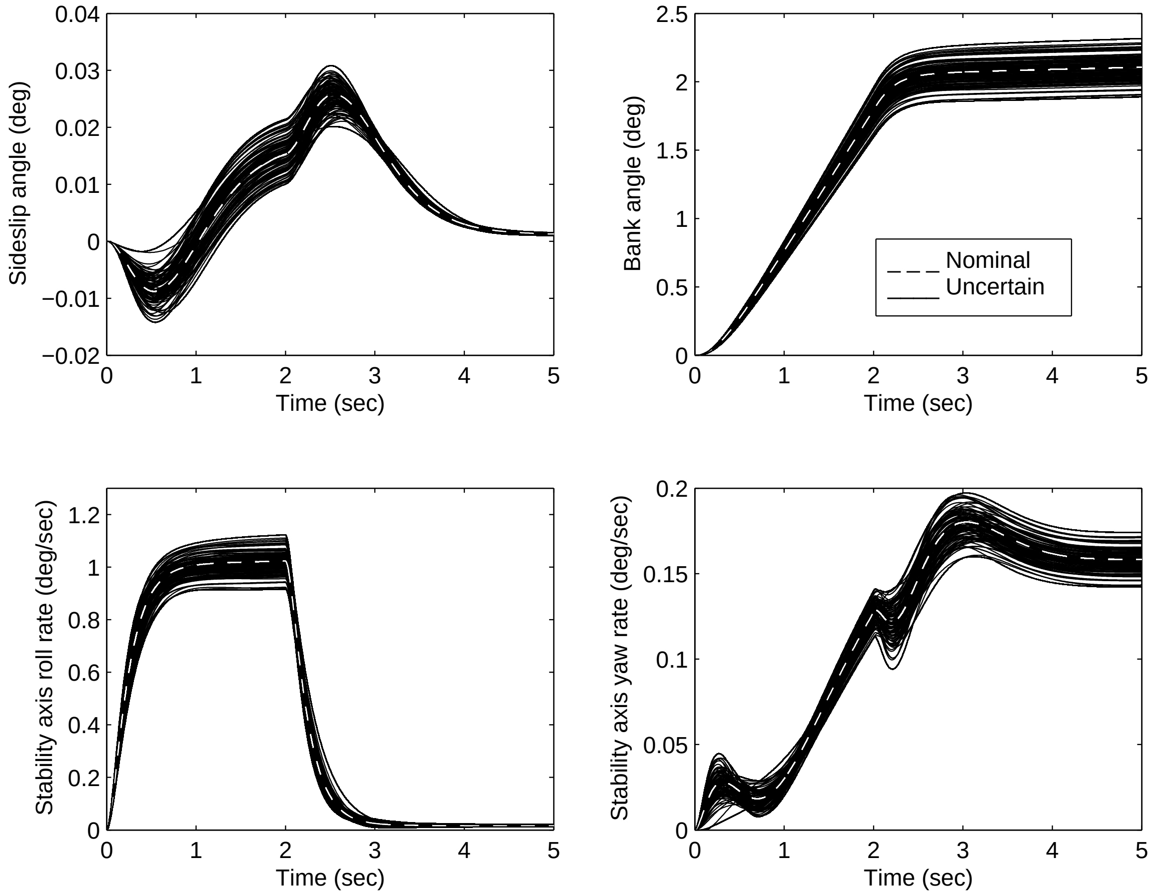

Figure 2.4: Monte carlo simulation for lateral dynamics

that deviations from nominal indicate a robust design.

b.2. Longitudinal dynamics:

The uncertainty in the longitudinal stability derivatives is given by [5] $Z_\alpha = 2\%$, and $M_\alpha = 4\%$. The uncertainty is 15% in all control derivatives. The uncertain stability and control derivatives also appear in the output equation for n_{zp}. The normal acceleration equation from the numerical linearization is given by

$$n_{zp} = 0.0048V_T + 7.604\alpha - 0.3417q - 0.0094\delta_{pflap} - 0.0200\delta_{ptv} \tag{2.14}$$

However, Eq.(2.14) does not show the dependence of n_{zp} on Z_α, M_α, Z_{pflap}, M_{pflap}, Z_{ptv}, or M_{ptv}. Thus, we consider the algebraic equation for n_{zp} given by

$$n_{zp} \approx \frac{V_{trim}}{g}(q - \dot{\alpha}) + \frac{\ell}{g}\dot{q} \tag{2.15}$$

where V_{trim}=422.96 ft/s, g=32.17 ft/s^2, and ℓ =17 ft. Upon substituting the $\dot{\alpha}$ and $\dot{q}$ equations into Eq.(2.15) we obtain

$$\begin{aligned} n_{zp} \approx 0.00537V_T + [(-(V_{trim}\, Z_\alpha) + (\ell\, M_\alpha))/g]\alpha \ - 0.3417q \\ +[(-(V_{trim}\, Z_{pflap} + (\ell\, M_{pflap}))/g]\delta_{pflap} \\ +[(-(V_{trim}\, Z_{ptv}) + (\ell\, M_{ptv}))/g]\delta_{ptv} \end{aligned} \tag{2.16}$$

We evaluate Eq.(2.16) at the nominal values of Z_α, M_α, Z_{pflap}, M_{pflap}, Z_{ptv}, and M_{ptv} which yields

$$n_{zp} \approx 0.00537V_T + 7.3988\alpha - 0.3417q - 0.009814\delta_{pflap} - 0.01472\delta_{ptv} \tag{2.17}$$

We observe that the nominal coefficients in Eqs.(2.14) and (2.17) are slightly different. We add the difference in the coefficients to Eq.(2.16) so that the nominal value of the coefficients will be those shown in Eq.(2.14). Then, the equation for n_{zp} that is used in the monte carlo simulation is given by

$$\begin{aligned} n_{zp} \approx 0.0048V_T + [(-(V_{trim}\, Z_\alpha) + (\ell\, M_\alpha))/g \ + 0.2052]\alpha \ - 0.3417q \\ +[(-(V_{trim}\, Z_{pflap} + (\ell\, M_{pflap}))/g \ + 0.000364]\delta_{pflap} \\ +[(-(V_{trim}\, Z_{ptv}) + (\ell\, M_{ptv}))/g \ - 0.00528]\delta_{ptv} \end{aligned} \tag{2.18}$$

The responses to a one g step command in cstar are shown in Figure 2.5. We observe that the responses are well behaved for all uncertainty and that deviations from nominal indicate a robust design.

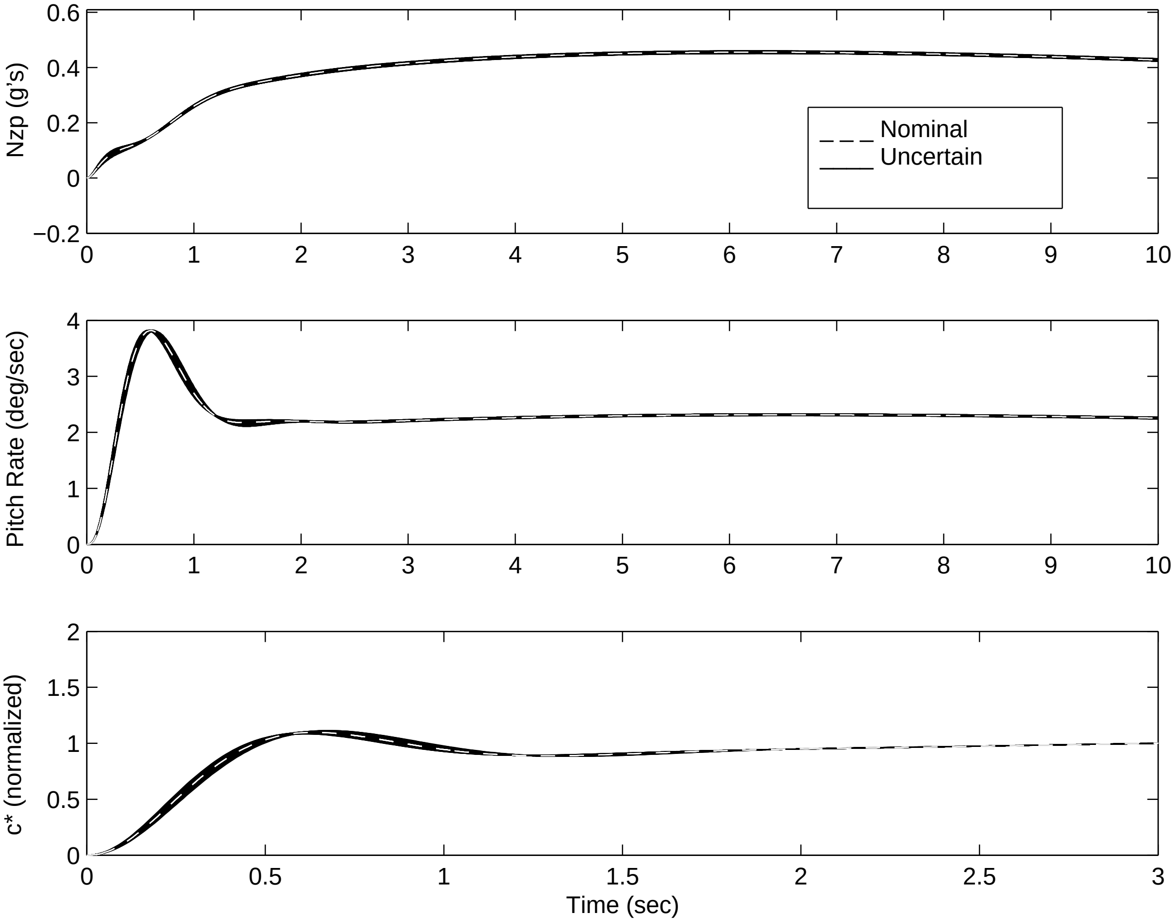

Figure 2.5: Monte carlo simulation for longitudinal dynamics

2.4 Nonlinear Simulation Results

We perform time responses using the linearized lateral simulation model that includes actuator dynamics and the full 6DOF nonlinear model with deflection and deflection rate limits. The nonlinear simulation includes both the lateral and longitudinal controllers.

Figure 2.6 shows the lateral linearized (dashed line) and the nonlinear (solid line) responses to 1 deg/s stability axis roll rate pulse for $0 \leq t \leq 2$ sec. We observe that (1) sideslip is less than 0.03 deg, (2) steady state bank angle is 2.3 deg, and (3) steady state stability axis yaw rate is 0.17 deg/s. We also observe that the linear and nonlinear responses are almost identical.

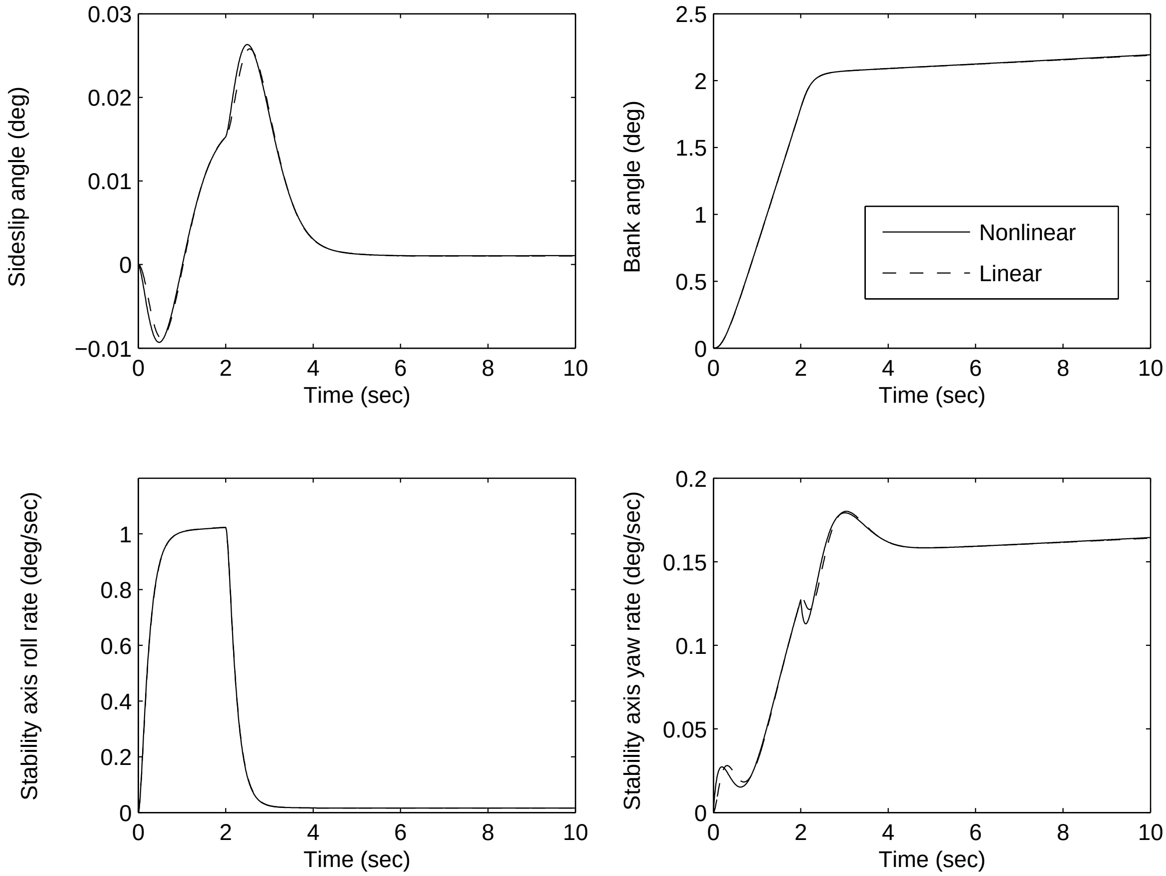

Figure 2.6: Nonlinear time responses to a 1 deg/s p_s pulse

Figure 2.7 shows the control effector deflections. We observe that (1) maximum elevon deflection is 0.7 deg, (2) maximum amt deflection is 0.3 deg, and (3) maximum yaw thrust vector deflection is 0.2 deg. We conclude that the nonlinear responses are excellent.

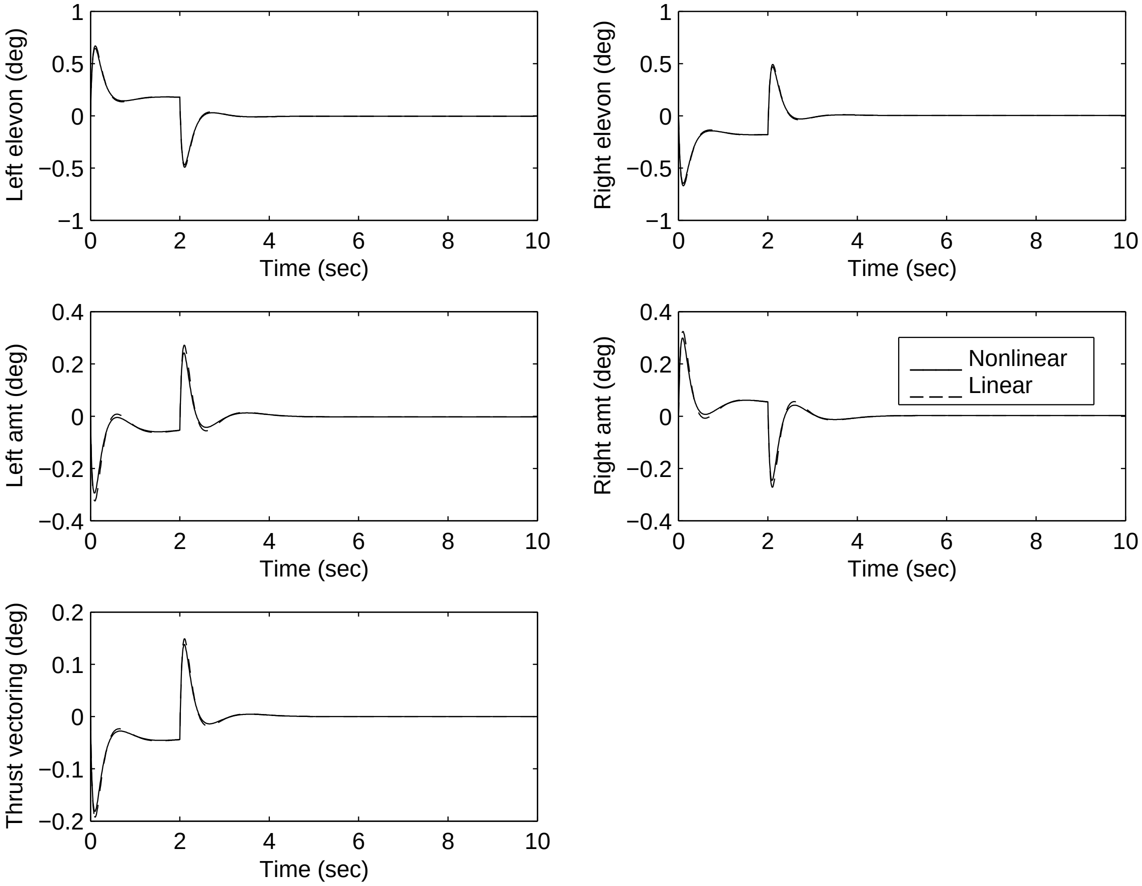

Figure 2.7: Nonlinear control responses to a 1 deg/s p_s pulse

Next, we perform time responses using the linearized longitudinal simulation model that includes actuator dynamics and the full 6DOF nonlinear model with deflection and deflection rate limits. The nonlinear simulation includes both the lateral and longitudinal controllers. Figure 2.8 shows the longitudinal linearized (dashed line) and the nonlinear (solid line) responses to a 1 g cstar step. Normal acceleration and pitch rate are shown for $0 \leq t \leq 10$ sec whereas normalized cstar is shown for $0 \leq t \leq 3$ sec. This is because the normalized cstar envelope is shown in Ref.[33] only for $0 \leq t \leq 3$ sec.

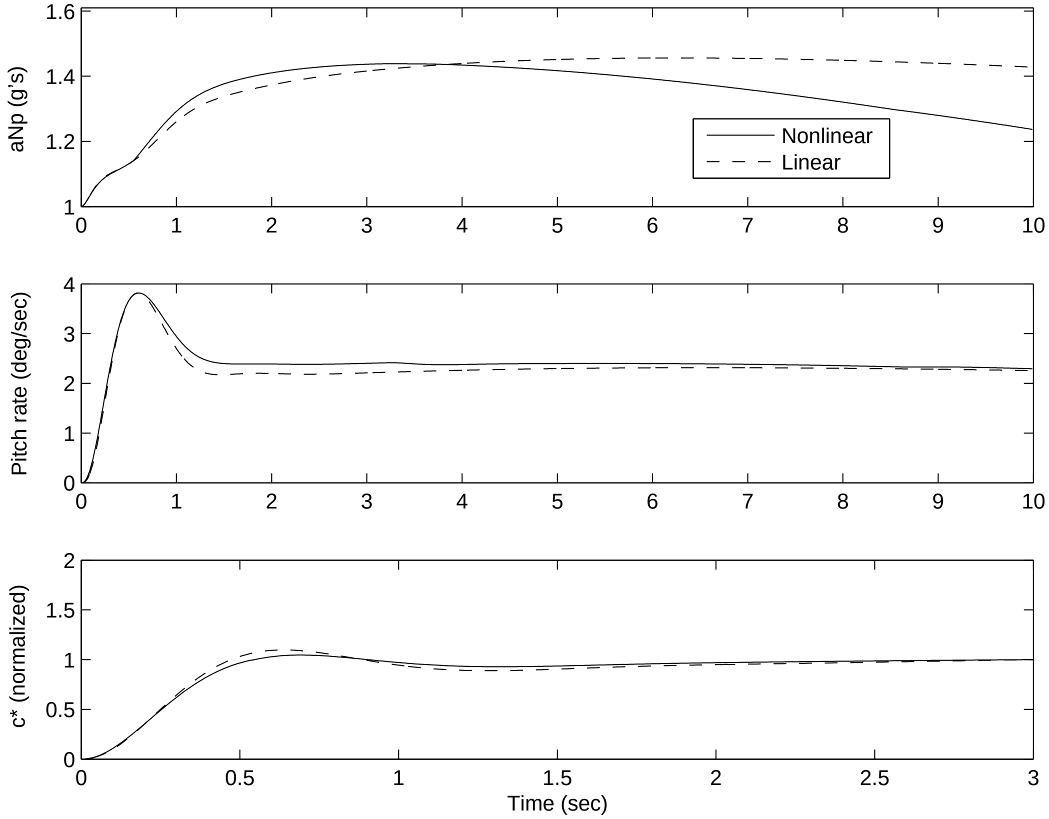

Figure 2.8: Nonlinear time responses to a 1 g cstar step

We observe that (1) the normalized cstar response is within the category I flight envelope of Ref.[33], and (2) the linear and nonlinear responses are similar until approximately 5 seconds when the nonlinear normal acceleration tends to its one g equilibrium value.

Figure 2.9 shows the control effector deflections. The maximum pitch flap and pitch thrust vector deflections are 4.5 deg and 2.2 deg, respectively for a maximum of 1.4 g normal acceleration. These deflections are well below the maximum deflections and will allow for much larger values of normal acceleration.

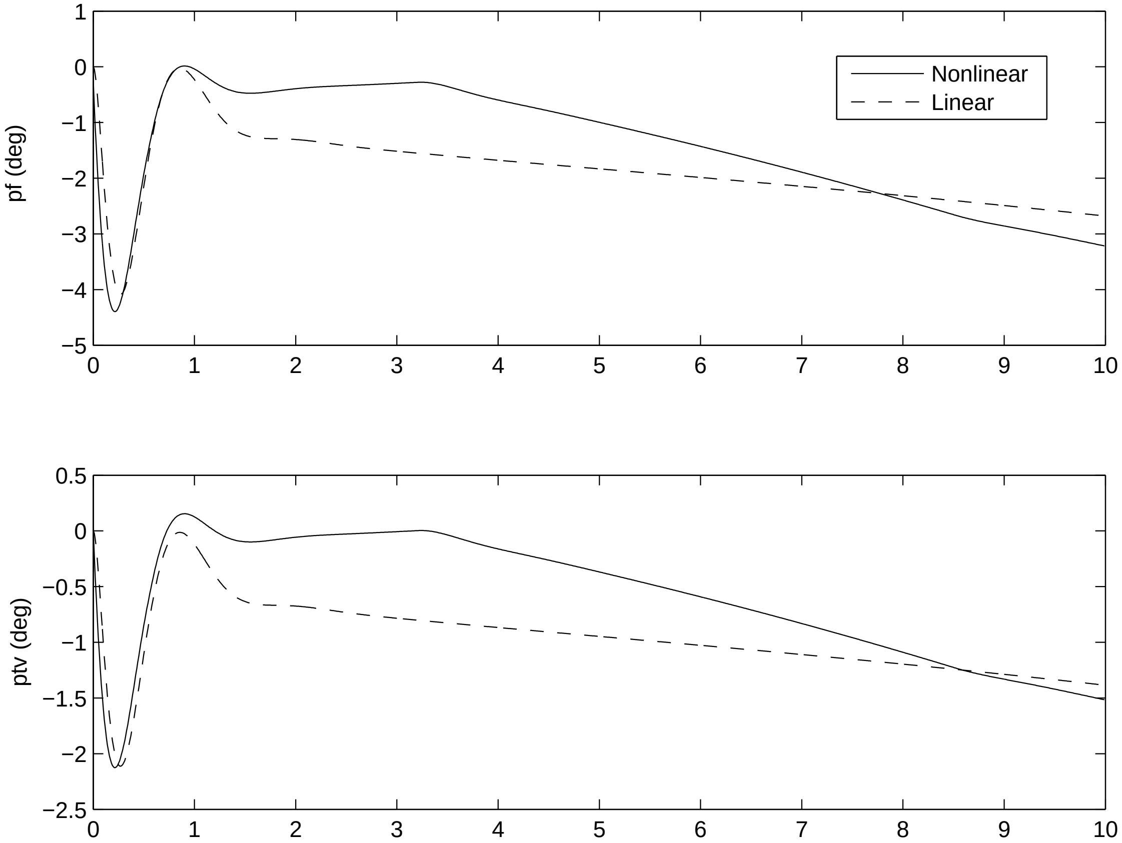

Figure 2.9: Nonlinear control responses to a 1 g cstar step

Chapter 3

Reconfigurable Control System

3.1 Overview

In this chapter, we extend the ICE aircraft's continuous-time flight control system design to the unified delta operator model that is valid for both continuous time and sampled data operation. We propose a new result that extends disk gain and phase margins to the delta operator system. Then, we consider symmetric lock in place failures of either the elevons or the all moving tips. We study the effect of the sampling period on the dutch roll damping, natural frequency, and phase margins to explain our choice of 25 samples/sec. We propose a novel eigenstructure assignment reconfiguration in which we first switch to a new recomputed gain to achieve satisfactory time responses. Then, we perform an optimization to achieve specifications on the disk gain and phase margins. We then switch to a second set of gains when the optimization achieves a feasible solution. This requires much less time than waiting for convergence to the optimal solution. We present simulation results using a full 6DOF nonlinear simulation. Our results show that an all moving tip failure causes the aircraft to become unstable whereas our eigenstructure assignment reconfigured flight control system yields responses that are similar to the unfailed responses. We also show that an elevon failure requires the feasible solution from an optimization to satisfy the disk gain and phase margin specifications in all channels.

3.2 Problem Statement

Consider the continuous-time linearized lateral dynamics of the ICE aircraft (section 2.2) described by

$$\begin{aligned} \dot{x}(t) &= Ax(t) + Bu(t) && (3.1) \\ y(t) &= Cx(t) && (3.2) \end{aligned}$$

where

$$x(t) = [\ \beta, \quad \phi, \quad p, \quad r\ ]^T \tag{3.3}$$

is the lateral state vector,

$$u(t) = [\ \delta_{el}, \quad \delta_{er}, \quad \delta_{amtl}, \quad \delta_{amtr}, \quad \delta_{ytv}\ ]^T = -Fy(t) \tag{3.4}$$

is the control vector with feedback gain matrix F such that stability, desired performance and satisfactory robustness of the flight control system are attained, and

$$y(t) = [\ \beta, \quad p_s, \quad (r_s)_{wo}\ ]^T \tag{3.5}$$

is the lateral output feedback vector.

A failure is modeled by setting the columns of the control derivative matrix corresponding to the stuck actuators to zero. We assume that there is a Fault Detection and Isolation(FDI) system which provides the linear fault model to be used for reconfiguration within 0.25sec.

The objective of our reconfigurable control system is to find a new feedback gain matrix such that all remaining (non faulty) control effectors are used to regain/maintain aircraft stability, to attain desired performance and to provide acceptable robustness of the flight control system.

3.3 Mathematical Results

Delta operator eigenstructure assignment assigns the eigenvalues in the $\gamma - plane$. We derive an expression for complex $\gamma - plane$ eigenvalues in terms of damping ratio ζ and natural frequency ω_n. We remark that ζ and ω_n are the same in both the s-plane and $\gamma - plane$. However, the s-plane eigenvalues and $\gamma - plane$ eigenvalues are different functions of ζ and ω_n.

Theorem 3.1 (Gamma eigenvalue as a function of damping and natural frequency): Given the damping ratio ζ and natural frequency ω_n where $\omega_n \leq \frac{\pi}{\Delta}$. The gamma plane eigenvalue γ is given by

$$\gamma = \frac{(e^{-\zeta\omega_n\Delta}cos(\omega_n\sqrt{1-\zeta^2}\Delta) - 1) + je^{-\zeta\omega_n\Delta}sin(\omega_n\sqrt{1-\zeta^2}\Delta)}{\Delta} \tag{3.6}$$

Proof: see Appendix A

The physical failure in an aircraft control effector occurs in continuous time body axis. However, in our gain computation we (1) transform to a stability axis model, (2) apply the control effector failure, (3) transform to the delta operator model, and (4) compute the eigenstructure assignment gain. The following result shows that this is equivalent to applying the failure in the continuous time body axis model.

Theorem 3.2 (Control effector failure equivalence): Let the continuous time aircraft in body axis have a failure in the j-th control input described by $w(b_j)^{body}$ where $(b_j)^{body}$ is the j-th column of B^{body} and $w \in [0, 1]$. Then, (1) the failure for the continuous time stability axis model is given by $w(b_j)^{stab}$ where $(b_j)^{stab}$is the j-th column of B^{stab}, and (2) the failure for the delta operator stability axis model is given by $wb_{\delta j}^{stab}$ where $b_{\delta j}^{stab}$is the j-th column of $(B_\delta)^{stab}$.

Proof: see Appendix B

Disk gain and phase margins are computed using function loopmargin in the MATLAB® Robust Control Toolbox [39]. This function uses the balanced sensitivity function S-T which yields margins that are symmetric on a log scale. The use of the balanced sensitivity function was originally proposed by Barrett [40] who used a bilateral transformation. These disk stability margins were applied to flight control design by Blight et. al. [41] An alternate derivation using the small gain theorem was later proposed by Bates and Postlethwaite [42]. We propose an extension of the disk stability margins to delta operator systems. Our proof uses ideas from the continuous time case in Ref.[43].

Theorem 3.3 (SISO Delta Operator Disk Gain and Phase Margins): Consider a SISO negative feedback delta operator system with sensitivity function $S(\gamma)$ and complementary sensitivity function $T(\gamma)$. Then, the disk gain and phase margins are given by

$$GM = \left[\frac{1 - r_{min}}{1 + r_{min}}, \frac{1 + r_{min}}{1 - r_{min}}\right] \tag{3.7}$$

and

$$PM = \pm 2tan^{-1} r_{min} \tag{3.8}$$

where

$$r_{min} = \frac{1}{\max\limits_{\omega \in [\frac{-\pi}{\Delta}, \frac{\pi}{\Delta}]} \left| S(\frac{e^{j\omega\Delta} - 1}{\Delta}) - T(\frac{e^{j\omega\Delta} - 1}{\Delta}) \right|} \tag{3.9}$$

Proof: see Appendix C

3.4 Delta Eigenstructure Assignment Reconfiguration

We follow the same procedure as in chapter 2 to obtain the flight control system for the ICE aircraft. However, now we apply eigenstructure assignment to the delta operator models of the linearized lateral and longitudinal ICE aircraft dynamics. The states, inputs and feedback variables of the lateral and longitudinal delta operator models are the same as in chapter 2.

Lateral Flight Control System

Recall that the states of the linearized body-axis lateral dynamics are β, ϕ, p and r. Upon transformation to stability axis and augmentation, the states become β, ϕ, p_s, r_s and a washout filter state x_{wo}. The lateral feedbacks are β, p_s, and washed out stability axis yaw rate$(r_s)_{wo}$ which allows us to assign three eigenvalues. The desired dutch roll damping ratio ζ, natural frequency ω_n and roll subsidence eigenvalue are $\zeta = 0.707$, $\omega_n = 3$, and λ_{roll}=-4. We use a weighted pseudo control distribution matrix whose columns correspond to rolling moment and yawing moment. The weights are w=[1,1,1,1,0.25].

We recompute the eigenstructure assignment gain when a failure occurs by projecting the desired eigenvectors[44] onto the failed achievable subspace. This is different from the approach in Refs. [13] - [15] where the authors project the unfailed achievable eigenvectors onto the failed achievable subspace. We choose to seek to attain desired performance when a failure occurs whereas Refs. [13] - [15] seek to attain unfailed performance. In any event, our experience indicates that both methods yield approximately equal feedback gains. The feedback gains for the two methods for both an all moving tips failure and an elevon failure are shown in Table 3.1. We observe that the feedback gains are approximately equal for both approaches. We remark that Table 3.1 uses the continuous time dynamics.

Table 3.1: Comparison of Gains for Different Projection Methods[a]

	orthogonal projection of ${v_i}^d$				projection onto unfailed ${v_i}^a$			
	β	P_s	$(r_s)_{wo}$		β	P_s	$(r_s)_{wo}$	
amt fail	-1.0883	0.3892	0.0237	$elev_L$	-1.0883	0.3892	0.0237	$elev_L$
	1 0883	-0.3892	-0.0237	$elev_R$	1.0883	-0.3892	-0.0237	$elev_R$
	0	0	0	amt_L	0	0	0	amt_L
	0	0	0	amt_R	0	0	0	amt_R
	11.0908	-0.3736	-3.1117	yaw_{TV}	11.0908	-0.3727	-3.1117	yaw_{TV}
elev fail	0	0	0	$elev_L$	0	0	0	$elev_L$
	0	0	0	$elev_R$	0	0	0	$elev_R$
	-1.3617	0.4869	0.0297	amt_L	-1.3616	0.4869	0.0297	amt_L
	1.3617	-0.4869	-0.0297	amt_R	1.3616	-0.4869	-0.0297	amt_R
	11.8203	-0.6421	-3.1225	yaw_{TV}	11.8202	-0.6397	-3.1224	yaw_{TV}

[a] Continuous time, $\zeta = 0.707$, $\omega_n = 3r/s$, $\lambda_{roll} = -4$

Next, we calculate the eigenstructure assignment gain for the delta operator model of the ICE aircraft lateral dynamics. The steps in our MATLAB® program are as follows: (1) begin with the body axis model,(2) transform to the stability axis model, (3)apply the control effector failure, (4) discretize to the delta operator model, (5) add the delta operator yaw rate washout filter, (6) apply the pseudo control weights, and (7) apply the pseudo control distribution matrix. Then, we compute the eigenstructure assignment gain. The washout filter in the s-plane has transfer function $\frac{s}{s+1}$ whereas its transfer function in the $\gamma - plane$ is $\frac{\gamma}{\gamma+0.98}$.

Sampling Period Effect on Dutch Roll Damping, Natural Frequency, and Phase Margins:

We analyze the stability robustness of the design using open loop phase and gain margins. We use the linearized simulation model that includes actuator dynamics. We modify function loopmargin from the MATLAB Robust Control Toolbox [39] to compute the delta operator disk margins. The disk margins represent the largest region for each channel such that the closed loop system is stable for all gain and phase variations inside the region. The disk margin analysis allows for simultaneous gain and phase variations one loop at a time. The unstable open loop complex mode poses a problem for gain and phase margin calculation. For a conventional aircraft with a real unstable spiral mode we would use a similarity transformation to decouple the spiral mode. Then, we would obtain gain and phase margins for the reduced order model that does not include the spiral mode. Unfortunately, the best that can be done here is to remove the bank angle equation from the open loop aircraft. This results in closed loop eigenvalues that are approximately the same for the model with the bank angle equation except for the absence of the spiral mode. We believe that this is acceptable especially because we use disk margins for simultaneous gain and phase variation whereas MIL-F-9490D [35] specifies either gain or phase variation. Thus, our analysis is conservative with respect to the specifications.

Table 3.2 shows the disk gain margin that does not achieve the specification as a function of the sampling period when no failure occurs. We observe that the disk phase and gain margins are satisfied in continuous time. However, the disk phase margin in the sideslip loop is less than the specification of 45 deg for sampled data operation.

Table 3.2: Disk Phase Margin vs. samples/sec for no failure case[a]

	PM, GM spec. violation for $\zeta_{dr} = 0.707$, $(\omega_n)_{dr} = 3r/s$	optimal gain for PM, GM spec. satisfied
continuous time	all margins achieved	NA
50 $samples/sec$	$PM_\beta = 44.1346$ deg	$\omega_n = 2.9340$, $\zeta = 0.7337$
25 $samples/sec$	$PM_\beta = 43.2302$ deg	$\omega_n = 2.9336$, $\zeta = 0.7639$
20 $samples/sec$	$PM_\beta = 42.6633$ deg	$\omega_n = 2.5195$, $\zeta = 0.7721$
15 $samples/sec$	$PM_\beta = 41.5191$ deg	$\omega_n = 2.6896$, $\zeta = 0.8211$
10 $samples/sec$	$PM_\beta = 39.5305$ deg	$\omega_n = 2.3825$, $\zeta = 0.8620$

[a] optimal gains for min $\|PM - PM^d\|$, lower bound $\omega_n = 2r/s$, w= $(1, 1, 1, 1, 0.25)$, optimization initialized at $\omega_n = 3r/s$, $\zeta = 0.707$

Furthermore, the disk phase margin in the sideslip loop decreases as the sampling rate decreases. Table 3.2 also shows ζ_{dr} and $(\omega_n)_{dr}$ for an optimal solution that achieves specifications on disk gain and phase margins in all input and output channels. The optimization is performed using function *fmincon* from the Optimization Toolbox[45] for use with MATLAB®. The performance index is chosen to be

$$J = \|PM^{ns} - PM^{spec}\| + \|GM^{ns} - GM^{spec}\| \tag{3.10}$$

subject to the constraints given by

$$\begin{aligned} PM^s &\geq PM^{spec} \\ GM^s &\geq GM^{spec} \end{aligned} \tag{3.11}$$

where PM^s and PM^{ns} are vectors containing the disk phase margins that satisfy and do not satisfy the specifications of 45 deg, respectively; GM^s and GM^{ns} are vectors containing the disk gain margins that satisfy and do not satisfy the specifications of 6dB, respectively; PM^{spec} is a vector whose entries are all 45 deg, and GM^{spec} is a vector whose entries are all 6dB.

The optimization is initialized with $\zeta_{dr} = 0.707$, $(\omega_n)_{dr} = 3r/s$, and $\lambda_{roll} = -4$. The optimization parameters are ζ_{dr} and $(\omega_n)_{dr}$. The interval for ζ_{dr} is chosen to be $0.4 \leq \zeta_{dr} \leq 0.9$. The choice of the interval for $(\omega_n)_{dr}$ is influenced by a plot of the unassigned washout filter eigenvalue vs. $(\omega_n)_{dr}$ which is shown in Figure 3.1.

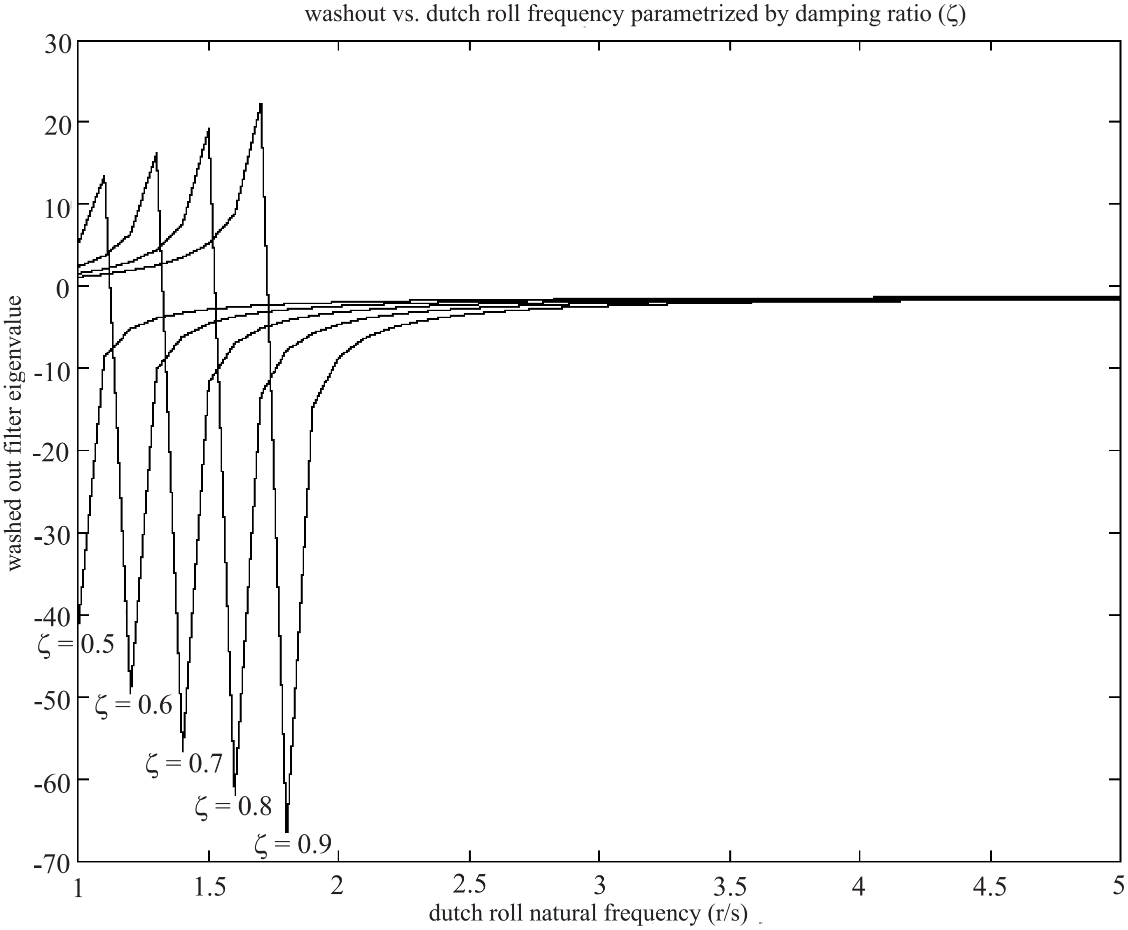

Figure 3.1: Washout filter eigenvalue vs. dutch roll natural frequency

We observe that the unassigned washout filter eigenvalue exhibits unacceptable values when $(\omega_n)_{dr} \leq 2r/s$. Therefore, we choose the lower end of the interval for $(\omega_n)_{dr}$ to be 2 r/s. Our interval for $(\omega_n)_{dr}$ is chosen to be $2r/s \leq (\omega_n)_{dr} \leq 5r/s$. We observe from the optimal solutions shown in Table 3.2 that $(\omega_n)_{dr} \approx 3r/s$ for sample rates at or faster than 25 samples/sec. This is one reason that we choose the sampling rate to be 25 samples/sec.

Table 3.3 shows the optimal solutions versus sampling rate for a 100% elevon failure. This corresponds to a lock in place failure. The first column in Table 3.3 shows the disk gain and phase margins that do not achieve the specifications when using the optimal solutions shown in Table 3.2. Thus, ζ_{dr} and $(\omega_n)_{dr}$ in column one of Table 3.3 are taken from column 2 of Table 3.2.

Table 3.3: Optimal and Feasible Solutions for 100% elevon failure

	PM, GM violation with optimal unfailed gain			Feasible solution[a]	
	$\omega_n\,(r/s)$	ζ	$PM_\beta\,(deg)$	$\omega_n\,(r/s)$	ζ
50 $samples/sec$	2.9340	0.7337	44.4019	2.4670	0.8169
25 $samples/sec$	2.9336	0.7639	42.9127	2.4691	0.8319
20 $samples/sec$	2.5195	0.7721	43.1740	2.0000	0.7646
15 $samples/sec$	2.6896	0.8211	40.8160	- No feasible solution -	
10 $samples/sec$	2.3825	0.8620	35.5277	- No feasible solution -	

[a] First feasible solution to achieve PM and GM specs, lower bound $\omega_n = 2r/s$, w= $(1, 1, 1, 1, 1)$, initialized with corresponding no failure ζ, ω_n

We observe that the disk phase margin in the sideslip channel does not achieve the specification when a 100% elevon failure occurs. The second column in Table 3.3 shows the first solution during the optimization when all disk gain and phase margins achieve the specifications. This solution is a feasible solution, but it may not be the optimal solution. We choose the first feasible solution because it requires significantly less computation time as compared with the computation time required to converge to the optimal solution. We observe that for the feasible solutions $\zeta_{dr} \approx 0.8$ and $(\omega_n)_{dr} \approx 2.5r/s$ for a sampling rate of 25 samples/sec. However, $(\omega_n)_{dr} = 2r/s$ for a sampling rate of 20 samples/sec. This places $(\omega_n)_{dr}$ at the boundary of the constraint set. Finally, the optimization does not converge for a sampling rate of 15 samples/sec or less. This is another reason that we choose the sampling rate to be 25 samples/sec.

Reconfigurable Delta Operator Eigenstructure Assignment for the ICE Aircraft Under Symmetric Failures in the Lateral Control Effectors:
We propose the following real time reconfiguration method : (1) recompute the eigenstructure assignment gains when a failure is detected, (2) switch the gains to the new values, (3) perform the optimization described by Eqs.(3.10)-(3.11), and (4) switch the gain values to the first feasible solution that achieves specifications on the disk gain and phase margins in all channels.

Table 3.4 shows the feedback gains, disk margins, and eigenvalues for the no failure case. The eigenstructure assignment gains that assign $\zeta_{dr} = 0.707$ and $(\omega_n)_{dr} = 3r/s$ does not achieve the disk phase margin in the sideslip channel. We remark that the $\gamma - plane$ roll mode eigenvalue γ_{roll}=-3.6964 corresponds to the s-plane eigenvalue λ_{roll}=-4. Next, we compute the optimal solution that minimizes Eqs.(3.10)-(3.11). We use the optimal solution here because the unfailed gains are computed off-line and stored in the flight control computer. We observe that the optimal gains achieve the disk gain and phase margin specifications in all channels. The dutch roll damping has changed from ζ_{dr}=0.707 to ζ_{dr}=0.7639. The dutch roll natural frequency has changed from $(\omega_n)_{dr}$=3r/s to $(\omega_n)_{dr}$=2.9336 r/s.These changes in ζ_{dr} and $(\omega_n)_{dr}$ are insignificant.

Table 3.4: No Failure Case: Feedback Gains, Gain/Phase Margins, and Eigenvalues[a]

	Feedback Gains				Margins				Eigenvalues		
										100%	100%
	β	P_s	$(r_s)_{wo}$		$GM\,(db)$	$PM\,(deg)$			No failure	elevon	amt
Eigenstructure	-10.0123	0.6058	2.6013	$elev_L$	±28.88	±85.88	elev	ζ_{dr}	0.707	-	-
assignment	10.0123	-0.6058	-2.6013	$elev_R$	±15.55	±71.05	amt	$(\omega_n)_{dr}$	3	-	-
$\zeta_{dr} = 0.707$	11.1323	-0.3078	-3.1998	amt_L	±16.96	±73.84	yaw_{TV}	γ_{roll}	-3.6964	-	-
$(\omega_n)_{dr} = 3r/s$	-11.1323	0.3078	3.1998	amt_R	±7.28	±43.23	β	γ_{wo}	-1.8426	-	-
	4.2926	-0.1777	-1.1843	yaw_{TV}	±17.76	±75.25	P_s	γ_{spiral}	0.0082	-	-
					±12.29	±62.68	$(r_s)_{wo}$				
Optimal gain	-10.4251	0.6090	2.7933	$elev_L$	±29.16	±86.01	elev	ζ_{dr}	0.7639	0.6513	-0.0951
	10.4251	-0.6090	-2.7933	$elev_R$	±15.64	±71.24	amt	$(\omega_n)_{dr}$	2.9336	4.1543	1.0424
	11.6402	-0.3117	-3.4415	amt_L	±16.93	±73.39	yaw_{TV}	γ_{roll}	-3.6964	-1.2354	-4.12
	-11.6402	0.3117	3.4415	amt_R	±7.656	±45.00	β	γ_{wo}	-2.0248	-1.9957	-1.6768
	4.4806	-0.1791	-1.2729	yaw_{TV}	±17.75	±75.24	P_s	γ_{spiral}	0.0082	0.0125	0.0238
					±11.80	±61.16	$(r_s)_{wo}$				

[a] Sampling rate is $25 samples/sec$, w= $(1, 1, 1, 1, 0.25)$

Longitudinal Flight Control System

Recall that the linearized longitudinal states are V_T, α, θ, q, and integral of cstar $\int c^*$. The feedbacks are c^*, q, and $\int c^*$. The block diagram of the longitudinal flight control system is shown in Figure 2.3. We are only considering symmetric failures in the lateral control effectors, therefore the longitudinal control system design follows the design procedure in chapter 2. The only difference is that now we apply eigenstructure assignment to the delta operator model of the linearized longitudinal ICE aircraft dynamics. Also, we replaced the integrator with continuous time transfer function $\frac{1}{s}$ with its delta operator equivalent of $\frac{1}{\gamma}$. and the pitch stick filter with continuous transfer function of $\frac{5(s+0.5)}{s+2}$ is replaced by its delta operator equivalent of

$\frac{5(\gamma+0.4805)}{\gamma+1.9221}$.

Table 3.5 compares the continuous time and delta operator eigenstructure assignment gains where the sampling rate is 25 samples/sec. We observe that there are significant differences between the two gain matrices. This indicates that the design should be done in the delta domain for a sampling rate of 25 samples/sec. Table 3.5 also shows the feedback gain matrix for 1000 samples/sec to show that the delta operator feedback gains approach the continuous time gains as the sampling period Δ goes to zero.

Table 3.5: Longitudinal feedback gains

	c*	α	q	$\int$c*				
continuous gain	-5.5885	-5.5885	-0.4979	8.320	δ_{pflap}	λ_{sp}	$=$	$-3 \pm j4$
	-2.8890	-2.8890	-0.2574	4.301	δ_{pTV}	λ_{ph}	$=$	$-0.0070 \pm j0.0071$
						λ_{int}	$=$	-0.25
delta gain	-4.9419	-4.9419	-0.6147	7.4320	δ_{pflap}	γ_{sp}	$=$	$-3.1102 \pm j3.5326$
25$samples/sec$	-2.5593	-2.5593	-0.3184	3.8489	δ_{pTV}	γ_{ph}	$=$	$-0.0062 \pm j0.0071$
						γ_{int}	$=$	-0.2488
delta gain	-5.5714	-5.5714	-0.5011	8.2966	δ_{pflap}	γ_{sp}	$=$	$-3.0035 \pm j3.9880$
1000$samples/sec$	-2.8803	-2.8803	-0.2591	4.2891	δ_{pTV}	γ_{ph}	$=$	$-0.0063 \pm j0.0071$
						γ_{int}	$=$	-0.25

3.5 Symmetric Lock in Place Failure Reconfiguration Results

Elevons Failure:

We observe from Table 3.4 that for a 100% elevon failure we have ζ_{dr}=0.6513, $(\omega_n)_{dr}$=4.1543, and γ_{roll}=-1.2354. This represents significant changes from the unfailed case. However, the aircraft still achieves MIL-F-8785C[34] specifications although the roll mode is close to the boundary of γ_{roll}=-0.9803 corresponding to λ_{roll}=-1.

Table 3.6 shows the feedback gains, disk margins, and eigenvalues for a 100% elevon failure. We have changed the pseudocontrol weights to w=[1,1,1,1,1] from the previous values of w=[1,1,1,1,0.25] because we want to allow increased yaw thrust vector deflection to compensate for the elevon failure. Furthermore, our experience indicates that the weights have no effect when a 100% failure occurs.

We first show the reconfigured gain computed using eigenstructure assignment. This new gain requires only 0.0630 seconds to compute. We compare this new gain with the unfailed optimal gain shown in Table 3.4. Of course, the assigned eigenvalues represented by ζ_{dr}, $(\omega_n)_{dr}$, and γ_{roll} are identical before and after reconfiguration. However, the disk phase margin of 42.93 deg in the yaw thrust vector channel is less than the specification of 45 deg. Next, we perform the optimization described by Eqs.(3.10)-(3.11). The first iteration where all disk gain and phase margins achieve the specifications is denoted by the feasible solution in Table 3.6. This second new gain required a computation time of 5.875 seconds. This is significantly less than the 39.6 seconds required to converge to the optimal solution.

Table 3.6: 100% elevon failure: Feedback Gains, Gain/Phase Margins, and Eigenvalues[a]

	Feedback Gains			Margins			Eigenvalues	
	β	P_s	$(r_s)_{wo}$		$GM\,(db)$	$PM\,(deg)$		
Eigenstructure	0	0	0	$elev_L$	±25.93	±84.21	amt	ζ_{dr} = 0.7639
Assignment	0	0	0	$elev_R$	±7.22	±42.93	yaw_{TV}	$(\omega_n)_{dr}$ = 2.9336
$\zeta_{dr} = 0.7639$	-1.4010	0.4500	0.0528	amt_L	±7.71	±45.24	β	γ_{roll} = -3.6964
$(\omega_n)_{dr} = 2.9336r/s$	1.4010	-0.4500	-0.0528	amt_R	±17.75	±75.24	P_s	γ_{wo} = -2.0069
(0.0630sec.	11.6583	-0.5979	-3.1840	yaw_{TV}	±11.92	±61.54	$(r_s)_{wo}$	γ_{spiral} = 0.0082
computation time)								
Feasible solution	0	0	0	$elev_L$	±26.10	±84.33	amt	ζ_{dr} = 0.8319
(5.812sec.	0	0	0	$elev_R$	±7.72	±45.30	yaw_{TV}	$(\omega_n)_{dr}$ = 2.4668
computation time)	-1.4772	0.4502	0.0682	amt_L	±8.24	±47.66	β	γ_{roll} = -3.6964
	1.4772	-0.4502	-0.0682	amt_R	±17.75	±75.24	P_s	γ_{wo} = -2.8837
	12.0083	-0.6019	-3.4946	yaw_{TV}	±11.45	±60.04	$(r_s)_{wo}$	γ_{spiral} = 0.0082

[a] Sampling rate is $25 samples/sec$, w= $(1, 1, 1, 1, 1)$

We observe from Table 3.6 that ζ_{dr} has changed from 0.7639 to 0.8319 and $(\omega_n)_{dr}$ has changed from 2.9336r/s to 2.4668 r/s. Our second gain satisfies both MIL-F-8785C[34] mode specifications and MIL-F9490D gain and phase margin specifications[35].

All Moving Tips Failure:

We observe from Table 3.4 that the aircraft exhibits an unstable dutch roll mode for a 100% amt failure. Therefore, the aircraft cannot continue flying after a 100% amt failure without a reconfiguration of the controller gains.

Table 3.7 shows the feedback gains, disk margins, and eigenvalues for a 100% amt failure. The reconfigured eigenstructure assignment gains stabilize the aircraft by achieving the unfailed dutch roll damping ζ_{dr}=0.7639, dutch roll natural frequency $(\omega_n)_{dr}$=2.9336r/s, and γ_{roll}=-3.6964.Furthermore, the disk gain and phase margins in all channels achieve the specifications of 45 deg and 6dB, respectively. So an optimization is not needed.

Table 3.7: 100% amt failure: Feedback Gains, Gain/Phase Margins, and Eigenvalues[a]

	Feedback Gains			Margins			Eigenvalues		
	β	P_s	$(r_s)_{wo}$		$GM\,(db)$	$PM\,(deg)$			
Eigenstructure	-1.1200	0.3598	0.0422	$elev_L$	±25.11	±83.65	elev	ζ_{dr}	= 0.7639
Assignment	1.1200	-0.3598	-0.0422	$elev_R$	±7.67	±45.08	yaw_{TV}	$(\omega_n)_{dr}$	= 2.9336
$\zeta_{dr} = 0.7639$	0	0	0	amt_L	±7.70	±45.20	β	γ_{roll}	= -3.6964
$(\omega_n)_{dr} = 2.9336 r/s$	0	0	0	amt_R	±17.75	±75.24	P_s	γ_{wo}	= -2.0137
$t_{comp} = 0.0630 sec$	10.9103	-0.3505	-3.1605	yaw_{TV}	±11.90	±61.48	$(r_s)_{wo}$	γ_{spiral}	= 0.0082

[a] Sampling rate is 25$samples/sec$, w= $(1, 1, 1, 1, 1)$

Nonlinear Simulation Results:

We perform time responses using the full 6DOF nonlinear model with deflection and deflection rate limits. The nonlinear simulation includes both the lateral and longitudinal controllers. The computation times for the new eigenstructure assignment gain K_{eig} and the feasible gain K_{feas} to achieve gain and phase margins specifications are 0.063 sec and 5.812 sec, respectively. We assume a failure detection time of 0.25 sec. Thus, we begin the computation of the new K_{eig} at 0.25 sec after a failure occurs. In all our simulations, we used the following sequence: (1) a failure occurs at t=1 sec, (2) computation of the new K_{eig} begins at t=1.25 sec, (3) we switch to the new K_{eig} at t=1.313 sec, (4) we begin computation of K_{feas} at t=1.313 sec, and (5) we switch to K_{feas} at t=7.125 sec. However, we know from Table 3.7 that an amt failure does not require K_{feas}. So in this case we omit steps 4 and 5.

First, we consider a pilot roll command p_c described by

$$p_c = \begin{cases} 0 deg/sec & ; 0 \leq t < 2 \\ 1 deg/sec & ; 2 \leq t < 6 \\ 0 deg/sec & ; 6 \leq t < 10 \\ -1 deg/sec & ; 10 \leq t < 14 \\ 0 deg/sec & ; 14 \leq t < 20 \end{cases} \tag{3.12}$$

Figure 3.2 shows the lateral responses for a symmetric stuck in place amt failure. These responses are sideslip angle β, bank angle ϕ, stability axis roll rate p_s, and stability axis yaw rate r_s. Both the failure and the switch to the new K_{eig} occur before the pilot command is applied. We observe that the aircraft without reconfiguration exhibits an unstable oscillation. However, the unfailed and reconfigured responses are approximately the same.

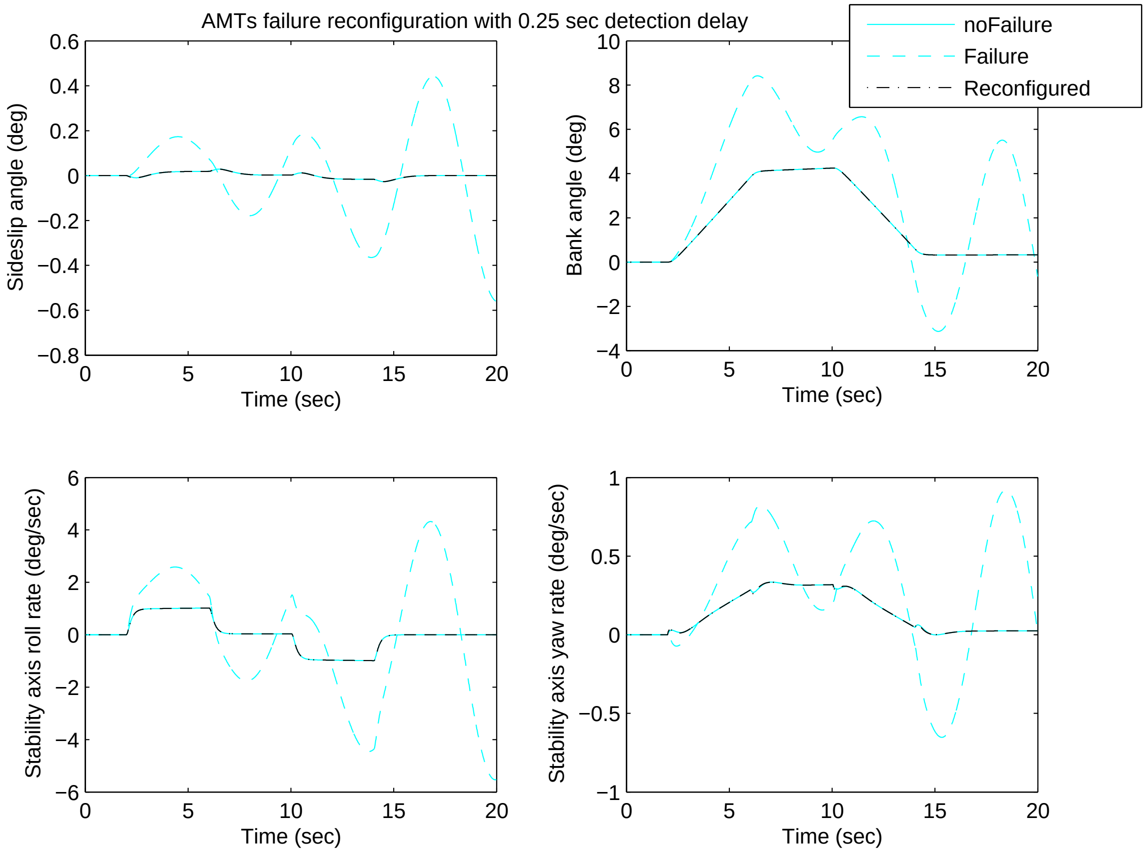

Figure 3.2: All moving tips failure before roll rate command (states)

Figure 3.3 shows the lateral responses for a symmetric lock in place elevon failure. We observe that the bank angle without reconfiguration is less than half of its unfailed value. In addition, we observe oscillations in yaw rate. Again the unfailed and reconfigured responses are approximately the same.

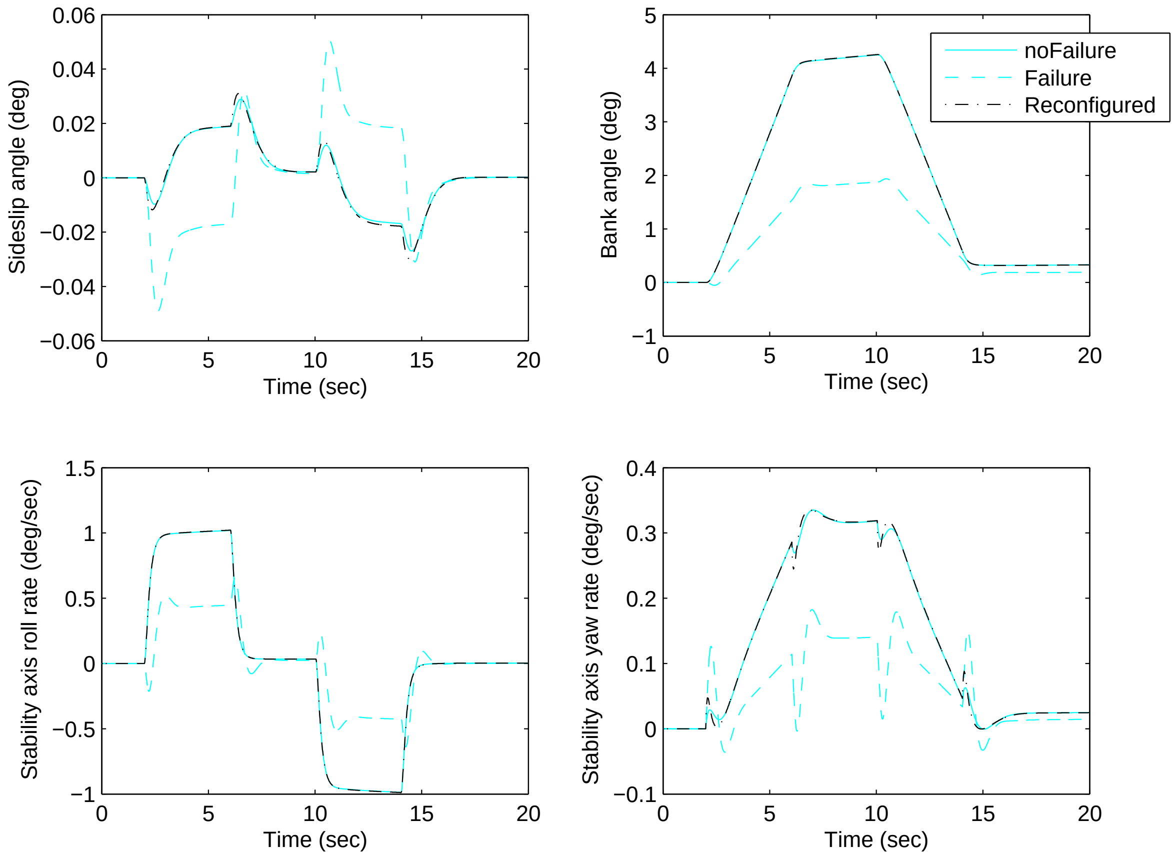

Elevons failure reconfiguration with 0.25 sec detection delay

Figure 3.3: Elevon failure before roll rate command (states)

Next, we consider a lateral velocity wind gust of 15 ft/sec for $2 \leq t < 2.5sec$. Figure 3.4 shows the lateral responses for a symmetric lock in place amt failure. We observe that the aircraft without reconfiguration exhibits an unstable oscillation. The unfailed and reconfigured responses are similar.

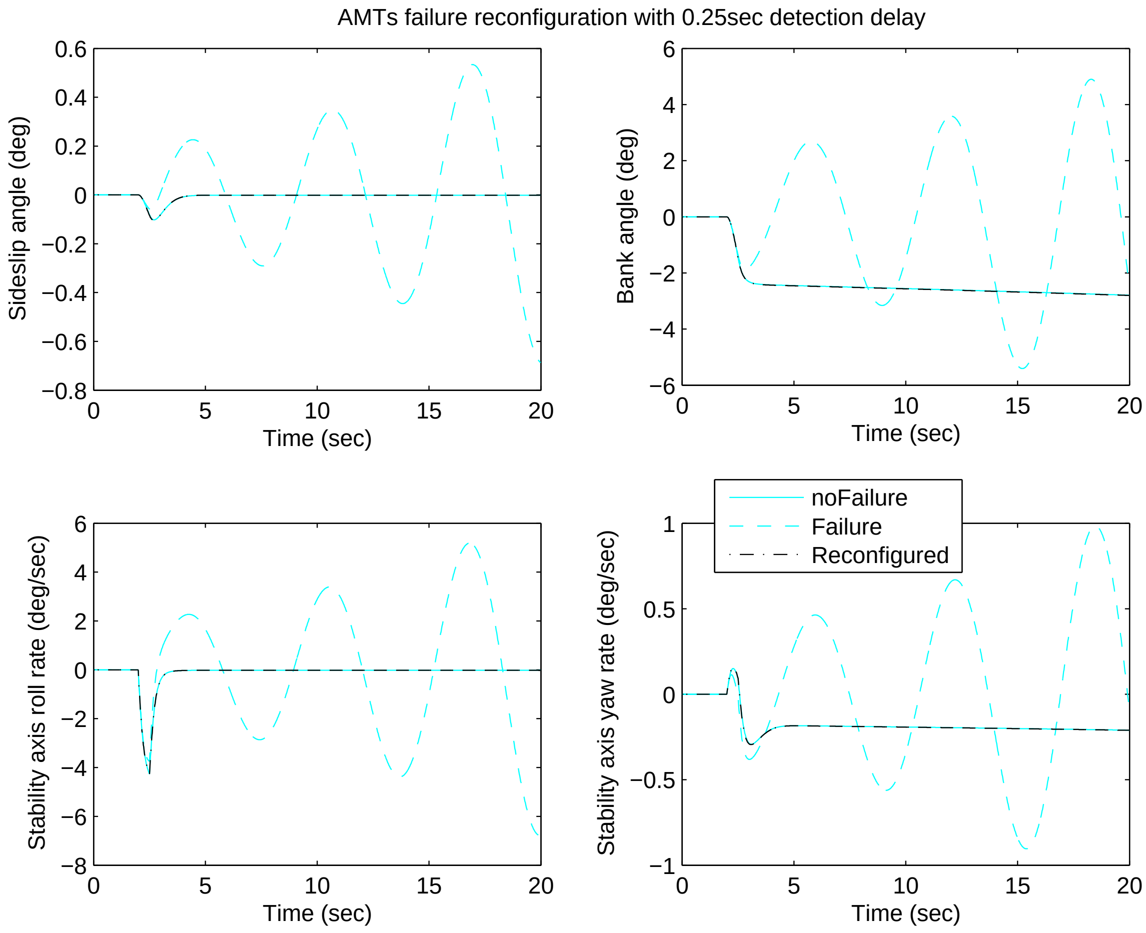

Figure 3.4: All moving tips failure before lateral gust (states)

Figure 3.5 shows the lateral responses for a symmetric elevon failure. We observe that without reconfiguration, the roll rate and sideslip angle have increased. Again the unfailed and reconfigured responses are similar. We remark that the bank angle does not return to zero because we are using a stability augmentation system without an autopilot mode.

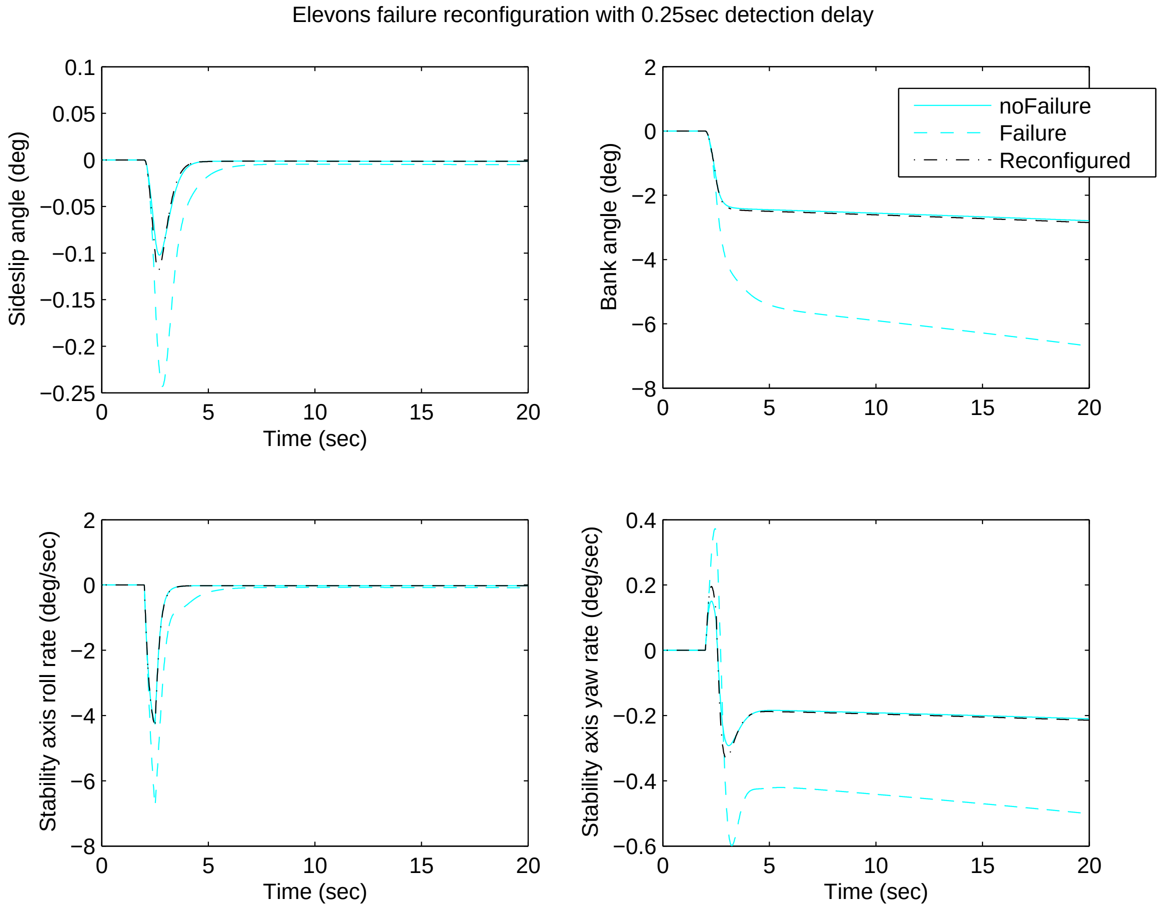

Figure 3.5: Elevon failure before lateral gust (states)

Finally, we consider a pilot roll rate command of 1deg/sec for 0$\leq$ t $<$ 2sec. Now the failure at t=1 sec occurs during the pilot command. Figure 3.6 shows the lateral responses for a symmetric amt lock in place failure. We observe the unstable oscillatory responses that occur without reconfiguration. The unfailed and reconfigured responses are similar except for an initial difference. This difference is the result of the 0.25 sec detection time and the 0.063 sec computation time.

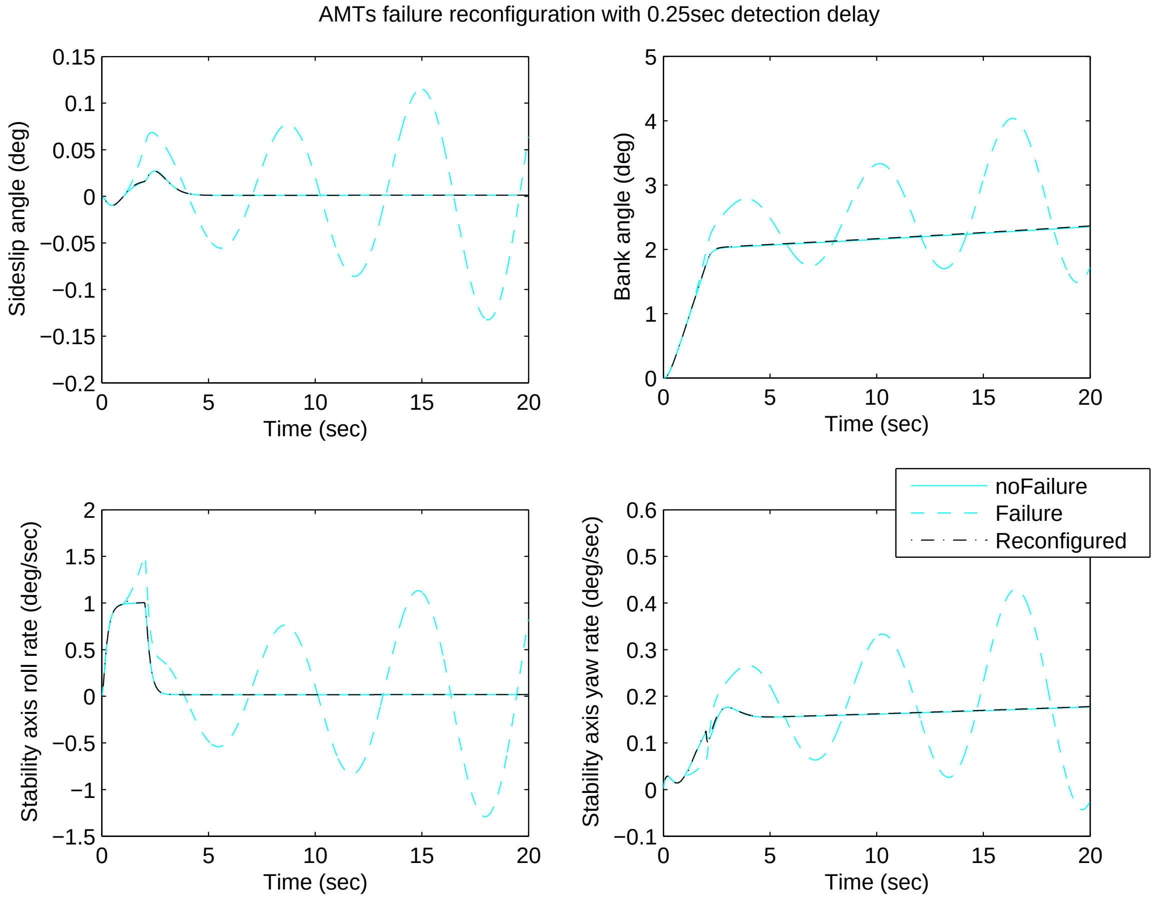
AMTs failure reconfiguration with 0.25sec detection delay

Figure 3.6: All moving tips failure during roll rate command (states)

Figure 3.7 shows the control effector deflections. We observe that after one second the amts are locked in place at their failure time values.

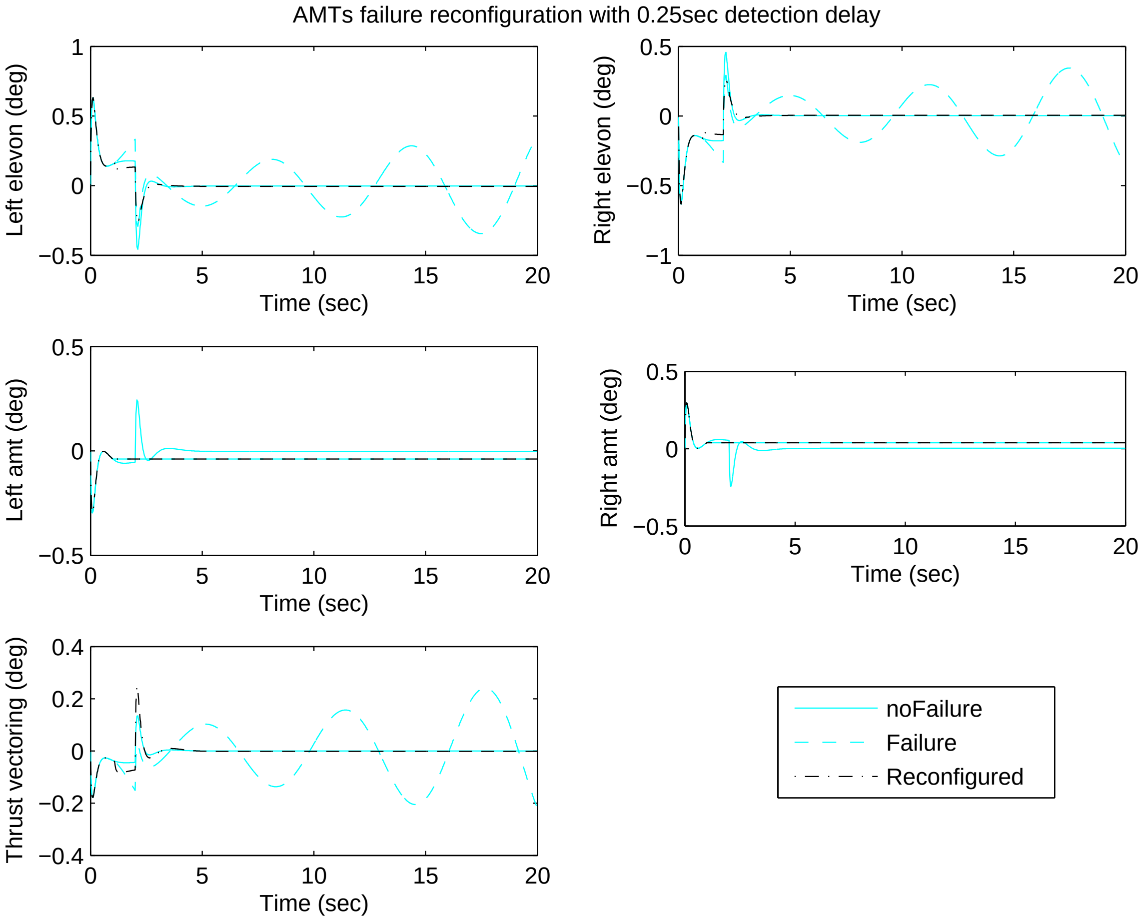

Figure 3.7: All moving tips failure during roll rate command (controls)

Figure 3.8 shows pitch rate q, angle of attack α, speed V_T, and altitude h. We observe that the aircraft remains approximately at its trim flight of $h = 15,000 ft$ and $V_T = 423 ft/sec$ after the failure.

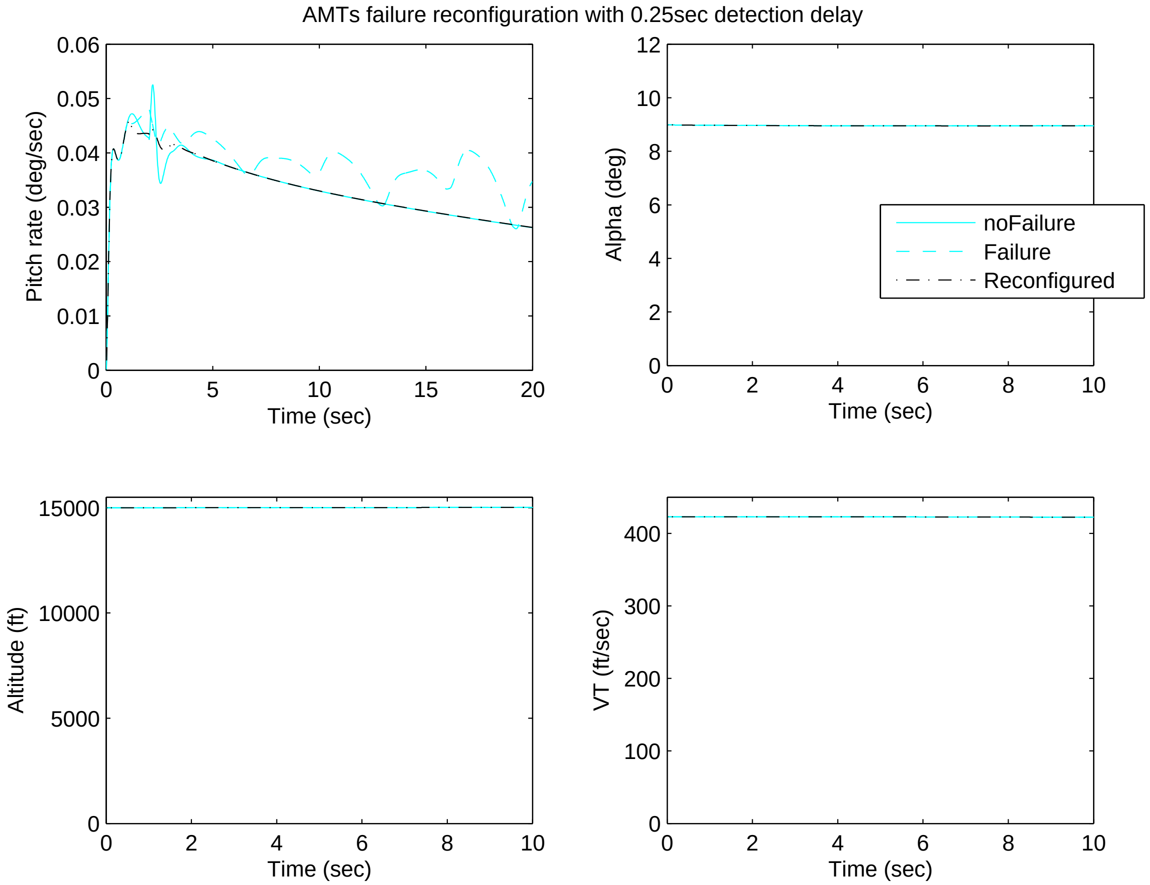

Figure 3.8: All moving tips failure during roll rate command (speed, altitude, alpha)

Figure 3.9 shows the lateral responses for a symmetric lock in place elevon failure. We again observe an initial difference between the unfailed and reconfigured responses due to the detection and gain computation times.

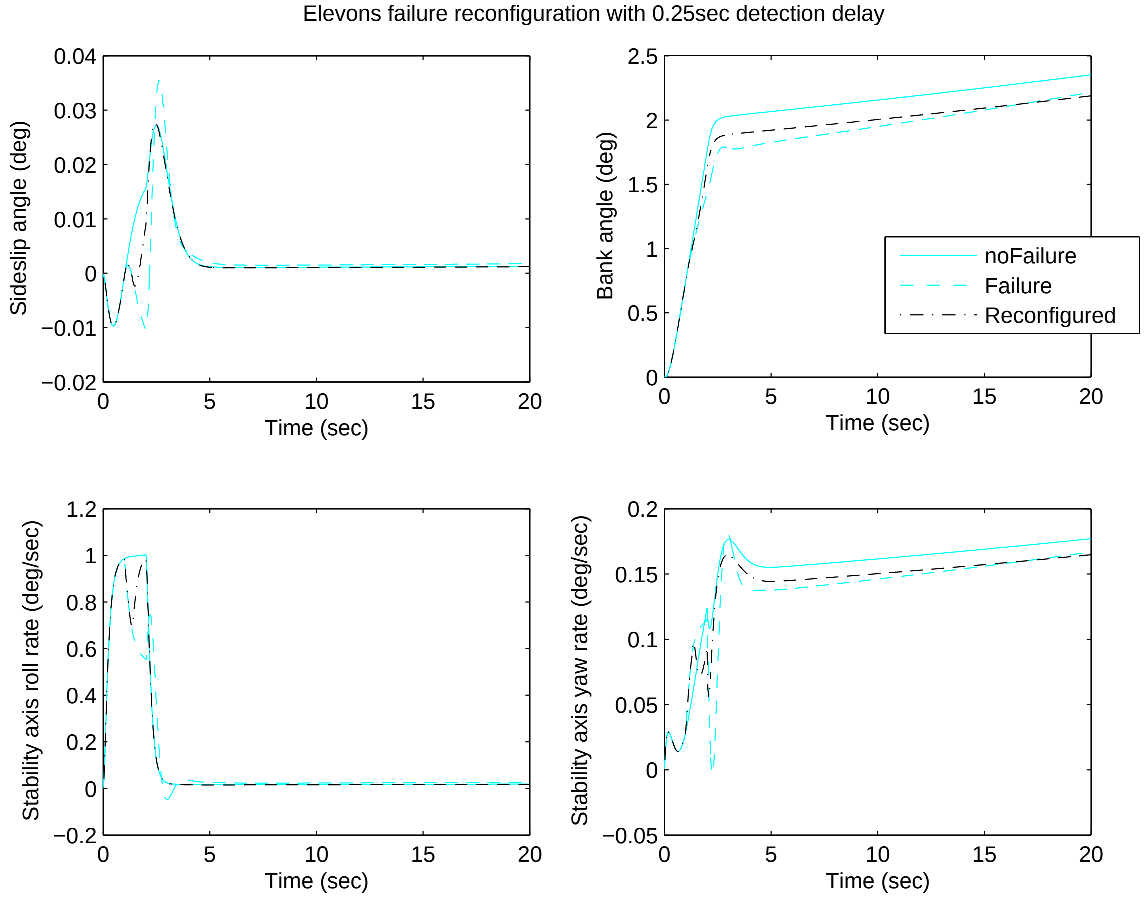

Figure 3.9: Elevon failure during roll rate command (states)

Chapter 4

Fault Detection and Isolation

4.1 Overview

In this section, we extend multiple and simultaneous fault detection and isolation (FDI) system design by a single diagnostic observer to the unified delta operator model that is valid for both continuous time and sampled data operation. We reformulate the detection filter problem and detectability conditions for delta operator systems. We use an eigenstructure framework to extend fixed directional residuals to delta operator systems and establish the conditions for allowable failures for the delta operator model. We present a new mathematical result that reveals the independence of the projection matrix W from the observer's eigenvectors for the delta operator model. Then, we present the projection matrix for the delta operator model. We extend a result proven by Moore [21] for computing the observer gains for the delta operator model. We present a new result for the delta operator model fault free residual bound, and use it to propose a new eigenvector selection criterion for robust FDI, subject to unstructured uncertainty and known initial condition mismatches. Then, we propose a new method/algorithm for multiple and simultaneous FDI of actuator failures for delta operator systems which involves a coordinate transformation of the system, the construction of subspaces to satisfy FDI conditions, and an eigenvector selection criterion for FDI robustness that is determined by the unconstrained optimization of a three-term weighted performance index. Finally, we consider the linearized longitudinal dynamics of a VTOL aircraft in the vertical plane, to demonstrate our FDI algorithm for delta operator systems. We subject the aircraft to an initial condition mismatch in the vertical velocity state and bias failures in the actuators of the collective control and the longitudinal cyclic control. We show that FDI system design by fixed directional residuals that use eigenstructure-based optimizations result in different sets of eigenvectors. Thus, residual responses can vary significantly. In contrast, our optimization and simulation results show that our FDI algorithm yields different sets of eigenvectors that (1) minimize the performance index, (2) satisfy FDI design requirements, (3) have low condition number, and (4) result in excellent and tightly similar residual responses with a detection time of approximately 4ms for 1ms sampled data rate.

4.2 Problem Statement

Consider an aircraft subject to failures of the control actuators described by the following continuous time linear time-invariant model:

$$\dot{x}(t) = Gx(t) + Hu(t) + Kf(t), \tag{4.1}$$

$$y(t) = Cx(t), \tag{4.2}$$

where $x(t) \in \mathrm{R}^n$ is the state vector, $u(t) \in \mathrm{R}^m$ is the control input vector, $y(t) \in \mathrm{R}^r$ is the output vector, and G, H, C are real matrices of compatible dimensions. The pair (C, G) is assumed to be observable. The effect of actuator faults is modeled by the $Kf(t)$ term, where K is known as the failure signature, and $f(t)$ is a vector containing the failure modes which are described by arbitrary functions which may be functions of $x(t)$ or $u(t)$. K is assumed to have full column rank, since the failure modes $f_i(t), i = 1, \dots m$ are arbitrary [46]. Multiple actuator faults are modeled by letting $K = H$ and by zeroing the components of $f(t)$ that correspond to non-faulty actuators. A priori knowledge of $f(t)$ is not required in the design process of a detection filter [20], and hence, the failure signature $K = H$ can model the effect of a wide variety of actuator failures (dead actuator, bias failure,...), since the failure mode is not restricted in any way [46].

The unified delta operator model with multiple faults in the actuators, that is valid for both continuous time and sampled data operation, is obtained by using Middleton and Goodwin's [17] delta operator and is given by

$$\rho x(t) = G_\rho x(t) + H_\rho u(t) + K_\rho f(t), \tag{4.3}$$

$$y(t) = Cx(t), \tag{4.4}$$

where

$$\rho = \begin{cases} \frac{d}{dt}, & \text{in continuous time} \\ \delta, & \text{in discrete time} \end{cases} \tag{4.5}$$

$$G_\rho = \begin{cases} G, & \text{in continuous time} \\ G_\delta = \Omega G, & \text{in discrete time} \end{cases} \tag{4.6}$$

$$H_\rho = \begin{cases} H, & \text{in continuous time} \\ H_\delta = \Omega H, & \text{in discrete time} \end{cases} \tag{4.7}$$

$$K_\rho = \begin{cases} K, & \text{in continuous time} \\ K_\delta = \Omega K, & \text{in discrete time} \end{cases} \tag{4.8}$$

and where

$$\Omega = \frac{1}{\Delta}\int_0^{\Delta} e^{G\tau} d\tau \tag{4.9}$$

$$\delta = \frac{q-1}{\Delta} \tag{4.10}$$

and where the shift operator q is defined by

$$q x_k = x_{k+1} \tag{4.11}$$

and where Δ is the sampling period.

$$\mathbf{E}_{L\rho}\left(\Lambda, t\right) = \begin{cases} e^{\Lambda t} & \text{in continuous time} \\ \left(I + \Lambda\Delta\right)^{t/\Delta} & \text{in discrete time} \end{cases} \tag{4.12}$$

$$\overset{t_2}{\underset{t_1}{\mathbf{S}}} f(\tau) d\tau = \begin{cases} \int\limits_{\tau=t_1}^{\tau=t_2} f(\tau) d\tau & \text{in continuous time} \\ \Delta \sum\limits_{k=t_1/\Delta}^{k=(t_2/\Delta)-1} f(k\Delta) & \text{in discrete time} \end{cases} \tag{4.13}$$

$$\gamma_i = \begin{cases} \lambda_i & \text{in continuous time} \\ \frac{e^{\lambda_i \Delta} - 1}{\Delta} & \text{in discrete time} \end{cases} \tag{4.14}$$

and

$$\Lambda = diag\left(\gamma_i\right), \quad i = 1, \ldots, n \tag{4.15}$$

Now consider a common observer-based residual generator where the plant is subjected only to actuator failures $f(t)$ as shown in Figure 4.1. The residual generator uses an observer to generate estimates of the system states and measurements. Then, residual signals that are suitable for multiple fault detection and isolation are generated. The difference between actual and estimated measurements is projected onto specific directions by a constant projection matrix W_ρ.

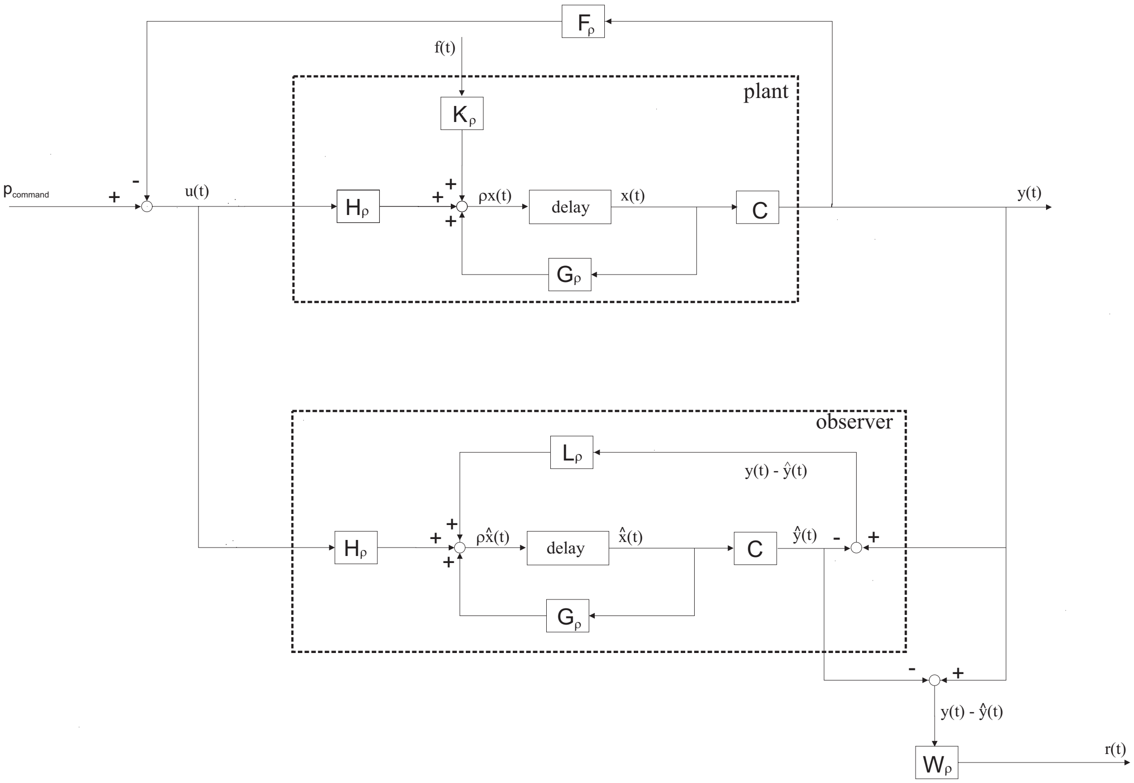

Figure 4.1: Observer-based residual generator.

The observer dynamics are given by

$$\rho\hat{x}(t) = (G_\rho - L_\rho C)\hat{x}(t) + H_\rho u(t) + L_\rho y(t), \tag{4.16}$$

$$\hat{y}(t) = C\hat{x}(t), \tag{4.17}$$

$$r(t) = W_\rho[y(t) - \hat{y}(t)], \tag{4.18}$$

where $\hat{x}(t) \in \mathrm{R}^n$ is the state estimation vector, $\hat{y}(t) \in \mathrm{R}^r$ is the output estimation vector, $r(t)$ is the residual vector for fault monitoring, $L_\rho(t) \in \mathrm{R}^{n\times r}$ is the observer feedback gain matrix, and $W_\rho(t) \in \mathrm{R}^{p\times r}$ is a constant projection matrix.

The state estimation error is defined by

$$e(t) = x(t) - \hat{x}(t), \tag{4.19}$$

thus, the state error dynamics are given by

$$\rho e(t) = G_{L\rho} e(t) + K_\rho f(t), \tag{4.20}$$

and assuming that $e(0) = 0$, the residual vector in Eq. (4.18) can be expressed as

$$r(t) = W_\rho C e(t), \tag{4.21}$$

where

$$G_{L\rho} = G_\rho - L_\rho C. \tag{4.22}$$

The complete γ-domain response of the residual to the fault is given by

$$r(\gamma) = G_{rf}(\gamma) f(\gamma), \tag{4.23}$$

where

$$G_{rf}(\gamma) = W_\rho C(\gamma I - G_{L\rho})^{-1} K_\rho. \tag{4.24}$$

Therefore, the detectability conditions for delta operator systems are:

1. The i^{th} fault is said to be detectable if the i^{th} column $[G_{rf}(\gamma)]_i$ of the transfer function matrix between residual and fault $G_{rf}(\gamma)$ is not zero, especially for steady-state values:

$$[G_{rf}(\gamma)]_i \neq 0, \quad \text{and} \quad [G_{rf}(0)]_i \neq 0. \tag{4.25}$$

2. Multiple faults can be isolated if the transfer function matrix $G_{rf}(\gamma)$ is a di-

agonal matrix so that each element of the residual vector is affected only by a certain fault.

The multiple fault detection and isolation design objective is then to obtain suitable matrices L_ρ and W_ρ such that the elements of $r(t)$ have fixed direction in response to a certain fault with $G_{rf}(\gamma)$ in diagonal form.

4.3 Mathematical Results

This section presents six mathematical results [47] to describe multiple fault detection and isolation by fixed directional residuals for the unified delta model. Theorem 4.1 extends fixed directional residuals to the delta operator model by expressing the transfer function matrix from residual to fault, $G_{rf}(\gamma)$, in terms of its γ-domain eigenstructure. Corollary 4.1 shows that $G_{rf}(\gamma)$ can be expressed in terms of CK_ρ instead of CV_1. Corollary 4.2 proves that CK_ρ and CV_1 have the same column rank. Lemma 4.1 presents the projection matrix W_ρ to diagonalize the failure/residual map for the delta-operator systems, and shows how to compute W_ρ based on the observer's eigenvalues, the output coefficient matrix, and the failure signature matrix. Proposition 4.1 describes how to obtain the feedback gain matrix to assign the diagnostic observer's eigenstructure for the delta-operator model based on a result by Moore [21]. Theorem 4.2 presents a new bound for the fault free residuals. This bound is explicitly in terms of both eigenvalues and eigenvectors for the unified delta system, and is less conservative than the shift operator bound of Shen et al. [26]. These results comprise a unified framework for multiple fault detection and isolation that is valid for both continuous time and sampled data operation.

Fixed Directional Residuals for Delta-Operator Systems:

We use the $\gamma-$domain eigenstructure of the transfer function matrix $G_{rf}(\gamma)$ to extend the fixed directional residuals in Theorem 1 of Shen et al. [26] to delta operator systems.

Consider the γ-domain transfer function matrix between residual vector and fault in Eq.(4.24) where $G_{L\rho} = G_\rho - L_\rho C$ is a $n \times n$ nondefective real matrix with distinct γ-domain eigenvalues γ_i; $i = 1, \ldots, n$. Let v_i and ${p_i}^T$ denote the right and left eigenvectors, respectively, associated with a γ-domain eigenvalue γ_i of $G_{L\rho}$ for $i = 1, \ldots, n$. Let $V = [v_1 \ v_2 \ \ldots \ v_n]$, $P = [p_1 \ p_2 \ \ldots \ p_n]$ for $i = 1, \ldots, n$, and $k_{\rho j}$ for $j = 1, \ldots, p$ be the j^{th} column of K_ρ. Let all eigenvectors be appropriately scaled so that $VP^T = P^T V = I$ [48]. Then, $G_{rf}(\gamma)$ can be expanded using eigenstructure decomposition

$$G_{rf}(\gamma) = W_\rho C \left[\frac{v_1 {p_1}^T}{\gamma - \gamma_1} + \frac{v_2 {p_2}^T}{\gamma - \gamma_2} + \ldots\ldots \frac{v_n {p_n}^T}{\gamma - \gamma_n} \right] K_\rho. \tag{4.26}$$

Theorem 4.1

If

$$p_i^T k_{\rho j} : \begin{cases} = 0, & i \neq j \\ \neq 0, & i = j \end{cases} \quad \forall i = 1, \ldots, n, \quad \forall j = 1, \ldots, p; \quad p < r \leq n \tag{4.27}$$

Then,

$$G_{rf}(\gamma) = W_\rho \left[C v_1 \tfrac{<p_1, k_{\rho 1}>}{\gamma - \gamma_1}, \quad C v_2 \tfrac{<p_2, k_{\rho 2}>}{\gamma - \gamma_2}, \quad \ldots, \quad C v_p \tfrac{<p_p, k_{\rho p}>}{\gamma - \gamma_p} \right] \tag{4.28}$$

Proof: see Appendix D.

If the Cv_i are independent, then Eq.(4.28) is the fixed direction residual.

Allowable Failures for Multiple Fault Detection and Isolation by Fixed Directional Residuals for Delta Operator Systems:

Define $P_1 = [\ p_1, \ \ldots, \ p_p\ ]$, $V_1 = [\ v_1, \ \ldots, \ v_p\ ]$, $P_2 = [\ p_{p+1}, \ \ldots, \ p_n\ ]$ and $V_2 = [\ v_{p+1}, \ \ldots, \ v_n\ ]$.

Next, we show that $G_{rf}(\gamma)$ can be written in terms of CK_ρ instead of CV_1. This yields the allowable choices of failures K_ρ.

Corollary 4.1

If

$$p_i^T k_{\rho j} : \begin{cases} = 0, & i \neq j \\ \neq 0, & i = j \end{cases} \quad \forall i = 1, \ldots, n, \quad \forall j = 1, \ldots, p; \quad p < r \leq n \tag{4.29}$$

and if $VP^T = P^T V = I$, then

$$\begin{aligned} G_{rf}(\gamma) &= W_\rho C K_\rho \; diag\left(\frac{1}{\gamma - \gamma_j}\right), \quad j = 1, \ldots, p & (4.30) \\ &= W_\rho \left[\tfrac{Ck_{\rho_1}}{\gamma - \gamma_1}, \quad \ldots, \quad \tfrac{Ck_{\rho_p}}{\gamma - \gamma_p} \right] & (4.31) \end{aligned}$$

Proof: see Appendix E.

The allowable failures K_ρ are the set of $k_{\rho i}$ such that the $Ck_{\rho i}$ are independent.

We now show that CK_ρ and CV_1 have the same column rank. Therefore, the Cv_i in Eq.(4.28) are independent iff the $Ck_{\rho i}$ in Eq.(4.31) are independent.

Corollary 4.2

If

$$p_i^T k_{\rho j} : \begin{cases} = 0, & i \neq j \\ \neq 0, & i = j \end{cases} \quad \forall i = 1, \ldots, n, \quad \forall j = 1, \ldots, p, \quad p < r \leq n \tag{4.32}$$

and

$$VP^T = P^T V = I \tag{4.33}$$

Then, CK_ρ and CV_1 have the same column rank.

Proof: see Appendix F.

Projection Matrix W for Delta-Operator Systems:

We show how to compute the matrix W_ρ in terms of CK_ρ to diagonalize the failure/residual map for delta-operator systems. This is different from Shen et al.[26] who solve for W in terms of CV_1. This is an important distinction because if we optimize over only eigenvectors, then our W_ρ is independent of the optimization.

Lemma 4.1

Let CK_ρ be full column rank.

If

$$p_i^T k_{\rho j} : \begin{cases} = 0, & i \neq j \\ \neq 0, & i = j \end{cases} \quad \forall i = 1, \ldots, n, \quad \forall j = 1, \ldots, p, \quad p < r \leq n$$

and

$$VP^T = P^T V = I$$

and

$$W_\rho = diag\left(-\gamma_j\right)\left(CK_\rho\right)^\ddagger \tag{4.34}$$

where $(\cdot)^\ddagger$ is left inverse and $j = 1, \ldots, p$, then

$$G_{rf}(\gamma) = diag\left(\frac{-\gamma_j}{\gamma - \gamma_j}\right), \quad \text{with} \quad \left[G_{rf}(0)\right]_i = 1 \tag{4.35}$$

Proof: see Appendix G.

Extension of Moore Proposition to Delta Operator:

Shen et al.[26] state a theorem proven by Moore[21] for computing the observer gains. We now extend this result to the delta operator system.

Proposition 4.1

Given the system representation $(G_\rho, H_\rho, C, 0)$ and let $L_\rho \in \mathrm{R}^{n \times r}$. Suppose that $\Gamma = \{\gamma_1, \gamma_2, \ldots, \gamma_n\}$ is a distinct self-conjugate eigenvalue set of $(G_\rho - L_\rho C)$ including all unobservable eigenvalues of the pair (C, G_ρ). Let

$$S_{\gamma_i} = [\gamma_i I - {G_\rho}^T \quad C^T] \tag{4.36}$$

and let there be a compatibility partition matrix

$$\Sigma_{\gamma_i} = \begin{bmatrix} N_{\gamma_i} \\ M_{\gamma_i} \end{bmatrix} \tag{4.37}$$

whose columns constitute the basis of $\mathcal{N}(S_{\gamma_i})$, where $\mathcal{N}(\cdot)$ is the null space of $(\cdot)$. Then, $\exists\, \alpha_i \neq 0$ and $p_i = N_{\gamma_i}\alpha_i$ for $i = 1, 2, \ldots, n$ such that $\{p_1, p_2, \ldots, p_n\}$ are linearly independent and

$${p_i}^T[\gamma_i I - (G_\rho - L_\rho C)] = 0 \tag{4.38}$$

with

$$L_\rho = [p_1, \ldots, p_n]^{-T}[\xi_1, \ldots, \xi_n]^T \tag{4.39}$$

where $\xi_i = M_{\gamma_i}\alpha_i$

4.4 Robustness Results

We present a new result for the fault free residual bound. Our bound is explicitly in terms of both eigenvalues and eigenvectors for the unified delta operator system and is less conservative than the shift operator bound of Shen et al.[26].

Theorem 4.2 [47]

Let

$$\rho x(t) = [G_\rho + dG_\rho(x,u)]\, x(t) + [H_\rho + dH_\rho(x,u)]\, [u(t) + \mathrm{v}(t)] \tag{4.40}$$

$$y(t) = Cx(t) + w(t) \tag{4.41}$$

where $\mathrm{v}(t)$ and $w(t)$ are input and output disturbances, respectively. $dG_\rho(x,u)$ and $dH_\rho(x,u)$ are bounded uncertainties.

Let the observer dynamics be given by

$$\rho\hat{x}(t) = (G_\rho - L_\rho C)\,\hat{x}(t) + H_\rho u(t) + L_\rho\,[Cx(t) + w(t)] \tag{4.42}$$

where $(G_\rho - L_\rho C)$ is a stability matrix with distinct eigenvalues.

Define

$$d\tilde{e}(t) = dG_\rho(x,u)x(t) + dH_\rho(x,u)\,[u(t) + \mathrm{v}(t)] + H_\rho \mathrm{v}(t)$$

Let $VP^T = P^TV = I$, $\sup\limits_{0\le t<\infty} \|d\tilde{e}(t)\| < B_1$, $\sup\limits_{0\le t<\infty} \|w(t)\| < B_2$,

Then,

$$\|r(t)\| \le \|W_\rho CV\| \left[\left\|P^T e(0)\right\| + \frac{\|P\| \;\cdot B_1 + \left\|P^T L_\rho\right\| \cdot B_2}{f(\lambda)} \right] + \|W_\rho\|\,\|w(t)\| \tag{4.43}$$

where

$$f(\lambda) = \begin{cases} -\max\limits_{1\le i\le n} \mathrm{Re}\lambda_i; & \text{continuous time} \\ \\ \frac{1}{\Delta}\left[1 - \max\limits_{1\le i\le n} |1 + \Delta\gamma_i|\right]; & \text{discrete time} \end{cases}$$

Proof: see Appendix H.

We note that when optimizing over both eigenvalues and eigenvectors, our bound gives important insights into where the eigenvalues should be located to minimize the residual. The $\frac{1}{f(\lambda)}$ term indicates that the eigenvalues should be far away from the stability boundary whereas the $\|W_\rho\|$ term needs the eigenvalues to be close to the stability boundary.

We now show that our bound is less conservative than Shen et al.[26].
Let the eigenvalues be specified and fixed, because Shen et al.[26] optimize over eigenvectors only.
Let $B_3 = \frac{B_1}{f(\lambda)}$ and $B_4 = \frac{B2}{f(\lambda)}$ be constants.
Then,

$$\begin{aligned} \|r(t)\| &\leq \|W_\rho C\| \|V\| \left[\|P\| \|e(0)\| + B_3 \cdot \|P\| + B_4 \cdot \left\|P^T L_\rho\right\|\right] && (4.44) \\ &\qquad + \|W_\rho\| \|w(t)\| \\ &\leq \|W_\rho C\| \kappa_2(P) \left[\|e(0)\| + B_3 + B_4 \cdot \|L_\rho\|\right] + \|W_\rho\| \|w(t)\| && (4.45) \end{aligned}$$

This led Shen et al.[26] to minimize $\kappa_2(P)$.

4.5 Eigenvector Selection Criterion

In this section we propose an optimization that describes a new eigenvector selection criterion for robust FDI by fixed directional residuals to unstructured uncertainty and known initial condition mismatches. Our proposed optimization is given by [47]

1. Minimize over α_i, $i = 1, \ldots, n$ only:

$$J_1 = \|W_\rho C V\| \left[\beta_1 \left\|P^T e(0)\right\| + \beta_2 \|P\| + \beta_3 \left\|P^T L_\rho\right\|\right] \tag{4.46}$$

$$W_\rho = diag\left(-\gamma_j\right) \left(C K_\rho\right)^\ddagger, \quad j = 1, \ldots, p \tag{4.47}$$

2. Minimize over γ_i and α_i, $i = 1, \ldots, n$;

$$J_2 = \|W_\rho C V\| \left[\beta_5 \left\| P^T e(0) \right\| + \frac{\beta_6 \|P\| + \beta_7 \left\| P^T L_\rho \right\|}{f(\lambda)} \right] + \beta_8 \|W_\rho\| \qquad (4.48)$$

$$W_\rho = diag(-\gamma_j)(CK_\rho)^\ddagger, \quad j = 1, \ \ldots, \ p$$

We note that W_ρ is independent of all n eigenvectors.

4.6 Numerical Method for Robust and Multiple FDI of Actuator Failures by Fixed Directional Residuals for Delta Operator Systems

The numerical method follows from theorems 2, 3 and the algorithm of Shen et al.[26]. Our contribution is that (1) we minimize our new bound on the residual, and (2) we use our new equation for W that is independent of eigenvectors.

Numerical Method:

1. Choose the eigenvalues $\gamma_1, \ \gamma_2, \ \ldots, \ \gamma_n$ of $G_\rho - L_\rho C$.

   Compute $W_\rho = diag\left(-\gamma_i\right)\left(CK_\rho\right)^\ddagger$, $j = 1, \ldots, p$.

2. Compute $T_{K\rho} = [K_\rho \ \ \overline{K}_\rho]^{-1}$ where $\overline{K}_\rho \in \mathrm{R}^{n \times (n-p)}$ is an orthonormal basis of $\mathcal{N}\left(K_\rho^T\right)$

3. Compute $\tilde{G}_\rho = T_{K\rho} G_\rho T_{K\rho}^{-1}$, $\tilde{C} = C T_{K\rho}^{-1}$

4. For $i = p+1, \ \ldots, \ n$

   Find the basis $\hat{\Sigma}_{\gamma_i} = \begin{bmatrix} \hat{N}_{\gamma_i} \\ \hat{M}_{\gamma_i} \end{bmatrix}$ of $\mathcal{N}(\hat{S}_{\gamma_i})$

where $\hat{S}_{\gamma_i} = \begin{bmatrix} -\tilde{G}_{\rho 21}^T & \tilde{C}_1^T \\ \gamma_i I_{n-p} - \tilde{G}_{\rho 22}^T & \tilde{C}_2^T \end{bmatrix}$, $\tilde{G}_\rho = \begin{bmatrix} \tilde{G}_{\rho 11} & \tilde{G}_{\rho 12} \\ \tilde{G}_{\rho 21} & \tilde{G}_{\rho 22} \end{bmatrix}$, $\tilde{C} = [\tilde{C}_1 \;\; \tilde{C}_2]$

Set $\tilde{N}_{\gamma_i} = \begin{bmatrix} 0 \\ \hat{N}_{\gamma_i} \end{bmatrix}$

5. For $i = 1, \ \ldots, \ p$

   Compute $\hat{S}_{\gamma_i}^i = [\gamma_i e_i^n - \tilde{g}_{\rho i} \;\; \hat{S}_{\gamma_i}]$

   e_i^n is a vector of all zeros except with a one in the i^{th} row

   $\tilde{g}_{\rho i}^T$ is the i^{th} row of $\tilde{G}_\rho$

   Find the basis of $\mathcal{N}(\hat{S}_{\gamma_i}^i)$

$$\hat{\Sigma}_{\gamma_i}^i = \begin{bmatrix} \hat{N}_{\gamma_i}^i \\ \hat{M}_{\gamma_i}^i \end{bmatrix}, \quad i = 1, \ \ldots, \ p \tag{4.49}$$

   Let $\tilde{N}_{\gamma_i} = \begin{bmatrix} \Delta_i^p \hat{N}_{\gamma_i}^i \\ {}_1\hat{N}_{\gamma_i}^i \end{bmatrix}$ where $\Delta_i^p = [e_i^p \;\; 0_{p\times(n-p)}]$ and ${}_1\hat{N}_{\gamma_i}^i$ is a matrix with the rows of $\hat{N}_{\gamma_i}^i$ except the first row.

6. Obtain the assignable subspace $M_{\gamma_i} = \hat{M}_{\gamma_i}$, $N_{\gamma_i} = T_{K_\rho}^T \tilde{N}_{\gamma_i}$, and determine the dimensions of $\alpha_i, i = 1, \ldots, n$.

7. Initialize $\alpha_i, i = 1, \ldots, n$.

8. Optimize over α_i only:

$$\min_{\alpha_i} J_1, \quad \text{in Eq(4.46)}$$

$$p_i = N_{\gamma_i}\alpha_i, \;\; \xi_i = M_{\gamma_i}\alpha_i, \;\; i = 1, \ \ldots, \ n$$

$$L_\rho = P^{-T}\Xi^T, \;\; \text{where} \;\; \Xi = [\xi_1, \ \ldots, \ \xi_n]$$

Optimize over γ_i,α_i :

$$\min_{\gamma_i,\alpha_i} J_2, \quad \text{in Eq(4.48)}$$

$$p_i = N_{\gamma_i}\alpha_i, \;\; \xi_i = M_{\gamma_i}\alpha_i, \;\; i = 1, \; \ldots, \; n$$

$$L_\rho = P^{-T}\Xi^T, \;\; \text{where} \;\; \Xi = [\xi_1, \; \ldots, \; \xi_n]$$

4.7 Implementation and Example - Our Algorithm

In this section we implement the proposed FDI system in a vertical takeoff and landing (VTOL) aircraft subject to multiple bias failures in the control actuators and an initial condition mismatch in the vertical velocity state.

The VTOL aircraft that we consider is the continuous time linearized longitudinal dynamics of a helicopter in the vertical plane described by Narendra and Tripathi [27]. The state space model is given by

$$\dot{x}(t) = G_c x(t) + H_c u(t) \tag{4.50}$$

$$y(t) = C_c x(t) \tag{4.51}$$

where the state variables are horizontal velocity $v(knot)$, vertical velocity $w(knot)$, pitch rate $q(deg/s)$, and pitch angle $\theta(deg)$. The control variables are collective u_1, and longitudinal cyclic u_2. The continuous state space matrices G_c and H_c are shown below [27].

$$G_c \;=\; \begin{bmatrix} -0.0366 & 0.0271 & 0.0188 & -0.4555 \\ 0.0482 & -1.0100 & 0.0024 & -4.0208 \\ 0.1002 & 0.3681 & -0.7070 & 1.4200 \\ 0 & 0 & 1.0000 & 0 \end{bmatrix} \tag{4.52}$$

$$H_c \;=\; \begin{bmatrix} 0.4422 & 0.1761 \\ 3.5446 & -7.5922 \\ -5.5200 & 4.4900 \\ 0 & 0 \end{bmatrix} \tag{4.53}$$

Next, we compute the delta state space matrices G_δ, H_δ by applying the delta operator directly to the VTOL aircraft's continuous time model using function *c2del.m* from the MATLAB Delta Toolbox. We use the sampling rate chosen by Shen et al.[26] of $\Delta = 0.001$ seconds. This sampling rate may be unrealistically fast, but we use it so that we can compare our results with Shen et al.[26]. The delta operator state space matrices G_δ, H_δ, are used to full precision. However, they are shown here as displayed by MATLAB with a scaled fixed point format with 5 digits. The VTOL aircraft's delta operator state space matrices are shown below

$$G_\delta = \begin{bmatrix} -0.0366 & 0.0271 & 0.0186 & -0.4555 \\ 0.0482 & -1.0095 & 0.0004 & -4.0188 \\ 0.1002 & 0.3678 & -0.7060 & 1.4187 \\ 0.0001 & 0.0002 & 0.9996 & 0.0007 \end{bmatrix} \tag{4.54}$$

$$H_\delta = \begin{bmatrix} 0.4422 & 0.1760 \\ 3.5428 & -7.5884 \\ -5.5174 & 4.4870 \\ -0.0028 & 0.0022 \end{bmatrix} \tag{4.55}$$

We use the $C_c = C_\delta$ that was chosen by Shen et al.[26]. This $C_c = C_\delta$ is not realistic because the 4^{th} output is the sum of three sensor measurements. However, we use it so that we can compare our results with Shen et al.[26]. This $C_c = C_\delta$ is given by [26]

$$C_\delta = \begin{bmatrix} 1 & 0 & 0 & 0 \\ 0 & 1 & 0 & 0 \\ 0 & 0 & 1 & 0 \\ 0 & 1 & 1 & 1 \end{bmatrix} \tag{4.56}$$

The VTOL aircraft's open loop γ-domain eigenvalues $\gamma_{1,2} = 0.2758 \pm j0.2577$, $\gamma_3 = -0.2325$, and $\gamma_4 = -2.0705$ indicate that the VTOL aircraft is unstable. Therefore, we use eigenstructure assignment to compute a stabilizing output feedback gain matrix for the VTOL aircraft's delta operator model.

Multiple failures in the control actuators are modeled by letting the failure signature matrix K_δ take the values of the control coefficient matrix H_δ. The bias failure modes are described by

$$f(t) = \begin{bmatrix} f_{u_1} \\ f_{u_2} \end{bmatrix} \tag{4.57}$$

where

$$f_{u_1} = \begin{cases} 0, & t < t_{f_{u1}} \\ 2, & t \geq t_{f_{u1}} \end{cases} , \qquad f_{u_2} = \begin{cases} 0, & t < t_{f_{u2}} \\ -3, & t \geq t_{f_{u2}} \end{cases} \tag{4.58}$$

and the initial condition mismatch $e(0)$ in the vertical velocity state is given by

$$x(0) = \begin{bmatrix} 0 \\ 10 \\ 0 \\ 0 \end{bmatrix} = e(0) \tag{4.59}$$

We apply the numerical method in section 4.6 for the design of robust and multiple FDI of actuator failures for delta operator systems with eigenvector selection criterion given by the three-term weighted performance index presented in Eq.(4.46). The observer's eigenvalues are fixed in this case. Therefore, the calculation of the projection matrix W_ρ in Eq.(4.47) for sampled data operation is completely independent of the optimization. We compute the projection matrix W_δ at the beginning of the procedure after the observer's eigenvalues are chosen. The observer eigenvalues for this example are shown in Table 4.1, and the resulting projection matrix is

$$W_\delta = \begin{bmatrix} 20.4941 & -15.5188 & -122.2347 & -137.8147 \\ 11.0909 & -76.7598 & -15.3773 & -92.1448 \end{bmatrix}. \tag{4.60}$$

Next, we follow the construction procedure in steps 4 and 5 in section 4.6 to obtain the allowable subspaces $N_{\gamma_i},\ i = 1, \ldots, 4$. Then, the dimension of the eigenvector parameterization vector variables α_i, $i = 1, \ldots, 4$ are determined from the dimensions of the subspaces. Table 4.1 shows the dimensions of the allowable subspaces and eigenvector parameters α_i for each of the desired observer eigenvalues.

Table 4.1: Diagnostic observer's γ-domain eigenvalues, allowable subspaces and eigevector parameter α_i

eigenvalue	subspace	dimension	parameter	dimension
$\gamma_1 = -900$	N_{γ_1}	4×3	α_1	3×1
$\gamma_2 = -800$	N_{γ_2}	4×3	α_2	3×1
$\gamma_3 = -700$	N_{γ_3}	4×2	α_3	2×1
$\gamma_4 = -600$	N_{γ_4}	4×2	α_4	2×1

The parameter vector α of the optimization is then constructed from the eigenvector parameters $\alpha_i,\ i = 1, \ldots, 4$. The vector α is consistent with the order and dimensions of the subspaces for the allowable eigenvectors. In this example, α is a 10×1 vector with structure,

$$\alpha = \begin{bmatrix} \alpha_1 \\ \alpha_2 \\ \alpha_3 \\ \alpha_4 \end{bmatrix} \tag{4.61}$$

The optimization is arbitrarily initialized with pseudorandom values drawn from the standard normal distribution that are assigned to the initial α using MATLAB function *randn.m*. The optimization (i) uses the allowable subspaces in the original coordinate system, (ii) is performed directly and simultaneously over all eigenvector parameters α_i in α, and (iii) allows α to take values such that resulting observer left eigenvectors are not constrained to be unit vectors. We implement this unconstrained optimization using function *fminunc.m* from the Optimization Toolbox for use with MATLAB®. Optimal data provided by *fminunc.m* includes α (optimal values for optimization parameter α), the *exit flag* value (a convergence indicator), and the

$fval$ value (performance index value corresponding to optimal α).

Figure 4.2 contains the optimal data provided by $fminunc.m$ for 50 independent optimization runs. The $exitflag$ value on the top subplot is positive for all runs indicating that the optimization has converged. The subplot in the middle monitors the conditioning of the residual generators which is evaluated based on the condition number $\kappa(P)$ of the observer's left eigenvector matrix $P = [p_1 \; p_2 \; \ldots \; p_n]$. We observe that initial conditioning, κ_{init} in cyan is improved for all runs, and that values for optimal conditioning, κ_{optim} in black are within $5.099 \leq \kappa(P) \leq 8.705$ with 82% of $\kappa(P) \leq 6.2$ for all runs. This indicates that our algorithm yields diagnostic observers

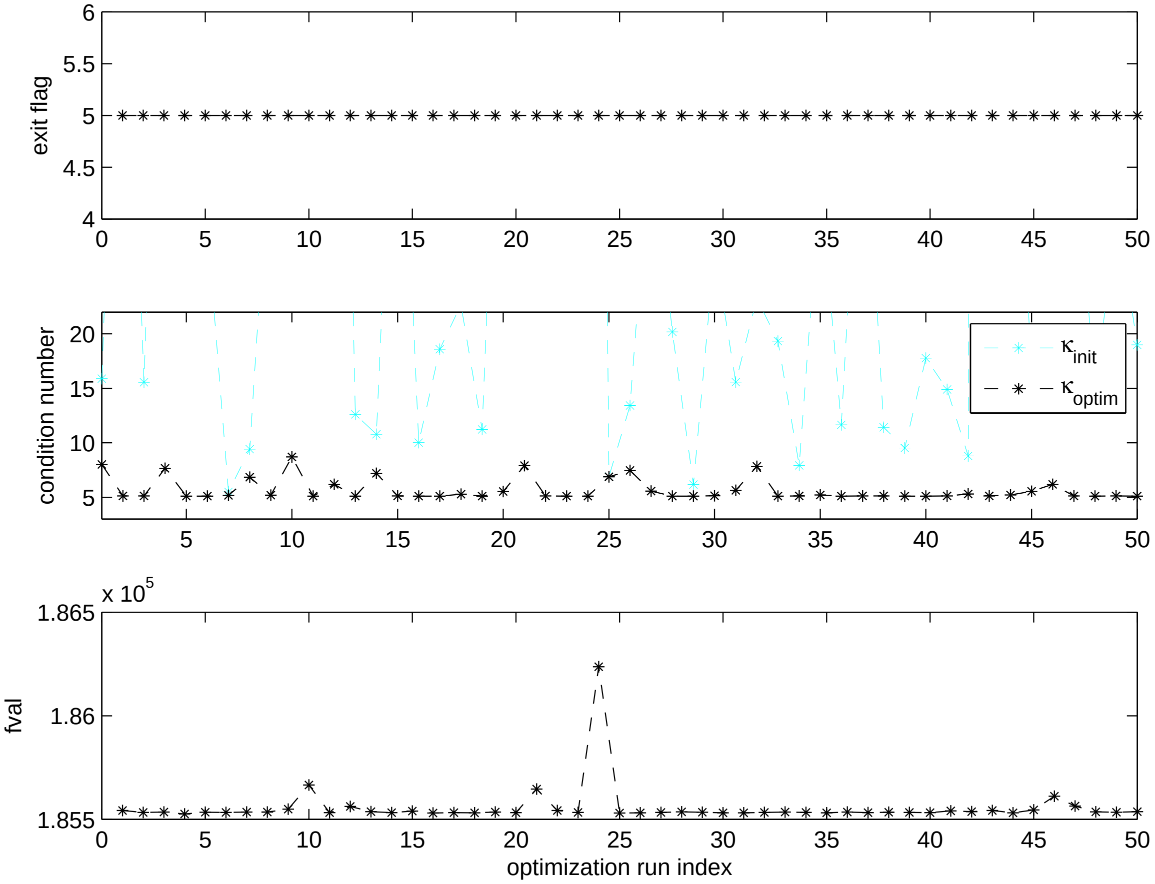

Figure 4.2: Optimization Results.

that are well-conditioned.The lower subplot shows $fval \approx 1.8556 \times 10^5$ with maximum variation of 0.36% in run-24. Table 4.2 shows optimal alphas for 5 arbitrarily selected runs from the 50 independent optimization runs. We observe that the sets for optimal alphas vary significantly from run to run even though the results from $fminuncon.m$ indicate that the optimization has converged for all runs.

Table 4.2: Optimal Alphas for runs 5, 13, 25, 39, 47

run	α_1	α_2	α_3	α_4
run-5	$\begin{bmatrix} -0.0065 \\ 1.1645 \\ 1.1573 \end{bmatrix}$	$\begin{bmatrix} 0.6464 \\ 0.0578 \\ 0.6965 \end{bmatrix}$	$\begin{bmatrix} 0.4274 \\ 1.1201 \end{bmatrix}$	$\begin{bmatrix} 1.1101 \\ -0.7138 \end{bmatrix}$
run-13	$\begin{bmatrix} -0.0087 \\ 1.4471 \\ 1.4376 \end{bmatrix}$	$\begin{bmatrix} 0.8042 \\ 0.0705 \\ 0.8645 \end{bmatrix}$	$\begin{bmatrix} -0.0752 \\ 1.4515 \end{bmatrix}$	$\begin{bmatrix} 1.7540 \\ -0.4415 \end{bmatrix}$
run-25	$\begin{bmatrix} -0.0088 \\ 1.3696 \\ 1.3561 \end{bmatrix}$	$\begin{bmatrix} 0.7584 \\ 0.0733 \\ 0.8176 \end{bmatrix}$	$\begin{bmatrix} 1.3423 \\ -0.3257 \end{bmatrix}$	$\begin{bmatrix} 0.2902 \\ 0.6618 \end{bmatrix}$
run-39	$\begin{bmatrix} -0.0093 \\ 1.3423 \\ 1.3363 \end{bmatrix}$	$\begin{bmatrix} 0.7473 \\ 0.0694 \\ 0.8019 \end{bmatrix}$	$\begin{bmatrix} 1.3102 \\ 0.3288 \end{bmatrix}$	$\begin{bmatrix} -0.5873 \\ 1.1707 \end{bmatrix}$
run-47	$\begin{bmatrix} -0.0022 \\ 1.4821 \\ 1.4761 \end{bmatrix}$	$\begin{bmatrix} 0.8413 \\ 0.1144 \\ 0.8682 \end{bmatrix}$	$\begin{bmatrix} -0.3789 \\ 1.2619 \end{bmatrix}$	$\begin{bmatrix} 1.1402 \\ 0.2904 \end{bmatrix}$

The type of convergence is revealed in Figure 4.3.a and Figure 4.3.b where initial alphas and optimal alphas for all 50 runs are shown in their corresponding 3-D and 2-D optimization space for α_i, $i = 1, \ldots, n$. Figure 4.3 shows that our implementation allows for convergence in direction for the eigenvector parameters associated with the failures (α_1 and α_2) while adding much flexibility for the eigenvector parameters which do not carry failure information (α_3 and α_4) in the 2-D optimization space. Table 4.2 and Figure 4.3 explain the nature of our algorithm solutions and anticipate the existence of different sets of eigenvectors that minimize the performance index, satisfy FDI design requirements, and have low conditioning. The sets of eigenvectors P with

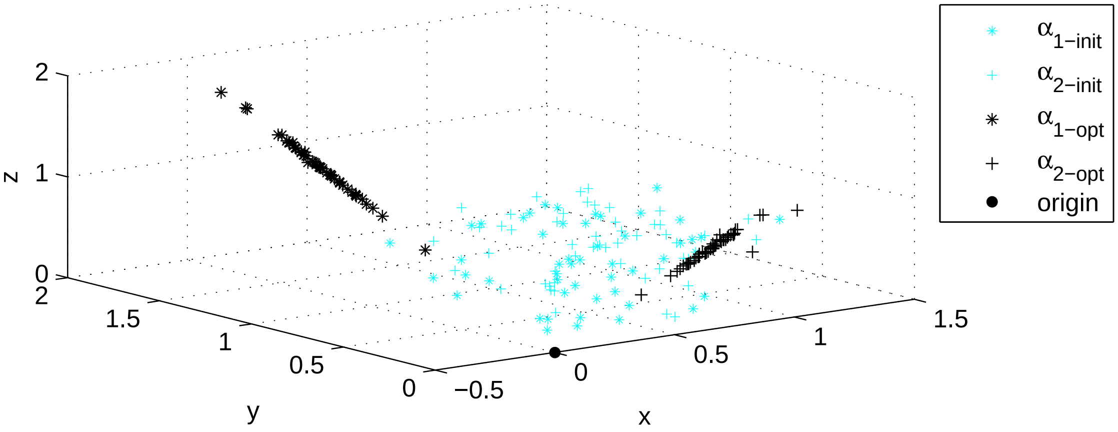
(a) 3−dimensional optimization space

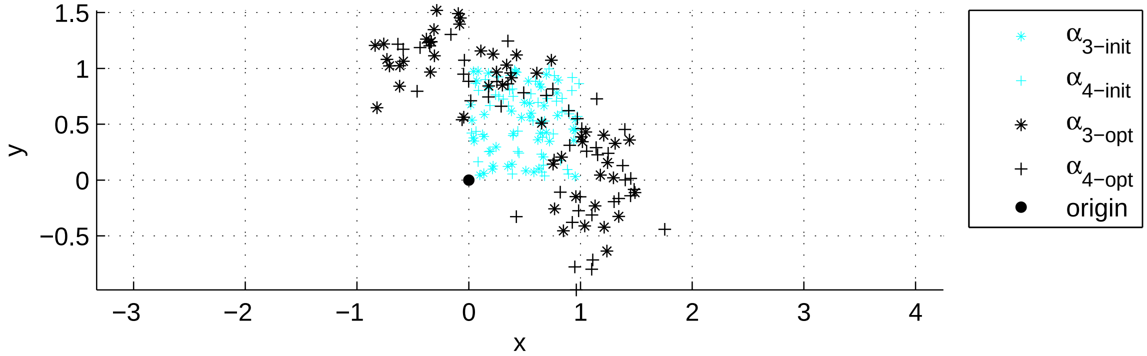
(b) 2−dimensional optimization space

Figure 4.3: Optimal Alphas

Table 4.3: P, L_δ for runs 5, 13, 25, 39, 47

run	P	L_δ
run-5	$\begin{bmatrix} -0.0002 & -0.0001 & 0.0011 & 0.0013 \\ 0.0015 & 0.0017 & 0.0001 & 0.0001 \\ 0.0026 & 0.0011 & 0.0002 & 0.0002 \\ 0.0014 & 0.0009 & 0.0008 & -0.0009 \end{bmatrix}$	$\begin{bmatrix} 658.0920 & -38.9717 & -49.8611 & 15.2150 \\ -19.4836 & 743.2036 & -98.8611 & -7.6449 \\ -44.1663 & -46.3006 & 816.6984 & 136.9548 \\ 69.3549 & -643.0047 & -639.1638 & 650.9448 \end{bmatrix}$
run-13	$\begin{bmatrix} -0.0002 & -0.0001 & 0.0006 & 0.0024 \\ 0.0019 & 0.0021 & 0.0001 & 0.0003 \\ 0.0032 & 0.0013 & 0.0001 & 0.0004 \\ 0.0017 & 0.0011 & 0.0012 & -0.0008 \end{bmatrix}$	$\begin{bmatrix} 622.1515 & -37.5893 & -49.8926 & 9.7427 \\ -12.9576 & 755.6137 & -86.1879 & -19.3124 \\ -38.4865 & -33.8947 & 829.3341 & 125.1952 \\ 45.9539 & -679.9894 & -677.0881 & 685.2665 \end{bmatrix}$
run-25	$\begin{bmatrix} -0.0002 & -0.0001 & 0.0016 & 0.0008 \\ 0.0018 & 0.0019 & 0.0002 & 0.0001 \\ 0.0030 & 0.0012 & 0.0002 & 0.0001 \\ 0.0016 & 0.0011 & -0.0005 & 0.0006 \end{bmatrix}$	$\begin{bmatrix} 661.9113 & 19.8636 & 9.1541 & -43.1858 \\ 38.5905 & 745.1309 & -94.6469 & -2.9637 \\ 12.0604 & -42.4828 & 822.7313 & 139.5353 \\ -101.1648 & -643.3676 & -646.2391 & 631.9035 \end{bmatrix}$
run-39	$\begin{bmatrix} -0.0002 & -0.0001 & 0.0019 & -0.0002 \\ 0.0017 & 0.0019 & 0.0002 & -0.0000 \\ 0.0029 & 0.0012 & 0.0003 & -0.0000 \\ 0.0016 & 0.0010 & 0.0000 & 0.0012 \end{bmatrix}$	$\begin{bmatrix} 703.4000 & 4.5076 & -4.5765 & -23.1086 \\ -0.2434 & 730.1456 & -111.1683 & 7.6025 \\ -23.9932 & -58.9954 & 804.7913 & 151.9451 \\ 16.5708 & -598.4306 & -596.6451 & 600.3641 \end{bmatrix}$
run-47	$\begin{bmatrix} -0.0002 & -0.0001 & 0.0001 & 0.0019 \\ 0.0019 & 0.0021 & 0.0000 & 0.0002 \\ 0.0033 & 0.0013 & 0.0000 & 0.0003 \\ 0.0017 & 0.0011 & 0.0011 & 0.0000 \end{bmatrix}$	$\begin{bmatrix} 604.2276 & -11.9871 & -24.9832 & -17.8991 \\ 0.7684 & 765.2884 & -75.9681 & -27.4251 \\ -29.9841 & -27.5218 & 836.0448 & 119.7898 \\ 13.3733 & -698.7534 & -697.1440 & 700.3231 \end{bmatrix}$

their corresponding observer feedback gain matrices L_δ for each of the 5 arbitrarily selected runs are shown in Table 4.3.

Next, we incorporate the closed-loop dynamics of the aircraft and the closed-loop dynamics of the diagnostic observer (including L_δ and W_δ) in a single composite system for simulation purposes for each of the 50 optimization runs. We define

$$X(t) = \begin{pmatrix} x(t) \\ \hat{x}(t) \end{pmatrix} , \quad X(0) = \begin{pmatrix} x(0) \\ 0_{(1\times n)} \end{pmatrix} , \quad \text{and} \quad Y(t) = \begin{pmatrix} y(t) \\ \hat{y}(t) \\ e(t) \end{pmatrix} , \tag{4.62}$$

where $x(t)$ is the aircraft state vector, $\hat{x}(t)$ is the state estimation vector, $y(t)$ is the aircraft output vector, $\hat{y}(t)$ is the output estimation vector, and $e(t)$ is the error vector. It can be easily shown that the composite model used for simulation is given by

$$\delta X(t) = \begin{bmatrix} G_\delta - H_\delta F_\delta C & 0_{(n\times n)} \\ L_\delta C - H_\delta F_\delta C & G_\delta - L_\delta C \end{bmatrix} X(t) + \begin{bmatrix} K_\delta \\ 0_{(n\times m)} \end{bmatrix} f(t) , \tag{4.63}$$

$$Y(t) = \begin{bmatrix} C & 0_{(r\times n)} \\ 0_{(r\times n)} & C \\ I_{(n\times n)} & -I_{(n\times n)} \end{bmatrix} X(t) , \tag{4.64}$$

$$r(t) = W_\delta C e(t) . \tag{4.65}$$

where F_δ in Eq.(4.63) is a stabilizing output feedback matrix such that $u(t) = -F_\delta y(t)$ and $u(t)$ is the aircraft input vector.

We perform simulations using each of the 50 independent composite systems that result from the 50 optimization runs. We examine the type of residual responses that our algorithm yields due to:

- The system is subjected to an initial condition mismatch in the vertical velocity state with the aircraft undergoing actuator failures at $t_{f_{u1}} = 60ms$ and $t_{f_{u2}} = 120ms$ - (Figure 4.4).

- Actuator failures occur early on in the simulation at $t_{f_{u1}} = 2ms$ and $t_{f_{u2}} = 6ms$ when the system is still under the effect of the initial condition mismatch in the vertical velocity state - (Figure 4.5).

Each of the two components of the residual vector is shown in a separate subplot in Figures 4.4 and 4.5 in black, while the actual failure in the actuator is shown in red.

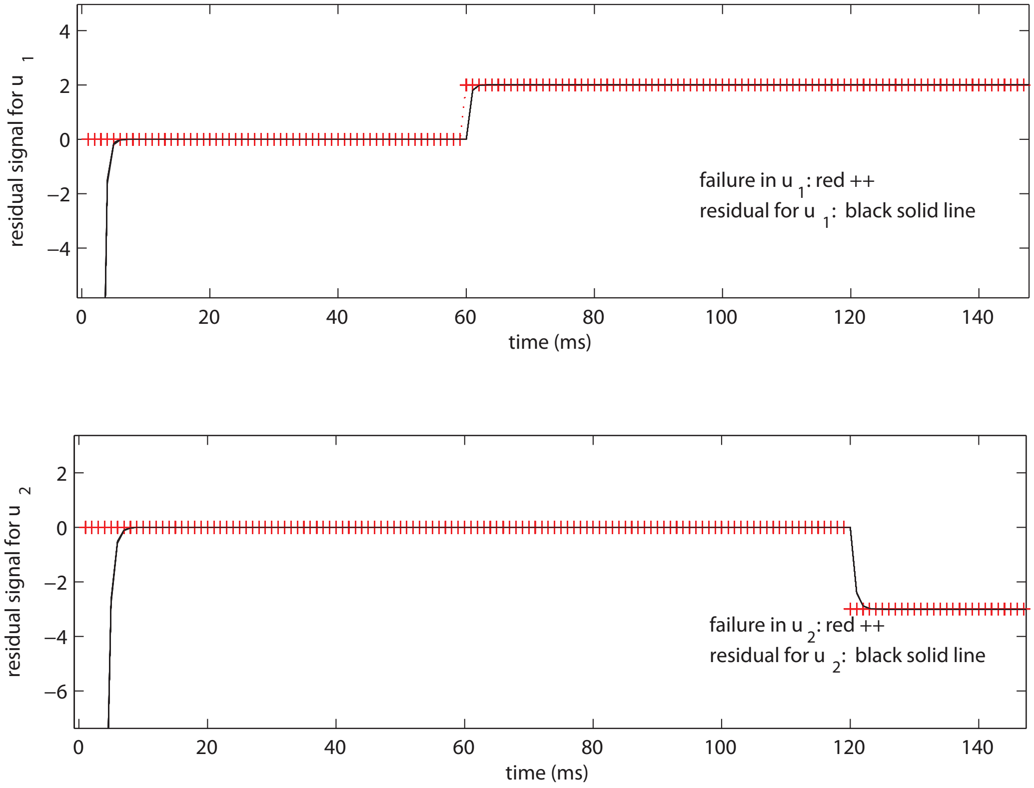

Figure 4.4: Residual response to failure-initial mismatch separate effect.

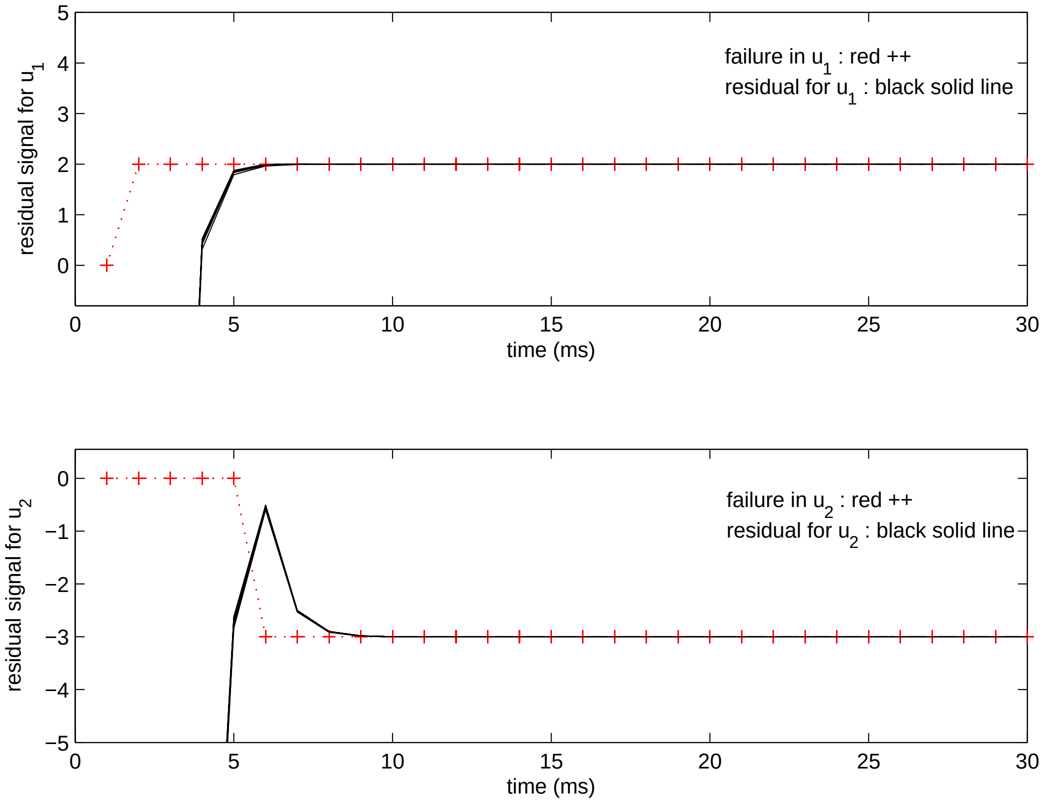

Figure 4.5: Residual response to failure-initial mismatch combined effect.

We observe that:

- All 50 responses are tightly similar for both residual components in both Figure 4.4 and Figure 4.5.
- Subsequent to the transient due to the initial mismatch, both residual components are zero in the absence of actuator failures (Figure 4.4).
- In the presence of a bias failure, residual components are no longer zero, and furthermore the value of the bias failures are indicated by the steady state values of the residual signals (Figure 4.4 and Figure 4.5).
- The first residual component (in both top subplots) responds only to actuator failures in u_1 and its time response is completely decoupled from the actuator

of u_2. Similarly, the second residual component (in both bottom subplots) responds only to actuator failures in u_2 and it is completely decoupled from the actuator of u_1 (Figure 4.4 and Figure 4.5).

- Within 4ms from a failure time, fault detection and isolation is achieved for all residual responses (Figure 4.4 and Figure 4.5).

We conclude that our algorithm yields excellent and highly consistent fixed directional residual responses that are well suited for multiple FDI with a detection time of about 4ms for 1ms sampled data for all runs.

4.8 Algorithm Consistency

In this section we evaluate our algorithm by comparing the consistency of our algorithm with Shen et al.[26]. The algorithm in [26] for robust and multiple FDI also makes use of an eigenstructure-based optimization to select the eigenvectors of the diagnostic observer. We show that the algorithm in [26] leads to residual responses that vary significantly from run to run. This is problematic when there is a need to impose a threshold over the optimal residual responses. Furthermore, detection time can not be determined in this case. Conversely, our algorithm yields residual responses of excellent and highly consistent performance for all runs. The detection time of our algorithm can be determined and threshold values for our residual signals can be established.

Shen et al.[26] use the shift operator for their development. Therefore, we implement the algorithm for robust FDI in [26] for the shift operator model of the VTOL aircraft subject to the same multiple bias failures in the control actuators and initial condition mismatch that we used in section 4.7. We perform 50 independent runs of Shen et al.[26] optimization. The 50 runs were initialized with the same initial alphas that we use in section 4.7 to initialize our optimization. Finally, residual responses from Shen et al.[26] are compared with our delta operator residual responses for the 50 optimization runs.

The eigenvector selection criteria for robust FDI proposed by Shen et al. [26] is the minimization of the condition number $\kappa(P)$ alone, where P is the matrix which columns are the observer's left eigenvectors p_i of unit length, for $i = 1, \dots,\ 4$. The authors in [26] explain that the condition number $\kappa(P)$ of the diagnostic observer can be minimized by making the eigenstructure as orthonormal as possible. For that reason, the authors in [26] use the rank-one updating method for the optimization of the condition number $\kappa(P)$ to obtain a set of orthonormal vectors for the design of the diagnostic observer.

Shen et al. [26], also present the following two expressions to calculate the projection matrix W:

$$W = diag(\omega_j)(CV_1)^{\ddagger}\ , j = 1, \dots, p\ , \tag{4.66}$$

and

$$W = diag(\omega_j)(V_1)^{\ddagger}C^{-1}\ , j = 1, \dots, p\ , \tag{4.67}$$

where V_1 is the matrix which columns are the first v_j right eigenvectors of the diagnostic observer, and $\omega_j = \frac{1-\lambda_j}{p_j^T K_j}$, $j = 1, \dots, p$, where p is the number of control actuators. The authors in [26] use Eq. (4.67) which leads to impractical cases as it requires the output coefficient matrix C to be square and invertible.

Given the above, we implement Shen et al. [26] algorithm for robust FDI by fixed directional residuals by

- Minimizing the condition number $\kappa(P)$ using function *fmincon.m* from MAT-

LAB Optimization Toolbox [45] instead of the rank-one method used in [26].

- Optimizing directly over the eigenvector parameter vector α, where $\alpha = \begin{bmatrix} \alpha_1 \\ \alpha_2 \\ \alpha_3 \\ \alpha_4 \end{bmatrix}$.
- Constraining α_i, $i = 1, 2, 3, 4$ such that all resulting eigenvectors are unit vectors.
- Calculating the projection matrix W using Eq.(4.66).

This implementation yields the same type of solutions that the original implementation for robust FDI in [26] would yield: orthonormal eigenvectors that minimize the condition number $\kappa(P)$ while satisfying design requirements for multiple FDI by fixed directional residuals, yet it does not lead to impractical cases.

First, the shift operator state space matrices G_q, H_q are computed by applying the shift operator directly to the VTOL aircraft's continuous time model using MATLAB function *c2d.m*. The sampling period is 0.001 seconds as in section 4.7. The shift operator state space matrices G_q, H_q, C_q are used to full precision. However, the values are shown here as displayed by MATLAB with a scaled fixed point format with 5 digits.

The VTOL aircraft's discrete shift operator state space matrices are shown below

$$G_q = \begin{bmatrix} 1.0000 & 0.0000 & 0.0000 & -0.0005 \\ 0.0000 & 0.9990 & 0.0000 & -0.0040 \\ 0.0001 & 0.0004 & 0.9993 & 0.0014 \\ 0.0000 & 0.0000 & 0.0010 & 1.0000 \end{bmatrix} \tag{4.68}$$

$$H_q = \begin{bmatrix} 0.0004 & 0.0002 \\ 0.0035 & -0.0076 \\ -0.0055 & 0.0045 \\ -0.0000 & 0.0000 \end{bmatrix} \tag{4.69}$$

$$C_q = \begin{bmatrix} 1 & 0 & 0 & 0 \\ 0 & 1 & 0 & 0 \\ 0 & 0 & 1 & 0 \\ 0 & 1 & 1 & 1 \end{bmatrix} \tag{4.70}$$

We use eigenstructure assignment to compute a stabilizing output feedback gain matrix for the VTOL aircraft's shift operator model.

The z-domain values for the desired observer eigenvalues λ_i, the dimensions of the corresponding allowable subspaces N_{λ_i}, and the dimensions of eigenvector parameters α_i, for $i = 1, \ldots, 4$ are shown in Table 4.4. The z-domain eigenvalues λ_i in Table 4.4 and the γ-domain eigenvalues γ_i in Table 4.1 correspond to the same eigenvalues in the s-domain. We observe that the dimensions for the subspaces in the z-domain (Table 4.4) and in the γ-domain (Table 4.1) are the same. Therefore, we use the structure for the optimization parameter α shown in Eq.(4.61).

Table 4.4: Diagnostic observer's z-domain eigenvalues, allowable subspaces and eigevector parameter α_i

eigenvalue	subspace	dimension	parameter	dimension
$\lambda_1 = 0.1$	N_{λ_1}	4×3	α_1	3×1
$\lambda_2 = 0.2$	N_{λ_2}	4×3	α_2	3×1
$\lambda_3 = 0.3$	N_{λ_3}	4×2	α_3	2×1
$\lambda_4 = 0.4$	N_{λ_4}	4×2	α_4	2×1

Figure 4.6, Table 4.5, Figure 4.7, Table 4.6, and Eq.(4.71) show the results for 50 runs of the optimization proposed in [26]. These runs are initialized with the same initial alphas that were used in section 4.7 to initialize our algorithm.

The exit flag values in Figure 4.6 indicate that all runs have converged and have achieved the same minimum condition number of $\kappa(P) \approx 4.11$ as in [26]. Table 4.5 shows that the algorithm in [26] yields sets of optimal α_i, $i = 1, \ldots, 4$ that are different from run to run. Figure 4.7 shows that α_1 and α_2 converge to 2 points along the corresponding direction of convergence in the 3-D optimization space (Figure 4.7.a), while α_3 and α_4 in the 2D space (Figure 4.7.b) have flexibility in direction but are restricted in magnitude. Optimization convergence for different sets of alphas indicate that there are different sets of eigenvectors that satisfy the design requirements for multiple FDI by fixed directional residuals. We note that different sets of eigenvectors also take place in the implementation of our algorithm in section 4.7. Table 4.6 shows the different sets of eigenvectors P and the corresponding observer gain feedback matrices L.

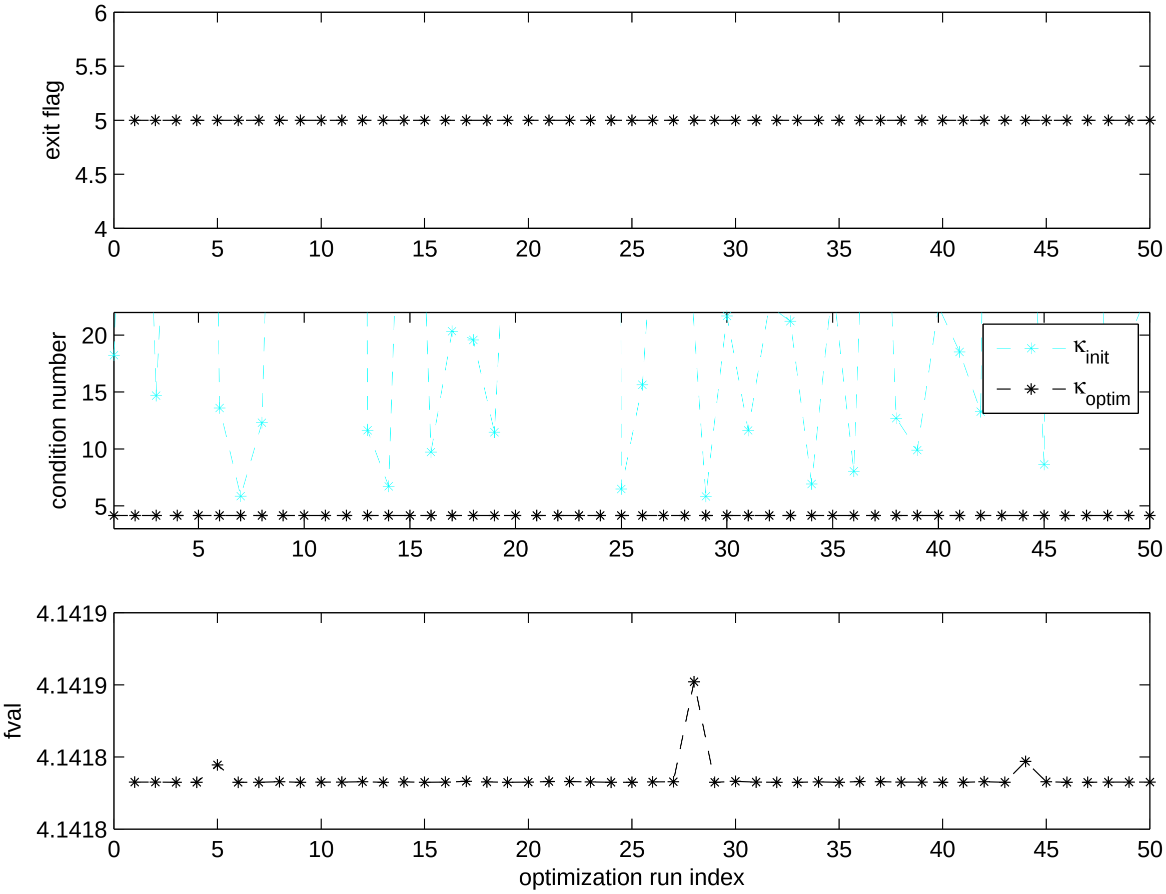

Figure 4.6: Optimization Results - Shen et al. algorithm.

Table 4.5: Optimal Alphas for runs 5, 13, 25, 39, 47 - Shen et al. algorithm.

run	α_1	α_2	α_3	α_4
run-5	$\begin{bmatrix} -0.4226 \\ -0.7899 \\ 0.0775 \end{bmatrix}$	$\begin{bmatrix} -0.6420 \\ -0.4817 \\ 0.0445 \end{bmatrix}$	$\begin{bmatrix} -0.1977 \\ -1.4973 \end{bmatrix}$	$\begin{bmatrix} 0.3942 \\ -1.3900 \end{bmatrix}$
run-13	$\begin{bmatrix} 0.4253 \\ 0.7892 \\ -0.0766 \end{bmatrix}$	$\begin{bmatrix} 0.6419 \\ 0.4796 \\ -0.0427 \end{bmatrix}$	$\begin{bmatrix} 0.1030 \\ 1.5262 \end{bmatrix}$	$\begin{bmatrix} 1.1730 \\ -0.0379 \end{bmatrix}$
run-25	$\begin{bmatrix} 0.4254 \\ 0.7892 \\ -0.0766 \end{bmatrix}$	$\begin{bmatrix} 0.6419 \\ 0.4796 \\ -0.0427 \end{bmatrix}$	$\begin{bmatrix} 0.8768 \\ -1.2247 \end{bmatrix}$	$\begin{bmatrix} 0.9487 \\ 0.7363 \end{bmatrix}$
run-39	$\begin{bmatrix} 0.4251 \\ 0.7892 \\ -0.0765 \end{bmatrix}$	$\begin{bmatrix} 0.6419 \\ 0.4794 \\ -0.0426 \end{bmatrix}$	$\begin{bmatrix} 0.4284 \\ 1.3863 \end{bmatrix}$	$\begin{bmatrix} -1.1652 \\ -0.0579 \end{bmatrix}$
run-47	$\begin{bmatrix} 0.4253 \\ 0.7892 \\ -0.0766 \end{bmatrix}$	$\begin{bmatrix} 0.6419 \\ 0.4796 \\ -0.0427 \end{bmatrix}$	$\begin{bmatrix} 0.8524 \\ 0.9915 \end{bmatrix}$	$\begin{bmatrix} 0.8382 \\ -1.0961 \end{bmatrix}$

(a) 3−dimensional optimization space

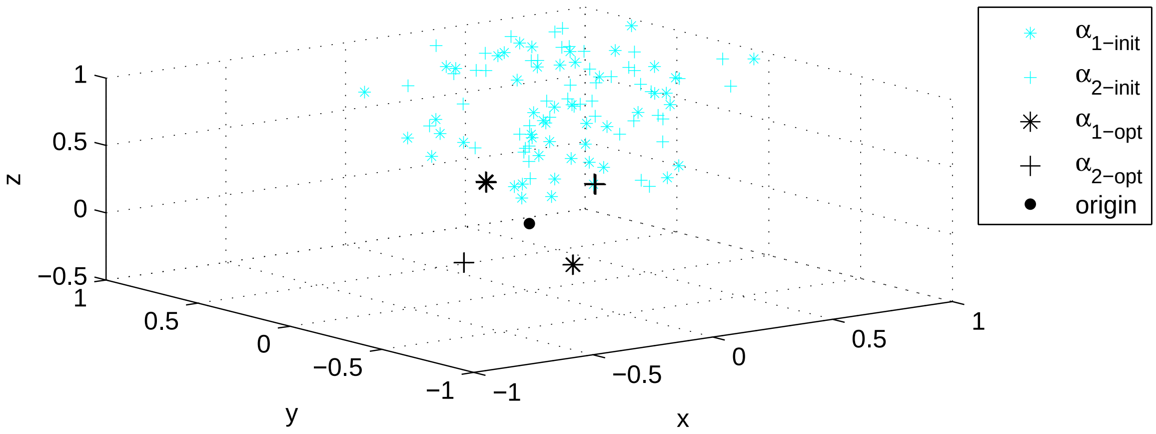

(b) 2−dimensional optimization space

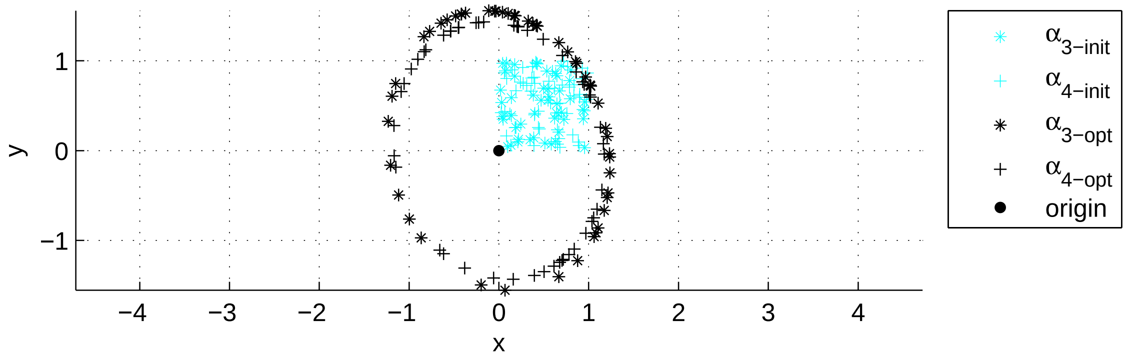

Figure 4.7: Optimal Alphas - Shen et al. algorithm.

Table 4.6: P, L for runs 5, 13, 25, 39, 47 - Shen et al. algorithm.

run	P	L
run-5	$\begin{bmatrix} 0.1884 & 0.1763 & 0.5517 & 0.0544 \\ -0.4966 & -0.8346 & 0.0628 & 0.0062 \\ -0.8473 & -0.5218 & 0.0849 & 0.0088 \\ -0.0009 & 0.0011 & -0.8274 & -0.9985 \end{bmatrix}$	$\begin{bmatrix} 0.7149 & 0.1407 & 0.1322 & -0.1580 \\ 0.0123 & 0.7619 & -0.0789 & -0.0227 \\ -0.0482 & 0.1125 & 0.9754 & -0.0223 \\ 0.0059 & -0.5904 & -0.5890 & 0.5911 \end{bmatrix}$
run-13	$\begin{bmatrix} -0.1864 & -0.1750 & -0.4874 & -0.9289 \\ 0.4969 & 0.8348 & -0.0555 & -0.1057 \\ 0.8476 & 0.5220 & -0.0751 & -0.1422 \\ 0.0004 & 0.0003 & 0.8682 & -0.3251 \end{bmatrix}$	$\begin{bmatrix} 0.6256 & 0.0012 & -0.0109 & -0.0287 \\ 0.0019 & 0.7453 & -0.0959 & -0.0073 \\ -0.0613 & 0.0915 & 0.9539 & -0.0028 \\ -0.0469 & -0.6889 & -0.6896 & 0.6836 \end{bmatrix}$
run-25	$\begin{bmatrix} -0.1864 & -0.1750 & -0.3388 & -0.9554 \\ 0.4969 & 0.8348 & -0.0385 & -0.1087 \\ 0.8476 & 0.5220 & -0.0514 & -0.1465 \\ 0.0004 & 0.0003 & -0.9387 & 0.2322 \end{bmatrix}$	$\begin{bmatrix} 0.6175 & -0.0495 & -0.0620 & 0.0211 \\ 0.0010 & 0.7395 & -0.1018 & -0.0016 \\ -0.0626 & 0.0837 & 0.9461 & 0.0048 \\ 0.0331 & -0.6881 & -0.6857 & 0.6919 \end{bmatrix}$
run-39	$\begin{bmatrix} -0.1864 & -0.1749 & -0.6974 & 0.9482 \\ 0.4968 & 0.8348 & -0.0794 & 0.1079 \\ 0.8476 & 0.5220 & -0.1072 & 0.1451 \\ 0.0006 & 0.0004 & 0.7042 & 0.2613 \end{bmatrix}$	$\begin{bmatrix} 0.6304 & -0.0055 & -0.0175 & -0.0214 \\ 0.0025 & 0.7445 & -0.0967 & -0.0065 \\ -0.0606 & 0.0904 & 0.9528 & -0.0016 \\ -0.0778 & -0.6874 & -0.6893 & 0.6786 \end{bmatrix}$
run-47	$\begin{bmatrix} -0.1864 & -0.1750 & -0.9141 & -0.3792 \\ 0.4969 & 0.8348 & -0.1040 & -0.0432 \\ 0.8476 & 0.5220 & -0.1402 & -0.0576 \\ 0.0004 & 0.0003 & 0.3660 & -0.9225 \end{bmatrix}$	$\begin{bmatrix} 0.6926 & 0.0138 & 0.0043 & -0.0336 \\ 0.0095 & 0.7467 & -0.0942 & -0.0078 \\ -0.0510 & 0.0934 & 0.9562 & -0.0035 \\ -0.0353 & -0.6181 & -0.6184 & 0.6141 \end{bmatrix}$

Eq.(4.71) shows the projection matrix W which is calculated by using Eq.(4.66) where W is a function of the observer eigenvectors. All 50 sets of optimal eigenvectors result in the same projection matrix W in Eq.(4.71). We note that Eq.(4.66) is misleading since W is independent of the observer eigenvectors, as we have shown in our Lemma 4.1

$$W = \begin{bmatrix} 20.4713 & -15.5016 & -122.0990 & -137.6617 \\ 11.0770 & -76.6640 & -15.3581 & -92.0297 \end{bmatrix} \tag{4.71}$$

Figure 4.8 and Figure 4.9 compare the residual responses from our algorithm (in black) and the residual responses from the algorithm proposed in [26] (in cyan) for all 50 runs and for the same simulation conditions as in section 4.7. Residual responses due to failure-initial condition mismatch separate effect simulated in section 4.7 are shown in Figure 4.8, and residual responses due to failure-initial condition mismatch combined effect are shown in Figure 4.9.

We observe that both algorithms yield fixed directional residuals capable of detecting and isolating multiple failures in the control actuators. However, the residual responses (in cyan) from the algorithm proposed in [26], vary significantly from run to run. Conversely, the residual responses from our algorithm (in black) are tightly consistent for all 50 runs. Consequently, the detection time for our algorithm can be determined to be approximately $4ms$ for $1ms$ sampled data operation for all runs. However, the detection time can not be determined for algorithms with inconsistent residual responses for all runs such as the algorithm proposed in [26].

Optimization and simulation results in sections 4.7 and 4.8 show that eigenstructure-based optimizations can lead to different sets of eigenvectors that minimize the performance index. These different sets of eigenvectors yield time responses that vary significantly which is problematic when there is a need to impose a threshold over the optimal time responses as is the case of FDI signals. This fact has not been addressed in the literature on eigenstructure-based optimizations for fixed directional residual design. In contrast, our optimization and simulation results show that our FDI algorithm yields different sets of eigenvectors that minimize the performance index, satisfy FDI design requirements, have low condition number, and result in excellent and tightly similar residual responses with a detection time of about 4ms for 1ms sampled data for all runs.

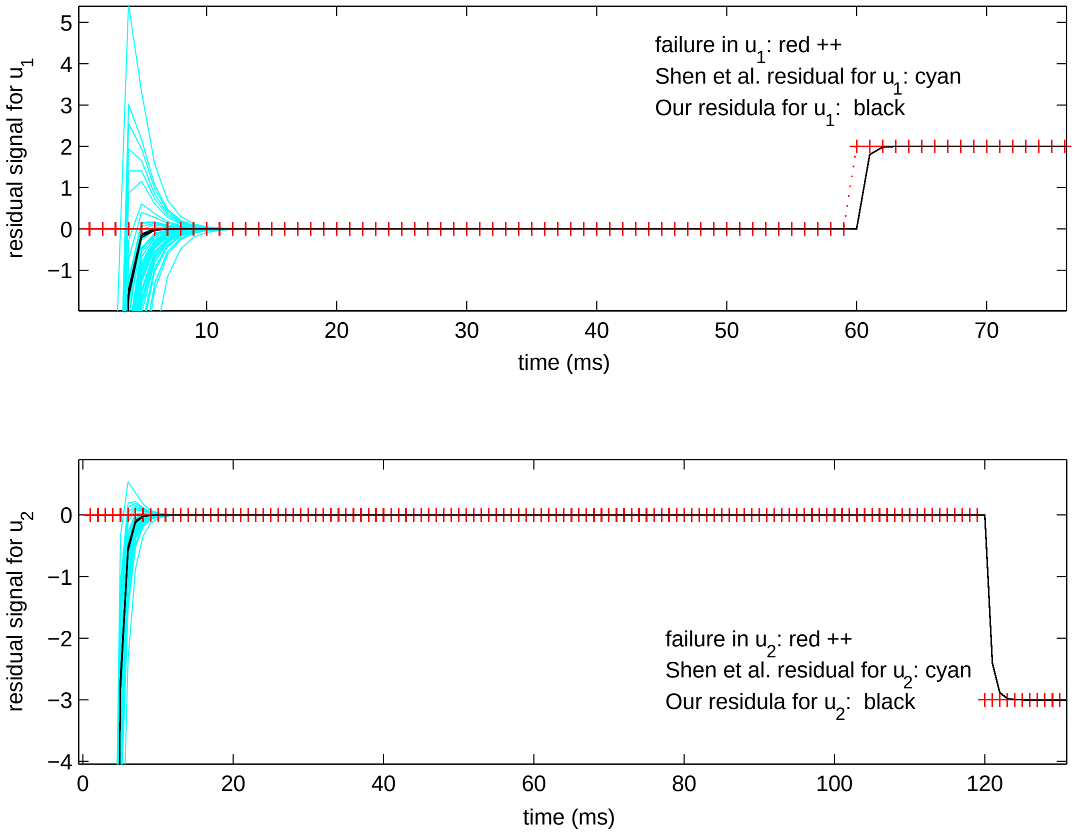

Figure 4.8: Residual response to failure-initial mismatch separate effect.

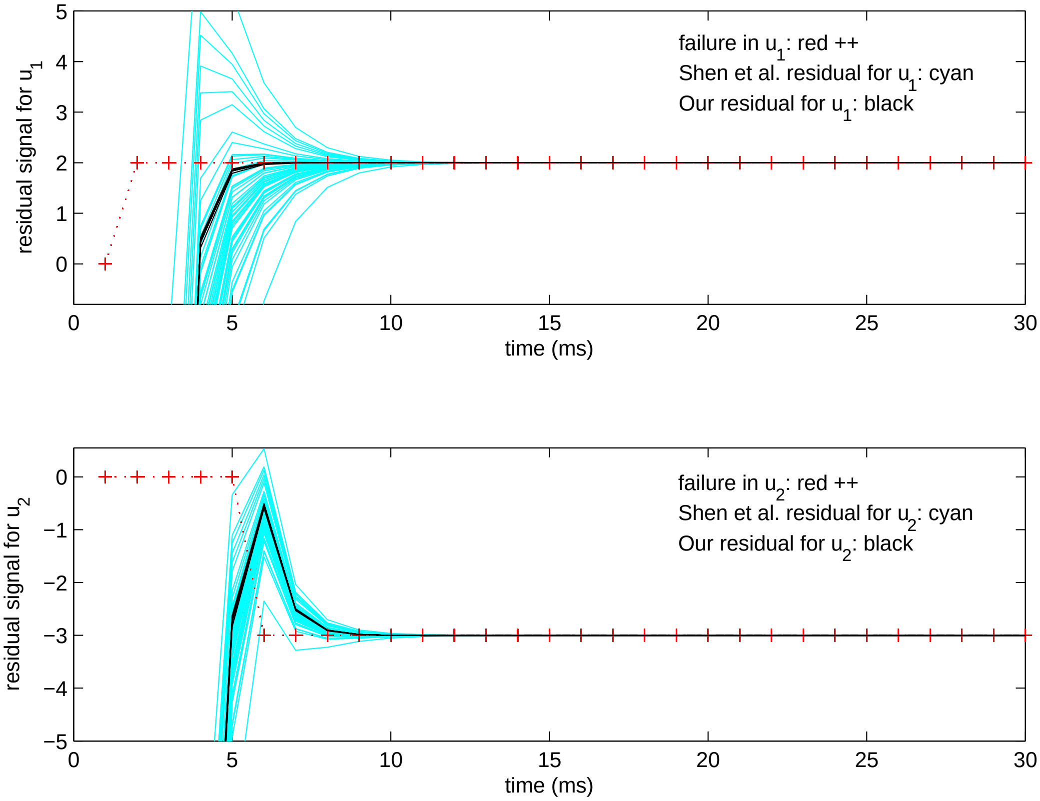

Figure 4.9: Residual response to failure-initial mismatch combined effect.

Chapter 5

Concluding Remarks

5.1 Conclusions

This research has proposed new results for the application of eigenstructure assignment to (*i*) the design of a flight control system for the continuous model and the delta operator model of the ICE tailless aircraft, (*ii*) the reconfiguration of the flight control system of the ICE tailless aircraft under symmetric lock in place failures of either the elevons or the all moving tips and (*iii*) the design of fixed directional residuals suited for multiple fault detection and isolation of a variety of failures in the control actuators for delta operator systems.

In chapter 2, we have designed a flight control system for the ICE tailless aircraft that includes thrust vectoring. Our longitudinal controller is a cstar command system and our lateral controller is a stability axis roll rate command system. Our design achieves MIL-F-8785C mode specifications on the short period, phugoid, dutch roll, roll subsidence and spiral modes, and achieves MIL-F-9490D specifications on phase and gain margins. The robustness of the design is further demonstrated by closed loop margins based upon mu-values and monte carlo simulations. The performance of the flight control system is evaluated by using a 6DOF nonlinear simulation of the ICE aircraft. Nonlinear simulation results show good performance to cstar and stability axis roll rate commands.

In chapter 3, we have extended the continuous time eigenstructure assignment design of the flight control system for the ICE tailless aircraft to the delta operator model. Theorem 3.1 derives an expression for complex $\gamma - plane$ eigenvalues in terms of damping ratio ζ and natural frequency ω_n. Theorem 3.2 shows that a failure in continuous time body axes is equivalent to the same failure in delta operator stability axes. Theorem 3.3 proves a new result that extends disk gain and phase margins to the delta operator system. We considered symmetric lock in place failures of either the elevons or the all moving tips. We proposed a novel eigenstructure assignment reconfiguration in which we first switch to a new recomputed gain to achieve satisfactory time responses. Then, we perform an optimization to achieve specifications on the disk gain and phase margins. We then switch to a second set of gains when the optimization achieves a feasible solution. We presented simulation results using a full 6DOF nonlinear simulation. We showed that an all moving tip failure causes the aircraft to become unstable whereas our eigenstructure assignment reconfigured flight control system yields responses that are similar to the unfailed responses. We also showed that an elevon failure requires the feasible solution from an optimization to satisfy the disk gain and phase margin specifications in all channels.

In chapter 4, we have extended multiple and simultaneous fault detection and isolation (FDI) system design by a single diagnostic observer to the unified delta operator model that is valid for both continuous time and sampled data operation. Theorem 4.1 extends fixed directional residuals to the delta operator model. Corollary 4.1 with corollary 4.2 show that allowable failure signatures K_ρ, for multiple FDI by the unified delta-operator fixed directional residuals, have full column rank. Lemma 4.1 presents the projection matrix W_ρ to diagonalize the failure/residual map for delta-operator systems. Proposition 4.1 describes how to obtain the feedback gain matrix to assign the diagnostic observer's eigenstructure for the delta-operator model based on a previous result by Moore [21]. Theorem 4.2 presents a new result for the fault free residual bound. This bound is explicitly in terms of both eigenvalues and eigenvectors for the unified delta system and is less conservative than the shift operator bound previously presented by Shen et al. [26].

In chapter 4, we have also proposed a new method/algorithm for multiple and simultaneous FDI of control actuator failures for delta operator systems. This method is applied to the design of a FDI system for the delta operator model of the linearized longitudinal dynamics of a VTOL aircraft in the vertical plane, subject to an initial condition mismatch in the vertical velocity state and bias failures in the control actuators. This method/algorithm is compared to the algorithm proposed by Shen et al. [26]. We showed that two algorithms that use eigenstructure-based optimizations to design fixed directional residuals yield different sets of eigenvectors that satisfy FDI requirements. Therefore, residual responses can vary significantly from run to run. In contrast, our algorithm for robust FDI yields different sets of eigenvectors that minimize the performance index, satisfy FDI design requirements, have low condition number, and result in excellent and highly consistent residual responses. Therefore, the detection time for our algorithm was determined to be approximately 4ms for a 1ms sampled data operation.

The work of this thesis is documented in the following papers:

Nieto-Wire, C., and Sobel, K.M., *"Eigenstructure Assigment for a Tailless Aircraft"*.

AIAA Guidance, Navigation, and Control Conference, Hilton Head, SC, August 20-23, 2007, AIAA Paper 2007-6417.

Nieto-Wire, C., and Sobel, K.M., *"Reconfigurable Delta Operator Eigenstructure Assignment for a Tailless Aircraft"*. AIAA Guidance, Navigation, and Control Conference, Chicago, IL, August 10-11, 2009, AIAA Paper 2009-6306.

Nieto-Wire, C. and Sobel, K., *"Observer-based residual generator design for multiple fault detection and isolation"*. in Junior Scientist Conference, Vienna, Austria, April 2010, pp. 91-92.

Nieto-Wire, C. and Sobel, K., *"Flight Control Design for a Tailless Aircraft Using Eigenstructure Assignment"*. International Journal of Aerospace Engineering, vol. 2011, Article ID 549131, 13 pages, 2011. doi:10.1155/2011/549131.

5.2 Problems and Recommendations

Eigenstructure assignment was applied to (i) the design of a flight control system for the ICE tailless aircraft, (ii) the eigenstructure assignment reconfiguration of the ICE tailless aircraft subject to symmetric failures in the lateral control actuators, and (iii) the design of fixed directional residuals for multiple and simultaneous FDI of failures in the control actuators. The analysis, control law, control reconfiguration, and algorithm for multiple FDI in (i), (ii), and (iii) are all based on the linearized dynamics of the given aircraft. Therefore, (i), (ii), and (iii) are restricted to aircraft operation in the vicinity of the operating condition of the aircraft's linearized model. Practical designs for (i), (ii), and (iii) require considering the change in aircraft dynamics with flight condition to cover a wider range of the non-linear flight envelope. The use of the delta operator to develop a unified framework for gain scheduling of (i), (ii), and (iii) is an area that remains open for further research.

We proposed an algorithm for the design of fixed directional residuals suited for multiple FDI of failures in the control actuators. This algorithm yields residual signals of excellent and highly consistent performance that can be used to detect different types of failures. We showed that allowable failures K_ρ are the set of k_{ρ_i}, $i = 1, \ldots, p$ such that Ck_{ρ_i} are independent. Multiple failures in the control actuators were modeled by letting the failure signature K_ρ take the values of the control coefficient matrix H_ρ. Our algorithm for fixed directional residual design can be applied directly to linearized models where the control coefficient matrix is full column rank. Further research should extend our algorithm for multiple FDI to the linearized models of aircraft with rank deficient control distribution matrices. Two areas of study that need to be simultaneously considered for this extension are (1) appropriate reduction of the control space such that the resulting pseudo control distribution matrix is full column rank, and (2) failure description in terms of the chosen pseudo effectors, such that fixed directional residuals well suited for multiple FDI can be obtained in the original control dimensional space.

Appendices

Appendix A

Proof of Theorem 3.1

Gamma Eigenvalue as a Function of Damping and Natural Frequency

$$\begin{aligned}
\gamma &= \frac{e^{\lambda\Delta}-1}{\Delta} = \frac{e^{(-\zeta\omega_n+j\omega_d)\Delta}-1}{\Delta} = \frac{e^{-\zeta\omega_n\Delta}e^{j\omega_d\Delta}-1}{\Delta} \\
&= \frac{e^{-\zeta\omega_n\Delta}(cos(\omega_d\Delta)+jsin(\omega_d\Delta))-1}{\Delta} \\
&= \frac{(e^{-\zeta\omega_n\Delta}cos(\omega_d\Delta)-1)+je^{-\zeta\omega_n\Delta}sin(\omega_d\Delta)}{\Delta} \\
&= \frac{(e^{-\zeta\omega_n\Delta}cos(\omega_n\sqrt{1-\zeta^2}\Delta)-1)+je^{-\zeta\omega_n\Delta}sin(\omega_n\sqrt{1-\zeta^2}\Delta)}{\Delta} \qquad \text{(A.1)}
\end{aligned}$$

Appendix B

Proof of Theorem 3.2

Control Effector Failure Equivalence

Our lateral dynamics design model has four states and five inputs. Let the body axis input matrix be given by

$$B^{body} = \begin{bmatrix} b_{11} & \cdots & b_{1j} & \cdots & b_{15} \\ b_{21} & \cdots & b_{2j} & \cdots & b_{25} \\ b_{31} & \cdots & b_{3j} & \cdots & b_{35} \\ b_{41} & \cdots & b_{4j} & \cdots & b_{45} \end{bmatrix}$$

Then, the corresponding stability axis matrix is

$$B^{stab} = \begin{bmatrix} b_{11} & \cdots & b_{1j} & \cdots & b_{15} \\ b_{21} & \cdots & b_{2j} & \cdots & b_{25} \\ b_{31} cos(\alpha) + b_{41} sin(\alpha) & \cdots & b_{3j} cos(\alpha) + b_{4j} sin(\alpha) & \cdots & b_{35} cos(\alpha) + b_{45} sin(\alpha) \\ b_{31} sin(\alpha) + b_{41} cos(\alpha) & \cdots & b_{3j} sin(\alpha) + b_{4j} cos(\alpha) & \cdots & b_{35} sin(\alpha) + b_{45} cos(\alpha) \end{bmatrix}$$

Let the j-th column of B^{body} denoted by $(b_j)^{body}$ be replaced by w$(b_j)^{body}$. Then,

$$B^{stab} = \begin{bmatrix} b_{11} & \cdots & wb_{1j} & \cdots & b_{15} \\ b_{21} & \cdots & wb_{2j} & \cdots & b_{25} \\ b_{31}cos(\alpha) + b_{41}sin(\alpha) & \cdots & wb_{3j}cos(\alpha) + wb_{4j}sin(\alpha) & \cdots & b_{35}cos(\alpha) + b_{45}sin(\alpha) \\ b_{31}sin(\alpha) + b_{41}cos(\alpha) & \cdots & wb_{3j}sin(\alpha) + wb_{4j}cos(\alpha) & \cdots & b_{35}sin(\alpha) + b_{45}cos(\alpha) \end{bmatrix}$$

or equivalently,

$$B^{stab} = \left[b_1^{stab} \cdots wb_j^{stab} \cdots b_5^{stab}\right] \tag{B.1}$$

This has proven part (1) of the theorem.

Next, map B^{stab} into B_δ^{stab} using Eq.(1.33). Recall that $B_\delta = \Omega B$. Then,

$$B_\delta^{stab} = \Omega B^{stab} = \begin{bmatrix} \Omega_1 \\ \Omega_2 \\ \Omega_3 \\ \Omega_4 \end{bmatrix} \left[b_1^{stab} \cdots wb_j^{stab} \cdots b_5^{stab}\right]$$

where Ω_i is the i-th row of Ω and b_j^{stab} is the j-th column of B^{stab}.

$$\begin{aligned} B_\delta^{stab} &= \begin{bmatrix} \Omega_1 b_1^{stab} \cdots \Omega_1 wb_j^{stab} \cdots \Omega_1 b_5^{stab} \\ \Omega_2 b_1^{stab} \cdots \Omega_2 wb_j^{stab} \cdots \Omega_2 b_5^{stab} \\ \Omega_3 b_1^{stab} \cdots \Omega_3 wb_j^{stab} \cdots \Omega_3 b_5^{stab} \\ \Omega_4 b_1^{stab} \cdots \Omega_4 wb_j^{stab} \cdots \Omega_4 b_5^{stab} \end{bmatrix} \\ &= \left[\Omega b_1^{stab} \cdots \Omega wb_j^{stab} \cdots \Omega b_5^{stab}\right] \\ &= \left[\Omega b_1^{stab} \cdots w(\Omega b_j^{stab}) \cdots \Omega b_5^{stab}\right] \\ &= \left[b_{\delta 1}^{stab} \cdots wb_{\delta j}^{stab} \cdots b_{\delta 5}^{stab}\right] \end{aligned} \tag{B.2}$$

This proves part (2) of the theorem.

Appendix C

Proof of Theorem 3.3

I. Preliminary Result: Delta Operator Small Gain Theorem

We extend the small gain theorem to single input single output delta operator systems. Our proof follows the idea described by Chao and Athans[43] for continuous systems.

Theorem: Consider a single input single output system with forward transfer function $G_1(\gamma)$ and feedback tranfer function $G_2(\gamma)$. Assume that $G_1(\gamma)$ and $G_2(\gamma)$ are stable. Then, the closed loop system is stable if

$$\left|G_1(\frac{e^{j\omega\Delta}-1}{\Delta})\right| \cdot \left|G_2(\frac{e^{j\omega\Delta}-1}{\Delta})\right| < 1 \quad \forall\omega \in [\frac{-\pi}{\Delta}, \frac{\pi}{\Delta}] \tag{C.1}$$

Proof:

$$\left|G_1(\frac{e^{j\omega\Delta}-1}{\Delta})G_2(\frac{e^{j\omega\Delta}-1}{\Delta})\right| \leq \left|G_1(\frac{e^{j\omega\Delta}-1}{\Delta})\right| \cdot \left|G_2(\frac{e^{j\omega\Delta}-1}{\Delta})\right| < 1 \quad \forall\omega \in [\frac{-\pi}{\Delta}, \frac{\pi}{\Delta}] \tag{C.2}$$

$$\Rightarrow \left|G_1(\frac{e^{j\omega\Delta}-1}{\Delta})G_2(\frac{e^{j\omega\Delta}-1}{\Delta})\right| < 1 \quad \forall\omega \in [\frac{-\pi}{\Delta}, \frac{\pi}{\Delta}] \tag{C.3}$$

Eq.(C.3) implies that the Nyquist plot of $G_1(\gamma)G_2(\gamma)$ lies strictly inside the unit circle centered at the origin. This is sufficient for stability because $G_1(\gamma)$ and $G_2(\gamma)$ are stable.

II. Main Result: Delta Operator Disk Margin Theorem

Consider an uncertain single input single output feedback system with loop transfer function $L(\gamma)$ and uncertainty Δ. Refs.[41] and [42] propose a block diagram where the transfer function seen by Δ is $S(\gamma) - T(\gamma)$. Let the gain K stabilize the nominal feedback system. Then, $S(\gamma) - T(\gamma) = \frac{1-L(\gamma)}{1+L(\gamma)}$ is stable. Let $\Delta = re^{j\theta}$ where $\theta \in [0, 2\pi]$.

The uncertain closed loop system is stable by the small gain theorem if

$$\max_{\omega \in [\frac{-\pi}{\Delta}, \frac{\pi}{\Delta}]} \left| S(\frac{e^{j\omega\Delta} - 1}{\Delta}) - T(\frac{e^{j\omega\Delta} - 1}{\Delta}) \right| \cdot |\Delta| < 1 \tag{C.4}$$

$$\Leftrightarrow \max_{\omega \in [\frac{-\pi}{\Delta}, \frac{\pi}{\Delta}]} \left| S(\frac{e^{j\omega\Delta} - 1}{\Delta}) - T(\frac{e^{j\omega\Delta} - 1}{\Delta}) \right| \cdot r < 1 \tag{C.5}$$

$$\Leftrightarrow r < \frac{1}{\max_{\omega \in [\frac{-\pi}{\Delta}, \frac{\pi}{\Delta}]} \left| S(\frac{e^{j\omega\Delta}-1}{\Delta}) - T(\frac{e^{j\omega\Delta}-1}{\Delta}) \right|} \equiv r_{min} \tag{C.6}$$

Now referring to the block diagram in Refs.[41] and [42] where the transfer function seen by Δ is $S(\gamma) - T(\gamma)$. It is easily shown that the transfer function seen by $L(\gamma)$ is $\frac{1-\Delta}{1+\Delta}$. Then, the loop gain of the uncertain system is the nominal loop gain multiplied by $\frac{1-\Delta}{1+\Delta}$ where $\Delta = re^{j\theta}$. This implies that the uncertainty seen by $L(\gamma)$ is $\frac{1-re^{j\theta}}{1+re^{-j\theta}}$. The gain margin GM is defined for $\frac{1-re^{j\theta}}{1+re^{-j\theta}}$ real. This quantity is real when $e^{j\theta}$ is real which occurs at $\theta = 0$ or $\theta = \pi$. When $\theta = 0$, $\frac{1-re^{j\theta}}{1+re^{-j\theta}} = \frac{1-r}{1+r}$ and when $\theta = \pi$, $\frac{1-re^{j\theta}}{1+re^{-j\theta}} = \frac{1+r}{1-r}$. Therefore, the disk gain margins are given by

$$GM = \left[\frac{1 - r_{min}}{1 + r_{min}}, \frac{1 + r_{min}}{1 - r_{min}} \right] \tag{C.7}$$

The phase margin is defined for $\left|\frac{1-re^{j\theta}}{1+re^{j\theta}}\right| = 1$. It follows that $\left|\frac{1-re^{j\theta}}{1+re^{j\theta}}\right| = 1 \Leftrightarrow \left|\frac{1-r(cos\theta+jsin\theta)}{1+r(cos\theta+jsin\theta)}\right| = 1 \Leftrightarrow \left|\frac{(1-rcos\theta)-jrsin\theta}{(1+rcos\theta)+jsin\theta}\right| = 1 \Leftrightarrow cos\theta = 0 \Leftrightarrow \theta = \pm\frac{\pi}{2}$. Then, at $\theta = \frac{\pi}{2}, arg\left(\frac{1-re^{j\theta}}{1+re^{j\theta}}\right) = arg\left(\frac{1-jr}{1+jr}\right) = -2tan^{-1}r$. Similarly, when $\theta = -\frac{\pi}{2}, arg\left(\frac{1-re^{j\theta}}{1+re^{j\theta}}\right) = arg\left(\frac{1+jr}{1-jr}\right) = 2tan^{-1}r$. Therefore, the disk phase margins are given by

$$PM = \left[-2tan^{-1}r_{min}, 2tan^{-1}r_{min}\right] \tag{C.8}$$

Appendix D

Proof of Theorem 4.1

$$G_{rf}(\gamma) = W_\rho C \left(\sum_{i=1}^{n} \frac{v_i {p_i}^T}{\gamma - \gamma_i} \right) K_\rho \tag{D.1}$$

use Eq.(4.27) for $i = p+1, \ldots, n$

$$\begin{aligned} G_{rf}(\gamma) &= W_\rho C \left(\sum_{i=1}^{p} \frac{v_i {p_i}^T}{\gamma - \gamma_i} \right) K_\rho && \text{(D.2)} \\ &= W_\rho C \left[\sum_{i=1}^{p} \frac{v_i {p_i}^T}{\gamma - \gamma_i} k_{\rho 1}, \quad \ldots, \quad \sum_{i=1}^{p} \frac{v_i {p_i}^T}{\gamma - \gamma_i} k_{\rho p} \right] && \text{(D.3)} \end{aligned}$$

use Eq.(4.27) for $i = 1, \ldots, p$

$$G_{rf}(\gamma) = W_\rho \left[C v_1 \tfrac{<p_1, k_{\rho 1}>}{\gamma - \gamma_1}, \quad \ldots, \quad C v_p \tfrac{<p_p, k_{\rho p}>}{\gamma - \gamma_p} \right] \tag{D.4}$$

Appendix E

Proof of Corollary 4.1

It follows from theorem 4.1 and Eq.(4.27) that

$$G_{rf}(\gamma) = W_\rho C V_1 {P_1}^T K_\rho \; diag\left(\frac{1}{\gamma - \gamma_j}\right), \quad j = 1, \; \ldots, \; p \tag{E.1}$$

use $V_1 {P_1}^T + V_2 {P_2}^T = I \Leftrightarrow V_1 {P_1}^T = I - V_2 {P_2}^T$

$$G_{rf}(\gamma) = W_\rho C (I - V_2 {P_2}^T) K_\rho \; diag\left(\frac{1}{\gamma - \gamma_j}\right) \tag{E.2}$$

Use Eq.(4.27) for $i = p+1, \ldots, n \Rightarrow P_2^T K_\rho = 0$ for $i = p+1, \ldots, n$

$$\begin{aligned} G_{rf}(\gamma) &= W_\rho C K_\rho \; diag\left(\frac{1}{\gamma - \gamma_j}\right), \quad j = 1, \ldots, p & \text{(E.3)} \\ &= W_\rho \left[\tfrac{C k_{\rho_1}}{\gamma - \gamma_1}, \quad \ldots, \quad \tfrac{C k_{\rho_p}}{\gamma - \gamma_p} \right] & \text{(E.4)} \end{aligned}$$

Appendix F

Proof of Corollary 4.2

$$\begin{aligned} VP^T &= I && \text{(F.1)} \\ V_1{P_1}^T + V_2{P_2}^T &= I && \text{(F.2)} \\ \left(V_1{P_1}^T + V_2{P_2}^T\right) K_\rho &= K_\rho && \text{(F.3)} \\ V_1{P_1}^T K_\rho + V_2{P_2}^T K_\rho &= K_\rho && \text{(F.4)} \end{aligned}$$

apply Eq.(4.32) for $i = p+1, \ldots, n \Rightarrow V_2{P_2}^T K_\rho = 0$

$$V_1{P_1}^T K_\rho = K_\rho \tag{F.5}$$

$$CV_1{P_1}^T K_\rho = CK_\rho \tag{F.6}$$

use Eq.(4.32) for $i = 1, \ldots, p$

$$\begin{aligned} C \begin{bmatrix} v_1, & \ldots, & v_p \end{bmatrix} diag \begin{bmatrix} < p_1, k_{\rho 1} >, & \ldots, & < p_p, k_{\rho p} > \end{bmatrix} &= CK_\rho && \text{(F.7)} \\ C \begin{bmatrix} v_1, & \ldots, & v_p \end{bmatrix} diag \begin{bmatrix} d_{\rho 1}, & \ldots, & d_{\rho p} \end{bmatrix} &= CK_\rho && \text{(F.8)} \end{aligned}$$

$$\begin{bmatrix} Cd_{\rho 1}v_1, & \ldots, & Cd_{\rho p}v_p \end{bmatrix} = \begin{bmatrix} Ck_{\rho 1}, & \ldots, & Ck_{\rho p} \end{bmatrix} \tag{F.9}$$

Eq.(F.9) shows that the Cv_i's are in the same direction as the columns of CK_ρ. Therefore, CK_ρ and CV_1 have the same column rank.

Appendix G

Proof of Lemma 4.1

From Corollary 4.1

$$G_{rf}(\gamma) = W_\rho C K_\rho \; diag\left(\frac{1}{\gamma - \gamma_j}\right), \quad j = 1, \ldots, p \tag{G.1}$$

Substitute W_ρ from Eq.(4.34) into Eq.(G.1) to obtain

$$G_{rf}(\gamma) = diag\left(-\gamma_j\right)\left(C K_\rho\right)^{\ddagger} C K_\rho \; diag\left(\frac{1}{\gamma - \gamma_j}\right), \quad j = 1, \ldots, p \tag{G.2}$$

simplify

$$G_{rf}(\gamma) = diag\left(\frac{-\gamma_j}{\gamma - \gamma_j}\right) \tag{G.3}$$

Appendix H

Proof of Theorem 4.2

First we need the following preliminary theorem.

Theorem H1:

If Λ is a stability matrix and $G = \sup\limits_{0 \leq t < \infty} \|g(t)\|$ then,

$$\mathop{\mathbf{S}}\limits_0^t \|\mathrm{E}_{L\rho}\left(\Lambda,\ t-\tau-\Delta\right)\| \cdot \|g(t)\|\, d\tau \leq \frac{G}{f(\lambda)}$$

where

$$f(\lambda) = \begin{cases} -\max\limits_i \mathrm{Re}\lambda_i; & \text{continuous time} \\ \\ \frac{1}{\Delta}\left[1 - \max\limits_i |1 + \Delta\gamma_i|\right]; & \text{discrete time} \end{cases}$$

Proof:

$$\begin{aligned} \mathop{\mathbf{S}}\limits_0^t \|\mathrm{E}_{L\rho}(\Lambda,\ t-\tau-\Delta)\| \cdot \|g(t)\|\ d\tau &= \mathop{\mathbf{S}}\limits_0^t \|\mathrm{E}_{L\rho}(\Lambda,\ \tau)\| \cdot \|g(t-\tau-\Delta)\|\ d\tau \\ &\leq \left(\mathop{\mathbf{S}}\limits_0^t \|\mathrm{E}_{L\rho}(\Lambda,\ \tau)\|\ d\tau\right) \cdot G \end{aligned}$$

where

$$\mathrm{E}_{L\rho}(\Lambda,\ t) = \begin{cases} e^{\Lambda t} & ; \quad \text{continuous time} \\ \\ (I + \Lambda\Delta)^{\frac{t}{\Delta}} & ; \quad \text{discrete time} \end{cases}$$

and

$$\|\mathrm{E}_{L\rho}(\Lambda,\ t)\| \leq \begin{cases} e^{(\max\limits_i \ \mathrm{Re}\lambda_i)t} & ; \quad \text{continuous time} \\ \\ \max\limits_i |1 + \Delta\gamma_i\ |^{\frac{t}{\Delta}} & ; \quad \text{discrete time} \end{cases}$$

In continuous time:

$$\begin{aligned} \left(\overset{t}{\underset{0}{\mathbf{S}}} \|\mathrm{E}_{L\rho}(\Lambda,\ \tau)\|\ d\tau\right) \cdot G \quad &\leq \quad \left(\int\limits_0^t e^{(\max\limits_i \ \mathrm{Re}\lambda_i)\cdot\tau}\ d\tau\right) \cdot G \\ &\leq \quad \left(\frac{e^{\max\limits_i \ \mathrm{Re}(\lambda_i)\cdot t} - 1}{\max\limits_i \ \mathrm{Re}\lambda_i}\right) \cdot G \\ &\leq \quad \left(\frac{-1}{\max\limits_i \ \mathrm{Re}\lambda_i}\right) \cdot G \\ &= \quad \frac{G}{f(\lambda)} \end{aligned}$$

In discrete time:

$$\left(\overset{t}{\underset{0}{\mathbf{S}}} \|\mathrm{E}_{L\rho}(\Lambda,\ \tau)\|\ d\tau\right) \cdot G \ \leq \left(\Delta \sum_0^{\frac{t}{\Delta}-1} \left(\max_i |1 + \Delta\gamma_i\ |\right)^{\frac{t}{\Delta}}\right) \cdot G$$

use

$$\sum_0^\infty r^k = \frac{1}{1-r}\ ; \quad r < 1$$

and

$$|1 + \Delta\gamma_i\ | < 1 \quad \forall i$$

then,

$$\left(\overset{t}{\underset{0}{\mathbf{S}}}\|\mathrm{E}_{L\rho}(\Lambda,\ \tau)\|\ \ d\tau\right)\cdot G\ \le \left(\frac{\Delta}{1-\max\limits_{i}|1+\Delta\gamma_i\ |}\right)\cdot G\ = \frac{G}{f(\lambda)}$$

Now we return to the proof of theorem 4.2.

Substitute Eqs.(4.40) and (4.41) into

$$\rho e(t) = \rho x(t) - \rho\hat{x}(t) \tag{H.1}$$

$$\begin{aligned} \rho e(t) &= (G_\rho + dG_\rho)x(t) + (H_\rho + dH_\rho)[u(t) + \mathrm{v}(t)] - [(G_\rho - L_\rho C)\hat{x}(t) && \text{(H.2)} \\ &\quad +H_\rho u(t) + L_\rho Cx(t) + L_\rho w(t)] && \text{(H.3)} \\ &= (G_\rho - L_\rho C)[x(t) - \hat{x}(t)] + H_\rho \mathrm{v}(t) + dH_\rho[u(t) + \mathrm{v}(t)] - L_\rho w(t) && \text{(H.4)} \\ &\quad +dG_\rho x(t) && \text{(H.5)} \end{aligned}$$

Let

$$de(t) = dG_\rho x(t) + dH_\rho[u(t) + \mathrm{v}(t)] - L_\rho w(t) + H_\rho \mathrm{v}(t) \tag{H.6}$$

Then,

$$\begin{aligned} \rho e(t) &= (G_\rho - L_\rho C)e(t) + de(t) && \text{(H.7)} \\ &= G_{L\rho}e(t) + de(t) && \text{(H.8)} \end{aligned}$$

Recall that

$$r(t) = W_\rho\,[y(t) - \hat{y}(t)] \tag{H.9}$$

so

$$r(t) = W_\rho\,[Ce(t) + w(t)] \tag{H.10}$$

The solution to Eq(H.10) is given by Middleton and Goodwin [17] as follows

$$r(t) = W_\rho C \left[V\mathbf{E}_{L\rho}\left(\Lambda, t\right) P^T e(0) + \overset{t}{\underset{0}{\mathbf{S}}} V\mathbf{E}_{L\rho}\left(\Lambda, t-\tau-\Delta\right) P^T de(\tau) d\tau \right] + W_\rho w(t) \tag{H.11}$$

$$\begin{aligned} r(t) = W_\rho C[V\mathbf{E}_{L\rho}(\Lambda, t)P^T e(0) + \overset{t}{\underset{0}{\mathbf{S}}} V\mathbf{E}_{L\rho}(\Lambda, t-\tau-\Delta)P^T\{dG_\rho(x,u)x(\tau) \\ + dH_\rho(x,u)\left[u(\tau)+\mathrm{v}(\tau)\right] - L_\rho w(\tau) + H_\rho \mathrm{v}(\tau)\}d\tau] + W_\rho w(t) \end{aligned} \tag{H.12}$$

$$\begin{aligned} \|r(t)\| \leq \|W_\rho CV\| \left[\|\mathbf{E}_{L\rho}(\Lambda, t)\| \left\|P^T e(0)\right\| + \overset{t}{\underset{0}{\mathbf{S}}} \|\mathbf{E}_{L\rho}(\Lambda, t-\tau-\Delta)\| \{\left\|P^T\right\| \|d\tilde{e}(\tau)\| \right. \\ \left. + \left\|P^T L_\rho\right\| \|w(\tau)\|\}d\tau\right] + \|W_\rho\| \|w(t)\| \end{aligned} \tag{H.13}$$

use $\|\mathbf{E}_{L\rho}(\Lambda, t)\| \leq 1$, $\sup\limits_{0\leq t<\infty} \|d\tilde{e}(t)\| < B_1$, $\sup\limits_{0\leq t<\infty} \|w(t)\| < B_2$, and theorem H1 to obtain

$$\|r(t)\| \leq \|W_\rho CV\| \left[\left\|P^T e(0)\right\| + \frac{\|P\| \ \cdot B_1 + \left\|P^T L_\rho\right\| \cdot B_2}{f(\lambda)}\right] + \|W_\rho\| \|w(t)\| \tag{H.14}$$

List of Publications

Nieto-Wire, C. and Sobel, K., *"Fault detection using eigenvalue/eigenvector optimization for delta operator systems"*. International Journal of Aerospace Engineering, in preparation.

Nieto-Wire, C. and Sobel, K., *"Flight Control Design for a Tailless Aircraft Using Eigenstructure Assignment"*. International Journal of Aerospace Engineering, vol. 2011, Article ID 549131, 13 pages, 2011. doi:10.1155/2011/549131.

Nieto-Wire, C. and Sobel, K., *"Observer-based residual generator design for multiple fault detection and isolation"*. in Junior Scientist Conference, Vienna, Austria, April 2010, pp. 91-92.

Nieto-Wire, C., and Sobel, K.M., *"Reconfigurable Delta Operator Eigenstructure Assignment for a Tailless Aircraft"*. AIAA Guidance, Navigation, and Control Conference, Chicago, IL, August 10-11, 2009, AIAA Paper 2009-6306.

Nieto-Wire, C., and Sobel, K.M., *"Eigenstructure Assigment for a Tailless Aircraft"*. AIAA Guidance, Navigation, and Control Conference, Hilton Head, SC, August 20-23, 2007, AIAA Paper 2007-6417.

Bibliography

[1] Dorsett, K.M., and Mehl, D.R., "Innovative control effectors (ICE)," Final Report for September 1994 - January 1996, Wright Laboratory, Air Force Material Command, Tech. Rep. WL-TR-96-3043, January 1996.

[2] Dorsett, K.M., Fears, S.P., and Houlden, H.P., "Innovative control effectors (ICE) phase III," Final Report for March 1996 - July 1997, Wright Laboratory, Air Force Material Command, Tech. Rep. WL-TR-3059, August 1997.

[3] *Aircraft Control Toolbox User's Guide*, Princeton Satellite Systems, Princeton, NJ, March 2003.

[4] Blake, W., "AFRL/VACA," Private Communication, September 2004.

[5] Ngo, A.N., Reigelsperger, W.C., and Banda, S.S., "Multivariable control law design for a tailless aircraft," in *Proceedings of the AIAA Guidance, Navigation, and Control Conference*, San Diego, CA, July 29-31 1996, AIAA Paper 96-3866.

[6] Sparks, A.G., "A gain scheduled H_∞ control law for a tailless aircraft," in *Proceedings of the 1998 IEEE International Conference on Control Applications*, Trieste, Italy, September 1-4 1998, pp. 674–678.

[7] Schumacher, C., and Johnson, C.D., "PI control of a tailless fighter aircraft with dynamic inversion and neural networks," in *Proceedings of the American Control Conference*, San Diego, CA, June 1999, pp. 4173–4177.

[8] Shtessel, Y., Buffington, J., and Banda, S., "Tailless aircraft flight control using multiple time scale reconfigurable sliding modes," *IEEE Transactions on Control Systems Technology*, vol. 10, no. 2, pp. 288–296, March 2002.

[9] Hess, R.A., Vetter, T.K., and Wells, S.R., "Design and evaluation of a damage tolerant flight control system," in *Proceedings of the AIAA Guidance, Navigation, and Control Conference*, Providence, RI, August 16-19 2004, AIAA Paper 2004-4872.

[10] Jones, C.D.C., Lowenberg, M.H., and Richardson, T.S., "Dynamic state feedback control of the ICE 101-TV," in *Proceedings of the AIAA Guidance, Navigation, and Control Conference*, Providence, RI, August 16-19 2004, AIAA Paper 2004-4754.

[11] Andry, A.N., Shapiro, E.Y., and Chung, J.C. , "Eigenstructure assignment for linear systems," *IEEE Transactions on Aerospace and Electronic Systems*, vol. 19, no. 5, pp. 711–729, September 1983.

[12] Davidson, J.B., and Andrisani D. , "Lateral-directional eigenvector flying qualities guidelines for high performance aircraft," NASA Technical Memorandum 110306, NASA Langley Research Center, Tech. Rep., December 1996.

[13] Jiang, J., "Design of reconfigurable control systems using eigenstructure assignments," *International Journal of Control*, vol. 59, no. 2, pp. 395–410, February 1994.

[14] Konstantopoulos, I., "Optimal controller design and reconfigurable control under stability robustness," Ph.D. dissertation, University of Notre Dame, January 1996.

[15] Ashari, A.E., Sedigh, A.K., and Yazdanpanah, M.J., "Reconfigurable control system design using eigenstructure assignment: Static, dynamic, and robust

approaches," *International Journal of Control*, vol. 78, no. 13, pp. 1005–1016, September 2005.

[16] Piou, J.E., and Sobel, K., "Robust Sampled Data Eigenstructure Assignment using the Delta Operator," *Journal of Guidance, Control, and Dynamics*, vol. 16, no. 4, pp. 702–711, July-August 1993.

[17] Middleton, R.H. and Goodwin, G.C., *Digital Control and Estimation: A Unified Approach*. Englewood Cliffs, NJ: Prentice-Hall, 1990.

[18] Beard, R.V., "Failure accommodation in linear systems through self-reconfiguration," Ph.D. dissertation, Massachusetts Inst. of Technology, Cambridge,MA, February 1971.

[19] Jones, H.L., "Failure detection in linear systems," Ph.D. dissertation, Massachusetts Inst. of Technology, Cambridge,MA, August 1973.

[20] White, J.E. and Speyer J.L., "Detection filter design: Spectral theory and algorithms," *IEEE Transactions on Automatic Control*, vol. AC-32, no. 7, pp. 593–603, July 1987.

[21] Moore, B.C., "On the flexibility offered by state feedback in multivariable systems beyond closed loop eigenvalue assignment," *IEEE Transactions on Automatic Control*, vol. 21, no. 6, pp. 689–692, October 1976.

[22] Chen, B., and Nagarajaiah, S., "Linear-matrix-inequality-based robust fault detection and isolation using the eigenstructure assignment method," *Journal of Guidance, Control, and Dynamics*, vol. 30, no. 6, pp. 1831–1835, November-December 2007.

[23] Li, Z., and Jaimoukah, I.M., "Observer-based fault detection and isolation filter design for linear-time invariant systems," *International Journal of Control*, vol. 82, no. 1, pp. 171–182, January 2009.

[24] Douglas, R.K., and Speyer, J.L., "An h-infinity bounded fault detection filter," in *Proceedings of the American Control Conference*, Seattle, WA, June 1995, pp. 86–90.

[25] Liu, B., and Si, J. , "Fault isolation filter design for linear time-invariant systems," *IEEE Transactions on Automatic Control*, vol. 42, no. 5, pp. 704–707, May 1997.

[26] Shen, L.C., Chang, S.K. and Hsu, P.L., "Robust Fault Detection and Isolation with Unstructured Uncertainty Using Eigenstructure Assignment," *Journal of Guidance, Control and Dynamics*, vol. 21, no. 1, pp. 50–57, January-February 1998.

[27] Narendra, K., and Tripathi, S.S., "Identification and optimization of aircraft dynamics," *Journal of Aircraft*, vol. 10, no. 4, pp. 193–199, January-February 1973.

[28] Srinathkumar, S., "Eigenvalue/eigenvector assignment using output feedback," *IEEE Transactions on Automatic Control*, vol. 23, no. 1, pp. 79–81, February 1978.

[29] Kautsky, J., Nichols, N.K., and Van Dooren,P. , "Robust pole assignment in linear state feedback," *International Journal of Control*, vol. 41, no. 5, pp. 1129–1155, May 1985.

[30] Sobel, K.M., and Lallman, J.F., "Eigenstructure assignment for the control of a highly augmented aircraft," *Journal of Guidance, Control and Dynamics*, vol. 12, no. 3, pp. 318–324, May-June 1989.

[31] Klema, V. C., and Laub, A. J, “The singular value decomposition: Its computation and some applications,” *IEEE Transactions on Automatic Control*, vol. 25, no. 2, pp. 164–176, April 1980.

[32] Sobel, K. M., and Banda, S.S., “Design of a modalized observer with eigenvalue sensitivity reduction,” *Journal of Guidance, Control and Dynamics*, vol. 12, no. 5, pp. 762–764, October 1989.

[33] Malcom, L.G., and Tobie, H.N. , “New short period handling quality criterion for fighter aircraft,” The Boeing Company, Tech. Rep., 1965.

[34] “Military specification flying qualities of piloted airplanes,” MIL-F-8785C, November 5 1980.

[35] “Military specification flight control systems - design, installation and test of piloted aircraft,” MIL-F-9490D, June 6 1975.

[36] Stevens, B.L., and Lewis, F.L. , *Aircraft Control and Simulation.* New York, NY: Wiley, 1992.

[37] Yechout, T.R., Morris, S.L., Bossert, D.E., and Hallgren, W.F., *Introduction to Aircraft Flight Mechanics: Performance, Static Stability, Dynamic Stability, and Classical Feedback Control*, ser. AIAA Education Series. Reston, VA: American Institute of Aeronautics and Astronautics, 2003.

[38] Pratt, R., *Flight Control Systems: Practical Issues in Design and Implementation.* The Institution of Electrical Engineers and The American Institute of Aeronautics and Astronautics, 2000.

[39] Balas, G., Chiang, R., Packard, A., and Safonov, M., *Robust Control Toolbox for use with* MATLAB®. Natick, MA: The Mathworks, Inc., 2006.

[40] Barrett, M.F., "Conservatism with robustness tests for linear feedback control systems," Ph.D. dissertation, University of Minnesota, June 1980.

[41] Blight, J.D., Dailey, R.L., and Gangsaas, D., "Practical control law design for aircraft using multivariable techniques," *International Journal of Control*, vol. 59, no. 1, pp. 93–137, January 1994.

[42] Bates, D., and Postlethwaite, I., *Robust Multivariable Control of Aerospace Systems.* Amsterdam, NL: Delft University Press, 2002.

[43] Chao, A., and Athans, M., "Stability robustness to unstructured uncertainty for linear time invariant systems," in *The Control Handbook.* IEEE Press, 1996, pp. 519–535.

[44] Nieto-Wire, C., and Sobel, K., "Eigenstructure assignment for a tailless aircraft," in *Proceedings of the AIAA Guidance, Navigation, and Control Conference*, Hilton Head, SC, August 20-23 2007, AIAA Paper 2007-6417.

[45] "Optimization toolbox for use with MATLAB®," The Mathworks, Inc.

[46] Massoumnia, M.A., "A geometric approach to the synthesis of failure detection filters," *IEEE Transactions on Automatic Control*, vol. 31, no. 9, pp. 839–846, September 1986.

[47] Nieto-Wire, C., and Sobel, K. M., "Fault detection using eigenvalue/eigenvector optimization for delta operator systems," *International Journal of Aerospace Engineering*, in preparation.

[48] Patton, R.J., and Chen, J., "Robust Fault Detection Using Eigenstructure Assignment: A Tutorial Consideration and Some New Results," in *Proceedings of 30th Conference on Decision and Control*, Brighton, UK, December 1991, pp. 2242–2247.